ABSTRACT

Title of Document: FORMATION AND CHARACTERIZATION
OF TRANSVERSELY MODULATED
NANOSTRUCTURES IN METALLIC THIN
FILMS USING EPITAXIAL CONTROL

Brad Michael Boyerinas, Ph.D, 2013

Directed By: Hugh A. Bruck, Professor, Department of
Mechanical Engineering

This thesis describes a fundamental investigation into the formation, characterization, and modeling of epitaxially-controlled self-assembly at the nanoscale. The presence of coherent nanophases and the clamping effect from an epitaxial substrate enables the formation of transversely modulated nanostructures (TMNS) resulting in improved functionality, which was previously observed through increased piezoelectric response in $BiFeO_3$. The ability to fabricate high quality epitaxial films presents opportunity to investigate coherent phase decomposition in other material systems with multifunctional response.

The research herein aims to extend the concept of nanoscale self assembly in metallic systems, including Ag-Si and Pd-PdH. First, the effect of annealing a Ag-Si couple was examined, and ordered, nanoscale Ag crystallites were observed along the interface with the epitaxial Si wafer. It is demonstrated that Ag foil can be used in place of doped Ag paste (commonly used in solar cell metallization) to achieve TMNS at the interface. It was proved that annealing the Ag-Si couple in air is necessary for the self-assembly reaction to take place, as doing so prevents bulk diffusion and eutectic melting. Electron backscatter diffraction was used to verify the epitaxial relation between the Ag nanostructures and Si crystal.

A method to fabricate ordered, nanoscale PdH precipitates in epitaxial Pd thin films via high temperate gas phase hydrogenation was established. Epitaxial Pd films were deposited via e-beam deposition and a V buffer layer was necessary to induce epitaxy. This novel self-assembled nanostructure may enable hysteresis-less absorption and desorption, thus improving functionality with regard to hydrogen sensing and storage. The epitaxial Pd film was characterized before and after hydrogenation with x-ray diffraction and atomic force microscopy to determine composition and nanostructure of the film.

A thermodynamic model was developed to demonstrate the possibility to control or eliminate thermodynamic hysteresis via balance of elastic interaction between the coherent interfaces of metal and metal-hydride phases and the film-substrate interface. This model can be extended to other metal-hydride systems which demonstrate coherent phase decomposition.

Formation and Characterization of Transversely Modulated Nanostructures in Metallic Thin Films using Epitaxial Control

By

Brad Michael Boyerinas

Dissertation submitted to the Faculty of the Graduate School of the
University of Maryland, College Park, in partial fulfillment
of the requirements for the degree of
Doctor of Philosophy
2013

Advisory Committee:

Professor Hugh A. Bruck, Chair/Advisor
Associate Professor Teng Li
Associate Professor Santiago Solares
Associate Professor F. Patrick McCluskey
Professor Alexander L. Roytburd (Dean's Representative)

Acknowledgements

I would like to express gratitude toward my research advisor, Dr. Hugh Bruck, for his guidance throughout the entire course of this dissertation. It was a great experience to be granted the freedom to pursue fundamental research and receive valuable feedback and direction along the way. I would like to thank Dr. Alexander Roytburd for his advisement in the area of nanostructured materials and also for numerous insightful discussions in the area of materials science and science in general. I would like to acknowledge Dr. Santiago Solares, Dr. Teng Li, and Dr. Patrick McCluskey for serving on my PhD committee. Financial support from NSF-DMR #0907122 is also gratefully acknowledged.

I am grateful for the opportunity to perform much of the experimental work presented in this dissertation at the National Institute of Standards and Technology (Gaithersburg, MD). Dr. Albert Davydov of NIST provided assistance with EBSD analysis and Dr. Leo Bendersky of NIST provided valuable insight into metal-hydrides and I am appreciative of their support.

I would like to acknowledge Sandip Haldar and other colleagues in the Multiscale Measurements Lab for their camaraderie and discussions during the course of this dissertation.

Last, and certainly not least, I want to thank my family for their support over the years which made this effort possible.

Table of Contents

List of Tables

List of Figures

1 Introduction

1.1 Background

The advent of nanoscale materials fabrication and analysis, where one or more material dimensions is in the sub-100nm range, has enabled researchers to realize and tailor novel properties that are not present on the macro scale. For instance, bulk alloy systems that adhere to traditional phase diagrams may present novel phase compositions when deposited as a thin film on a rigid substrate. The clamping condition of the substrate on the film due to epitaxy may significantly alter the thermodynamic state of the film and stabilize coherent phase decomposition that is not seen on the bulk scale under similar conditions. This phenomenon was first theoretically considered in 1976 [1] as the trend towards relaxation of elastic misfit that is responsible for creating stable periodic domain structures. Such structures been observed in ferroic films, namely $BiFeO_3$, where modulated rhombohedral and tetragonal phases are stable due to the clamping effect on the film.

Self organization on the nano scale is a natural phenomenon that allows bottom-up design and fabrication of nanostructures that cannot be made with conventional techniques such as etching and machining, and can also enable novel functional properties when such structures are aligned in a particular manner. This process can involve the separation or patterning of unlike materials, such as Ag and Si, or the ordered layout of like materials that decompose into periodic phases, as observed in ferroic films ($BiFeO_3$). The minimization of elastic energy between thin film polydomain phases and the substrate stabilizes the two-phase state, thus acting as a formation mechanism of self assembly for such systems.

While it is well known that the phase distribution of a metallic material system on the bulk scale will govern its physical properties such as hardness and stiffness, phase coexistence in nanoscale film has been observed experimentally as a highly unstable phenomenon that can be altered significantly via external stimuli, such as mechanical or electrical loading, thus drastically affecting physical properties [2]. Mechanical softening can occur under such loading, and, in fact, peculiar material properties such as negative Young's modulus have been predicted due to domain instability during deformation [1]. More recently, domains consisting of alternating phases in $BiFeO_3$ (Figure 1.1) have been observed shifting (percent fraction of domain increases or decreases) under load, thus altering the piezoelectric effect. This unique ordered arrangement of domains, and its ability to rearrange due to elastic instability, provides improved functionality when compared to a film of similar composition with only a single domain state.

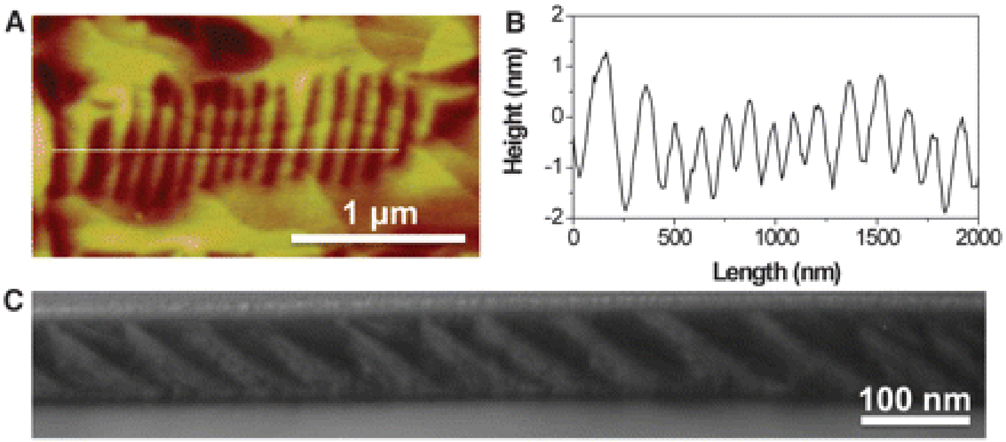

Figure 1.1 AFM topographical scan (A), height profile (B), and cross sectional TEM micrograph (C) of alternating tetragonal and rhombohedral polydomains in $BiFeO_3$ film [2].

Film deposition techniques such as sputtering and e-beam deposition are capable of producing high quality epitaxial films of various compositions. In the case of heteroepitaxy, dislocations may form to relieve misfit strain. These dislocations generally form ordered, periodic patterns due to long range repulsion of the dislocations and high mobility on the film surface. This patterning can be used as a template for deposition of zero-dimensional structures (quantum dots), shown in Figure 1.2, as island nucleation is energetically favorable at a sufficient distance from dislocations.

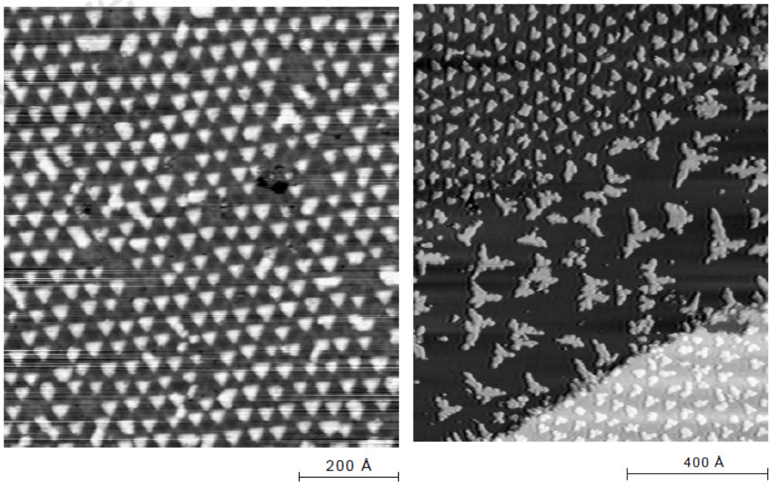

Figure 1.2 STM image of nucleated Fe islands grown across dislocation networks on Cu film (left) and ordered vs randomly oriented islands grown on dissimilar substrate [3].

Coherent phase decomposition is dependent on relative lattice parameters of parent and product phases and relies on the balance between strain energy and surface energy [4]. Generally, the properties of multiphase systems depend not only on the constituent elements, but also their micro/nano structure and the nature of the boundary between phases. The ordered, chessboard like structure (Figure 1.3) is self-organized such that multiple variants of the precipitate align normal to planes of minimal stiffness (elastically soft directions).

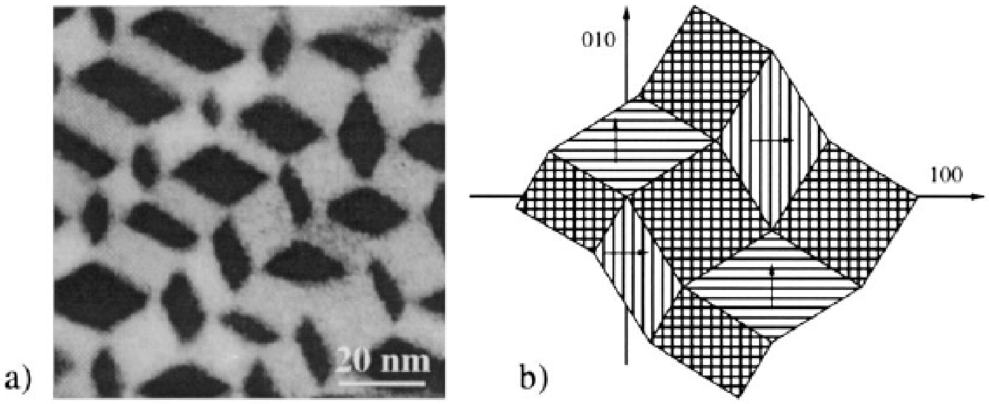

Figure 1.3 Dark field TEM image (a) and schematic representation (b) of Co-Pt coherent chessboard nanostructure composed of cubic and tetragonal phases [4].

Tailoring ordered nanostructures along functional interfaces is desirable when considering devices where mechanical reliability or electrical conductivity along the interface is crucial. Si-based solar cells fall within this category and are under vast scrutiny in the scientific community. While both Si and electrode material (commonly Ag) are not usually processed in nanoscale film thicknesses, the layered heterostructure can be thermally processed so that the constituent materials interact, thus creating an effective "film" layer that is sandwiched between its bulk counterparts. Processing parameters have been established for interfacial nanostructure formation in the Ag-Si system [5]. These structures form primarily due to the fact that one bulk constituent (Si) is a single crystal and serves as an epitaxial template for ordered nanostructure growth. Changing duration of thermal treatment will alter nanostructure size and distribution while changing the single crystal orientation will alter nanostructure morphology.

1.2 Motivation for Research

The utilization of nanoscale material characterization techniques enables one to design materials for optimal performance with regard to novel nanostructure. Design constraints, such as epitaxial strain (lattice mismatch), processing conditions, and film thickness all play a role in coherent phase decomposition in thin films [6]. Developing principles of formation of transversely modulated nanostructures in metallic thin films and interfaces will enable engineers to develop and optimize functional properties in these systems.

Nanostructured metal-semiconductor interfaces have been studied in terms of conductivity for solar cell applications [7]-[10]. Embedded Ag crystallites have been observed embedded in Si after metallization of the Si surface with glass doped Ag paste. Due to the insulating nature of the glass, the Ag crystallites serve as the only conducting pathway of the solar cell. Optimizing Ag crystallite size and periodicity, as well as considering alternative methods of Si surface metallization, may enable more efficient solar cell operation.

Hydrogen storage in metallic thin films has been the subject of intense study due to the current need for sustainable energy and also for use as hydrogen sensors [11]-[24]. As specific metal films (Ti, Pd, Mg) are hydrogenated, substantial out of plane expansion occurs. This expansion, which can be as high as 23% for Mg, effectively damages the film due to defect formation. Cyclic loading will continue the damage process until the film reaches a powdered state, thus significantly altering hydrogen loading behavior. This damage is a source of extrinsic hysteresis and decreases efficiency of the loading-unloading cycle [25]-[30]. Recent advances in epitaxial Mg film fabrication have enabled discovery of epitaxial phase decomposition after hydrogenation [31]. The ability to extend this effect to other metal-hydride systems will enable well controlled coherent nanophases in hydrogenated metallic films will offer insight into improving durability of these films as well as enabling more efficient hydrogenation by the possibility to minimize of hysteresis during hydrogenation. Unlike Mg, Pd is an attractive candidate material for analysis and characterization in ambient conditions since oxidation in air is of no concern.

While epitaxial effects and their influence on nanostructure modulation have been observed experimentally and confirmed theoretically in other material systems (thin piezoelectric films), the structure and its periodicity have not been well studied in epitaxial Pd thin films. Ordered coherent phases have been observed in bulk Pd foil after hydrogenation, but the influence of thin film epitaxy and hydrogenation parameters in Pd thin films have not been determined.

1.3 Dissertation goals and scope

The goal of this dissertation is twofold: (a) to fabricate transversely modulated metallic nanostructures via solid-solid (Pd-PdH) and liquid-solid phase decomposition (Ag-Si), and (b) to develop a thermodynamic model predicting control of hysteresis of hydrogen cycling in epitaxial thin films via modulated nanostructure decomposition. In principle, under the right formation conditions, it is possible for the ordered coherent phases to form transversely modulated nanostructures (TMNS), which are typically formed indirectly using selective deposition or removal techniques on a surface and not through direct synthesis at an interface. For purposes of practicality, the systems chosen thus far for investigation are Ag/Si (applicable to solar cells and microelectronics) and metals capable of volumetric hydrogen absorption, including Pd (applicable to energy storage and hydrogen sensing).

Pd thin films are grown epitaxially on single crystal substrate to form ordered coherent phases. Films are characterized in terms of crystallinity and surface morphology before and after hydrogen loading. It is expected that misfit strain between domains will manifest surface modulation (as shown in Figure 1.1), and this morphology can be characterized via atomic force microscopy. A thermodynamic theory predicts that formation of ordered coherent phases at the nanoscale can minimize or eliminate hysteresis during hydrogenation, thus improving the functionality of thin films as hydrogen storage mediums and sensors.

The effect of eutectic solidification on a single crystal “parent” phase will be studied along the interface of single crystal Si and polycrystalline Ag. A liquid composed of Ag and Si will form by way of interface diffusion. Scanning electron microscopy will be utilized to study the morphology and composition of resulting nanostructure formation and the effect of Si crystal orientation on structure morphology will be examined. The effect of Si native oxide on the interface behavior during processing will also be determined.

2 Literature Review

The effect of atomic structure and composition on material performance and functionality is not a novel concept. Modern microscopy and analysis techniques have enabled the understanding of material performance on the atomic scale and fabrication techniques, including nanoscale self assembly, are more recently being understood and used to design materials with not only novel atomic constituents but also unique nanostructure arrangement. Recent work has shown that optimized self assembled nanostructures can drastically improve active functional properties such as piezoelectricity [32].

Modern electronic devices, such as solar cells, generally use semiconductors and metals in order to produce, collect, or transport charge. The quality of the interface of these systems will optimize or limit the operating efficiency or influence the mechanical reliability of the device. Therefore, it is necessary to not only be aware of the nanostructure along a contact interface, but also understand the mechanism of formation so one can control the size and morphology to optimize efficiency and reliability [33]. Also, a good understanding of the nanostructure formation may facilitate new fabrication techniques, ie. processing and isolating the structures via chemical etching as opposed to optimizing design for a specific device.

The proposed research effort aims at developing transversely modulated nanostructures via thin film and thin layer decomposition. The effect of eutectic melting and epitaxial resolidification and also ordered metal hydride phase separation via coherent phase formation will be examined. Understanding classical eutectic theory of common systems as well as hydride formation in suitable metals is necessary for this undertaking and corresponding literature is discussed below. Fundamental knowledge of coherent phase formation in epitaxial films (polydomain formation) is necessary to understand the driving mechanisms of formation, and an overview of this phenomenon is shown below.

2.1 Self Assembly in Constrained Films

The study of phase transition in metals that is responsible for organized structural layout has been reported in the literature for decades (ie. martensitic transformation) [1]. This diffusionless transformation has more recently been considered in mechanically constrained thin films [34]. Equilibrium phase structure can be predicted theoretically via film misfit (Fig. 2.1). Misfit in a constrained film is analogous to a specific external applied stress, as exemplified in Figure 2.1, and can also be manifest via temperature change. On a practical level, the ability to design bimorph and trimorph films that consist of unstable phase-changing films may enable unique “smart composite” material behavior that presents novel mechanical and dynamic (damping) properties [34].

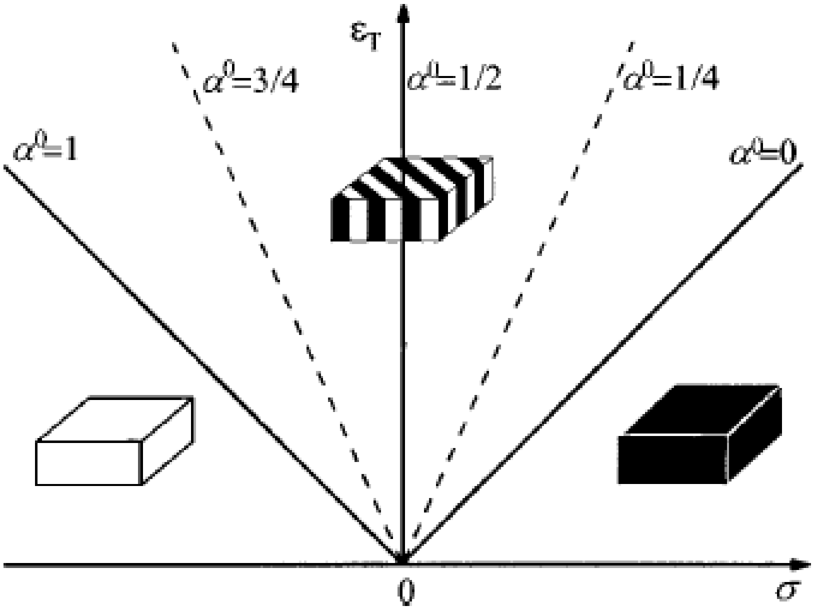

Figure 2.1 Domain stability map for orthorhombic-tetragonal transformation under external applied stress [35].

A theoretical framework, known as the theory of elastic domains, was developed that predicts polydomain heterostructure volume fraction (α) as a function of substrate-film (direct) elastic interaction and domain-domain (indirect) elastic interaction [6], [36], [37]. This class of thin film materials, polydomain heterostructures, form with a certain phase volume fraction to minimize total elastic energy in the film-substrate system. This model assumes coherency between both phases (Figure 2.2) and substrate, thus neglecting the effect of dislocation formation along interfaces. If other forms of energy relaxation (ie. dislocation formation) appear, the effect of polydomain formation will be mitigated or possibly absent. Film thickness also governs polydomain fraction, as its value has a direct influence on indirect elastic interaction. This phenomenon has been experimentally observed in oxide systems, more namely in $PbZrTiO_3$ film [38].

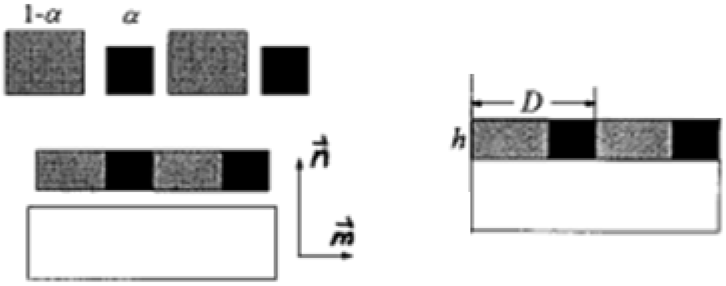

Figure 2.2 Coherent polydomain heterostructures with misfit strain between (black and gray) phases and substrate [6].

In an unrelaxed epitaxial film, strain energy is manifest by misfit strain between the lattice parameter of the film and lattice parameter of the substrate. These misfit strains can be calculated from the values given by example in Figure 2.3.

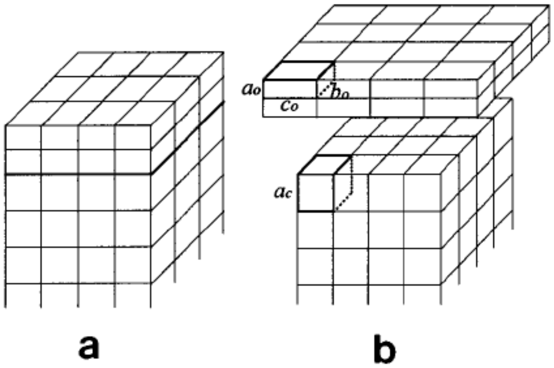

Figure 2.3 Definition of misfit strain: (a) epitaxial couple (b) freestanding film illustrating differences in lattice paremeters between orthorhombic and cubic phases [6].

More specifically, using the parameters in Figure 2.3, the misfit strain tensor for phase ***A*** can be expressed as:

$$\widehat{\varepsilon_A^M} = \begin{bmatrix} \frac{a_0-a_c}{a_c} & 0 & 0 \\ 0 & \frac{b_0-a_c}{a_c} & 0 \\ 0 & 0 & \frac{c_0-a_c}{a_c} \end{bmatrix} \tag{1.1}$$

where the indirect elastic energy between film and substrate is

$$e_A^M = \frac{1}{2}\widehat{\varepsilon_A^M}\boldsymbol{G}(\boldsymbol{n})\widehat{\varepsilon_A^M} \tag{1.2}$$

and $\boldsymbol{G}$, the planar modulus with normal plane $\boldsymbol{n}$,

$$\boldsymbol{G}(\boldsymbol{n}) = \boldsymbol{C} - \boldsymbol{Cn}(\boldsymbol{nCn})^{-\mathbf{1}}\boldsymbol{nC} \tag{1.3}$$

For phase B, the same formulation is used as shown above, except for the substitution of appropriate lattice parameters in the misfit strain matrix $\widehat{\varepsilon_B^M}$.

Similarly, direct interaction between phases with plane $\boldsymbol{m}$, is defined as

$$e^{DI} = \frac{1}{2}\hat{\boldsymbol{\varepsilon}}\boldsymbol{G}(\boldsymbol{m})\hat{\boldsymbol{\varepsilon}} \tag{1.4}$$

where the self-strain of transformation is

$$\hat{\boldsymbol{\varepsilon}} = \widehat{\varepsilon_B^M} - \widehat{\varepsilon_A^M} \tag{1.5}$$

The total elastic energy can then be summed as

$$\boldsymbol{e(\alpha) = \alpha e_A^M + (1-\alpha) e_B^M + \alpha(1-\alpha) e^I - \alpha(1-\alpha) e^{DI}} \tag{1.6}$$

where α is the volume fraction of phase A.

The balance of energies between the substrate (**n**) and phases (**m**) enables the stable coexistence of coherent two-phase state, as shown in Figure 2.2. However, in an open system such as Pd-PdH, the values of direct and indirect energy will change with increasing concentration and varying volume fraction of phases. The effect of indirect energy between incompatible phases may create an elastic instability, thus creating novel functional properties such as negative Young's modulus (Figure 2.4) and hysteresis-less gas absorption/desorption [39]. Improved properties in other systems, such as $BiFeO_3$, have been reported experimentally and validated theoretically as the effect of interface energies between phases and substrate [2], [40].

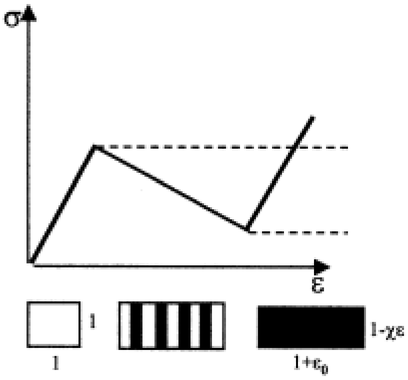

Figure 2.4 Strain controlled deformation of incompatible phase with negative effective elastic modulus [39].

In the case of an epitaxial ferroelectric film, such as $BiFeO_3$, the field induced response can be enhanced to due elastic instability and the movement of domains walls (or, in other words, the

the change in relative fraction of the phases). Due to interaction between film-sustrate and domain-domain interface interaction, as well as difference in relative polarization, the free energy of the two-phase state becomes a non-convex function, as shown in Figure 2.5.

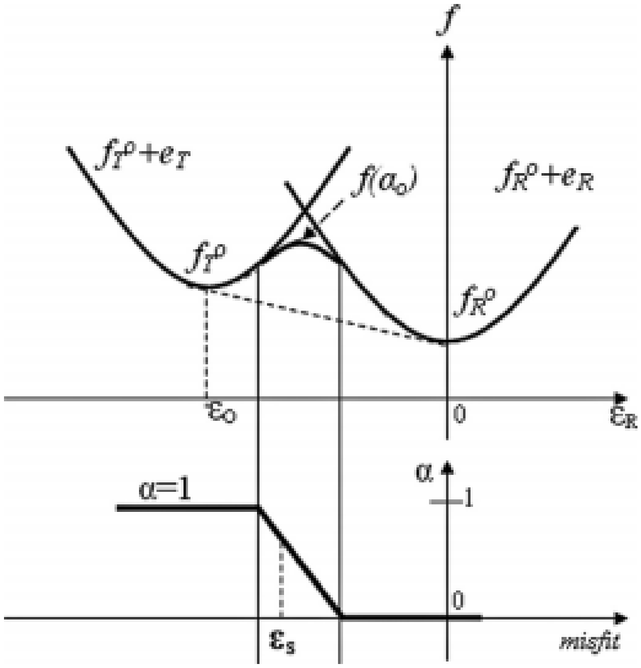

Figure 2.5 Free energies of phases as a function of substrate misfit and dependence of domain fraction on misfit [40].

2.2 Coherent Hydride Phase Formation in Metal Hydrides

Phase coherency in metal-hydride systems has been studied for decades, but only more recently has this phenomenon been studied in thin films, and more specifically, epitaxial thin films. Phase coherency in epitaxial Pd thin films is discussed in Chapter 4 and a model postulating improved functional response due to phase coherency (elimination of hysteresis) is present in Chapter 5.

Recently, hydride phase transformation with epitaxial interfaces was observed in epitaxial Mg thin film. This transformation proceeds by formation of 3 MgH_2 varients (Figure

2.6). It is suggested that the effect of coherent phase transformation in this hydride system will significantly alter the kinetics of hydride absorption [31].

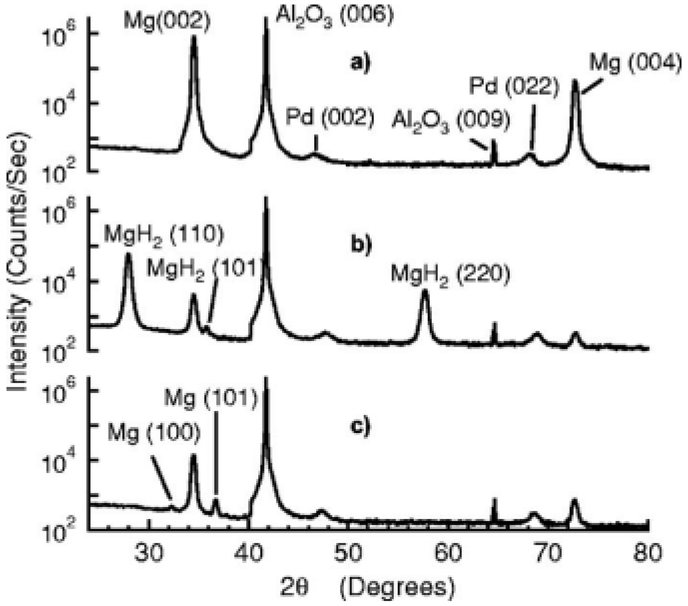

Figure 2.6 XRD spectra after film growth (a), after hydrogen absorption (b), and after hydrogen desorption (c) [31].

The formation of coherent nanostructure in metal-hydride systems is an important technological concept because it will enable improved performance in practical applications. This is due to the fact that the absorption-desorption cycle will be more efficient and predictable than incoherent phase decomposition.

2.2.1 The Pd-PdH System

Palladium (Pd) is a noble metal that possesses a FCC crystal structure. It displays several unique qualities which make it a candidate material for several hydrogen based technologies. Most significantly, it can absorb relatively large volumes of hydrogen at room temperature and low pressures (below atmospheric). In a fully occupied PdH unit cell (β phase), the phase transformation is isomorphic and the octahedral sites are fully occupied with a total of 4 H atoms in the unit cell. Its phase diagram consists of a large miscibility gap with two single phase regions, as well as the two-phase gap (Figure 2.7).

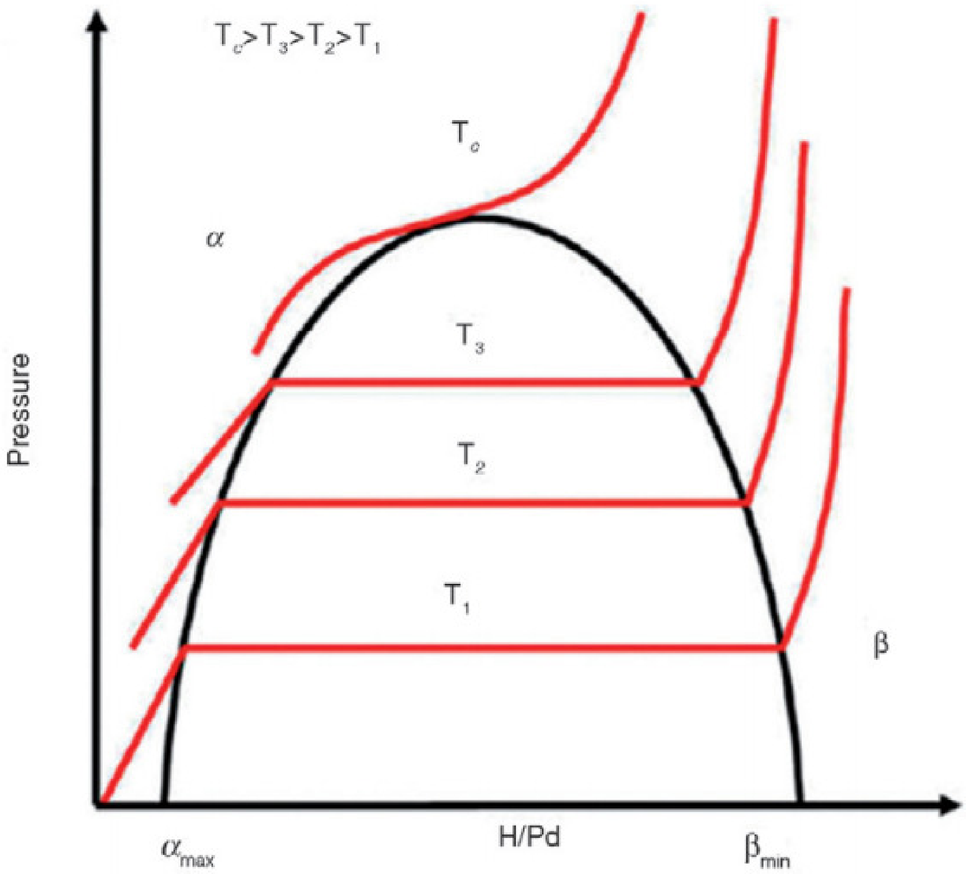

Figure 2.7 Phase diagram for PdH_x [41].

Pd is also unique in that it requires little to no activation energy to break apart H_2 into single atoms, thus requiring much less energy when compared to other metals for hydrogen absorption. Because of this behavior, Pd is often used as a surface catalyst for absorption of H into other metals that are capable of higher volumetric H concentration [41].

The urgency for sustainable energy production and storage is perhaps one of the greatest technical challenges of the current generation [41] and hydrogen gas has been identified as plausible alternative energy source due to its highly combustible nature. However, storing hydrogen successfully relies on 4 main aspects: storage capacity, charge and discharge rates, purity of H after storage, and maximum number of charge/discharge cycles. Some metals, such as Pd and Mg, have the capability to absorb large volumetric quantities of gaseous hydrogen (0.56% and 7.60%, respectively). In fact, Pd can absorb appreciable volumes at room temperature and pressure. Nevertheless, due to 10% volumetric expansion when converted fully to beta-phase hydride, full cycling damages the metal, eventually reducing it to a powder-like state. Being able to control the nature of hydride phase decomposition may enable cycling that is virtually fully reversible via coherent phase decomposition. Additionally, recent work has shown enhanced mechanical properties in Pd film with nanoscale twins [41], and using hydrogen absorption to creating ordered nanostructures may be a path towards similar mechanical behavior improvements.

Hydrogen purification is another process that can be improved via absorption in Pd. Hydrogen is usually produced by electrolysis of water or by the gasification of hydrocarbons which waste energy or produce pollutants, respectively, while absorption in Pd is selective with H purity of 99.99999% and can be used to isolate pure gas [41]. However, continued cycling of Pd membranes for gas purifying causes embrittlement and possible solutions to improve durability via substrate constraint and phase coherency will be addressed in this dissertation.

PdH was found to display superconductive properties at 9K when stoichiometric ratio $x=H/Pd = 1$ [42]. High temperature superconductivity of high concentration PdH (stoichiometric ratio $x=H/Pd \geq 1$) was discovered in Pd wire hydrogenated electrochemically, but hydride phase characterization has not been performed and the reason for superconducting behavior at high temperature is still largely unknown [43]-[45].

While the effect of hydrogenation on metals has been the subject of study for several decades, only more recently it has been proposed that hydrogen solubility in nanowires and thin films systems is governed by morphology and nanostructure of hydride phases and their relative stresses [46]. A recent study has described a novel R9 phase formed after hydrogenation of polycrystalline Pd film with single stacking faults located every {111} plane in the fcc Pd structure [47], [48]. These structural effects include absorption around the surface, inter metal matrix, and grain boundaries and edge dislocations (Figure 2.8). Fortunately, multiple parameters can be adjusted in thin film deposition techniques to tailor effects such as surface roughness, crystal orientation, grain size, defect density. Therefore, recent advances in thin film fabrication that enable high quality epitaxial growth present an opportunity to study the effect of phase formation in highly ordered metal crystal that is generally not commercially available or prohibitively expensive in bulk.

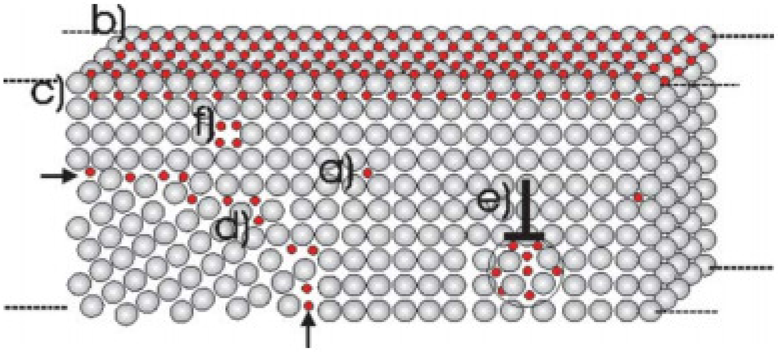

Figure 2.8 Schematic of defect in nanoscale thin film and accumulation of H atoms: (a) solubility in metal matrix, (b) and (c) surface and subsurface absorption, (d) and (f) grain boundary absorption, (e) absorption at edge dislocation often seen between film/substrate [46].

Hydrogenation of Mg and Pd commences with partially occupied octahedral sites in the lattice. At relatively low concentrations, the solution decomposes into a two phase mixture of low concentration with respect to H cells (α-phase) and high concentration with respect to H cells (β-phase). In the case of PdH, the transformation is isomorphic, with the cell retaining its cubic structure and increasing in volume due to the ~3.5% strain (Figure 2.9).

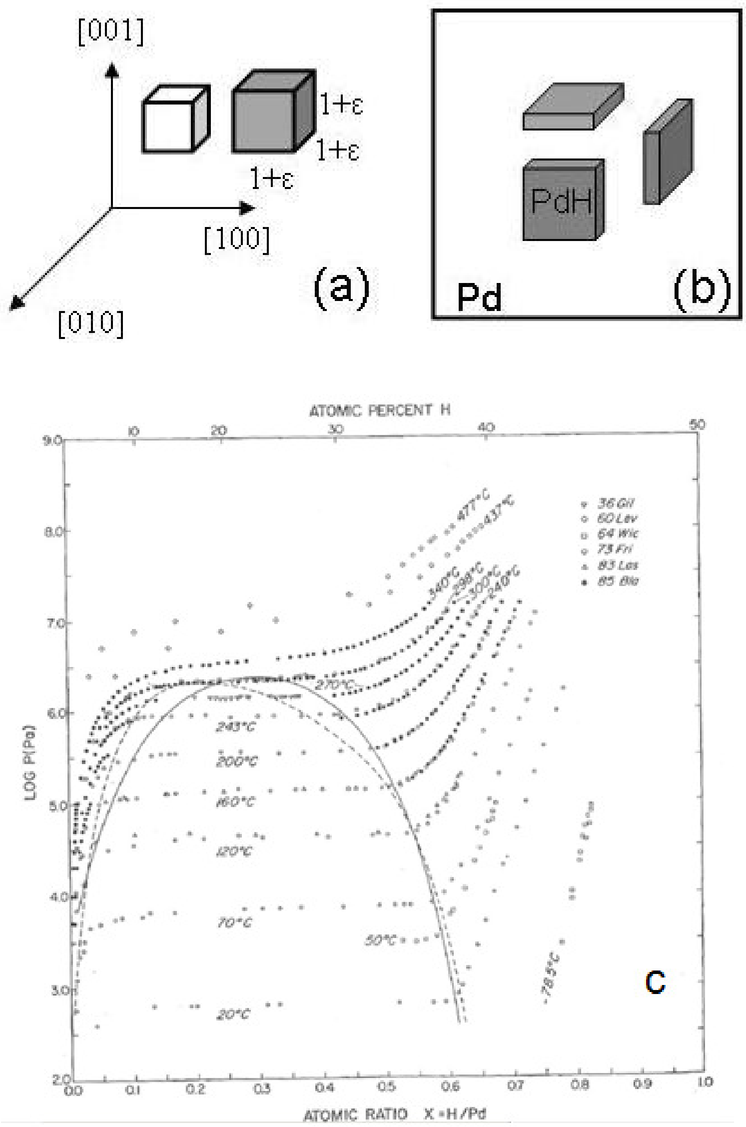

Figure 2.9 Self-strain (a) and equilibrium crystal orientation (b) of Pd-PdH transformation and (c) bulk Pd-H phase diagram [49].

The effect of processing conditions on coherent phase formation in the Pd-H system was considered as early as the 1970’s [50], [51]. This work by Ho et al. examined the effect of cooling partially hydrogenated Pd foil to liquid nitrogen temperatures in the TEM chamber. They observed coherent precipitates of both α and β phase (Figure 2.10) under certain concentrations after cooling. Unintuitively, a specimen processed with the concentration corresponding to the critical temperature (0.3 H) produced only dendritic precipitation, even after liquid nitrogen cooling. This is not expected since room temperature is below the theoretically predicted coherent miscibility gap [50]. The authors of this study believe that "quenching" to liquid N_2 temperatures in the TEM cooling stage is responsible for the coherent phase decomposition.

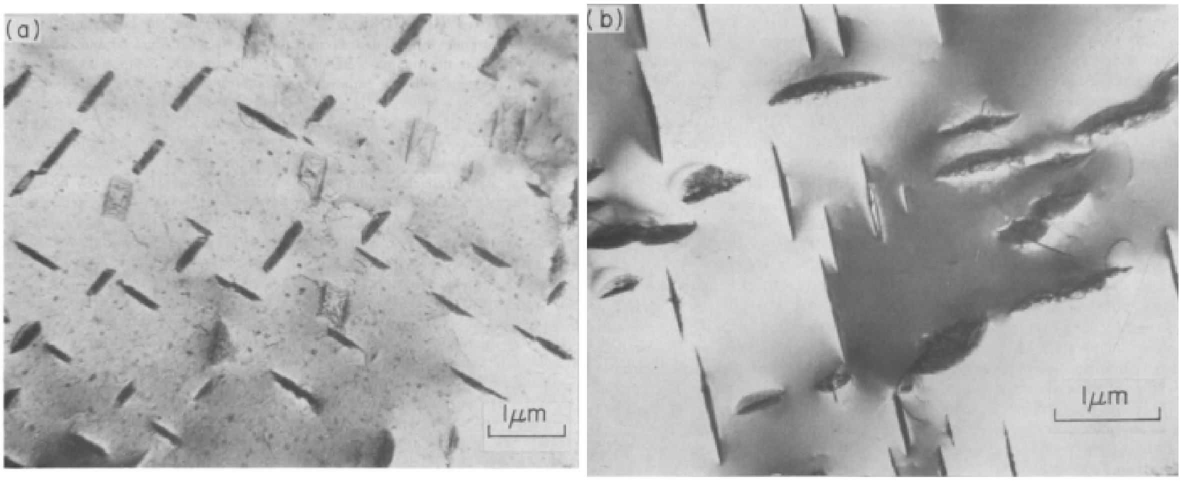

Figure 2.10 Coherent {100} plate-like precipitates after growth at liquid N_2 temperatures: (a) β precipitation in α matrix at 0.05 at. % H (b) α precipitation in β matrix at 0.6 at. % H [50].

It is also worthwhile to note that the work presented in [50] was highly variable; hydrogenating specimens under similar conditions sometimes produced no measureable hydride peak, while specimens exposed to ambient conditions would contain hydrogen for several weeks (this is unexpected as all hydrogen should desorb in a matter of hours). The orientation of coherent hydride plates is dependent on the crystallographic plane viewed. When viewing the

(111) plane in bulk crystal, one can expect colonies of plates at an angle of 60 degrees with other colonies (Figure 2.11). When considering an epitaxial film with (111) in-plane orientation, the plates can be expected to form at an angle of 60 degrees with the substrate as shown in Figure 2.11. Therefore, coherent phases formed in (111) film will be manifest similarly to (111) bulk (colony angles apart at 60 degrees).

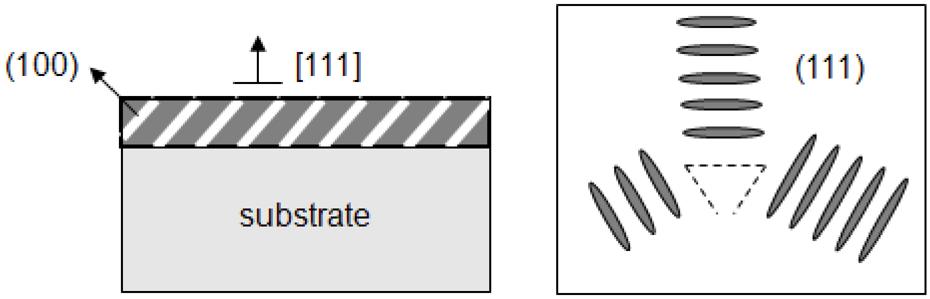

Figure 2.11 Orientation of hydride plate formation in Pd film (left) and bulk (right).

Structural evolution after hydrogenation has recently been studied in 150 nm Pd thin fimls with nanoscale growth twins [48]. Fcc metals with nanotwins have been shown to exhibit exemplary mechanical properties including high strength (1 GPa) and elevated ductility of 10% elongation [48]. These properties originate from {111} coherent twin boundaries and serve as barriers to glide dislocations. Nanocrystalline Pd films that have been hydrogenated and dehydrogenated have displayed an evolution in the arrangement of the {111} twin boundaries, with the boundaries becoming largely incoherent. Also, a martenite-type 9R phase was observed after dehydrogenation with misfit dislocations between the interface between the Pd matrix and the 9R (Figure 2.11) [48].

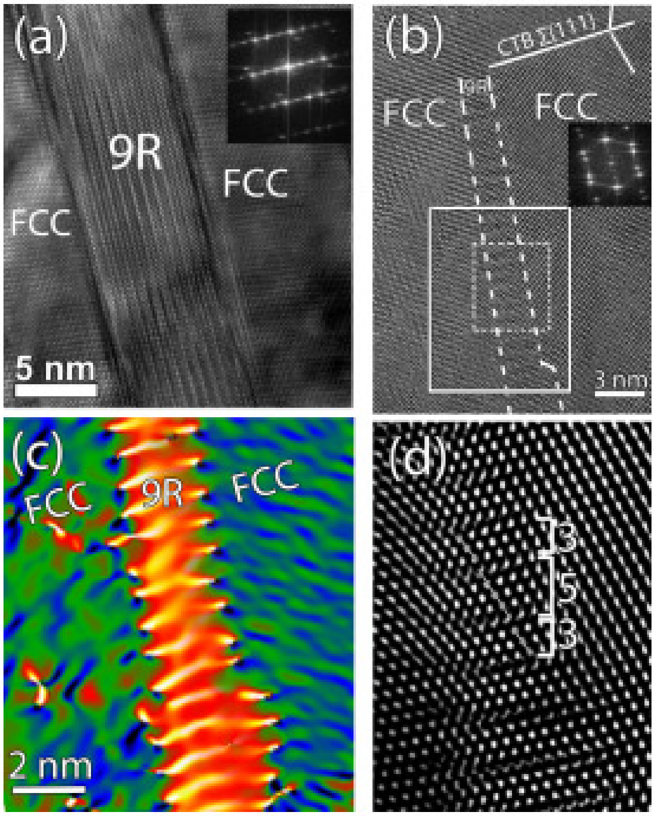

Figure 2.12 High res TEM micrograph of 9R phase in Pd matrix (a), high res TEM micrograph of {112} incoherent twin boundary (b), GPA map of 9R structure (c), and enlargement of twin boundary shown in (b) [48] .

Most studies considering the hydrogenation of bulk Pd and thin films perform loading at relatively low temperatures where composition crosses into the miscibility gap at relatively low concentration. At this state, small volumes of β-phase nucleate and due to high levels of misfit between the phases, microcracks form and continue to propagate after each loading sequence. It is important to note that if specimens are not processed in a similar fashion to [50], entering the miscilibility gap without quenching from the single phase states will typically create incoherent phases. This fracturing caused by incoherent precipitation is a source of *extrinsic* hysteresis, where hysteresis is commonly displayed as a gap between loading and unloading isotherms (Figure 2.14).

However, in the case of coherent phase transformation, hysteresis may still occur due to a macroscopic thermodynamic barrier that opposes formation of coherent phases due to elastic interaction between hydride and metal phases [52]-[54]. This type of hysteresis is referred to as *intrinsic* hysteresis. This energy barrier is considered macroscopic since its strength is proportional to the volume of the transformed hydride phase.

If hysteresis was due solely to plastic deformation, then its presence would decrease with increasing loading cycles as the film hardened. However, as shown in Figure 2.15, hysteresis remains even after many cycles, which should significantly increase dislocation density. Therefore, this intrinsic hysteresis must be due to coherent strain energy as hydrogen atoms enter vacancy sites [53].

The effect of hysteresis in Pd films during hydrogen loading has been studied experimentally by multiple research groups [55]-[62]. The critical point of the phase diagram (peak of the miscibility gap) is a determining factor in the occurrence of extrinsic hysteresis, as entering the miscibility gap induces incoherent β phase nucleation. Feenstra et al. [55] note that the elastic strain field in the Pd lattice around each dissolved H atom is responsible for existence of the miscibility gap and by altering the elastic effects (ie. clamping or compressing the specimen) one can control the miscibility behavior of the Pd-PdH system. This concept was proven experimentally (Figure 2.14), where hydrogenation of a 122 nm Pd film produced a noticeably narrower and shorter miscibility gap than a 320 nm film hydrogenated under similar conditions. The miscibility gap can be visualized as beginning and ending in the flat plateau regions of the isotherms where two phases coexist.

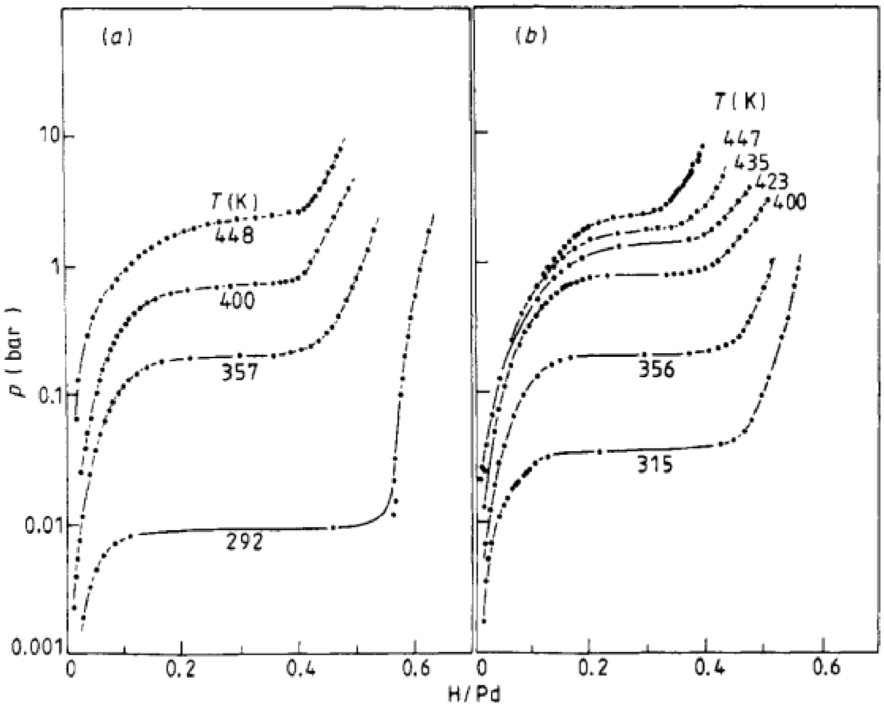

Figure 2.13 Absorption pressure-composition isotherms of (left) 320 nm PdH_x film and (right) 122 nm PdH_x film [55].

Salomons et al. discovered that isotherms measured in 300nm films were similar to bulk in terms of solubility limits and equilibrium pressure. 50nm films generally had narrower hysteresis with sloping of the plateau region, as displayed in Figure 2.14. The critical point for the thinner film was ~30K lower and was attributed to a reduction in H-H interaction due to substrate clamping [46]. They also noted that the 300nm film partially delaminated from the substrate after one loading cycle.

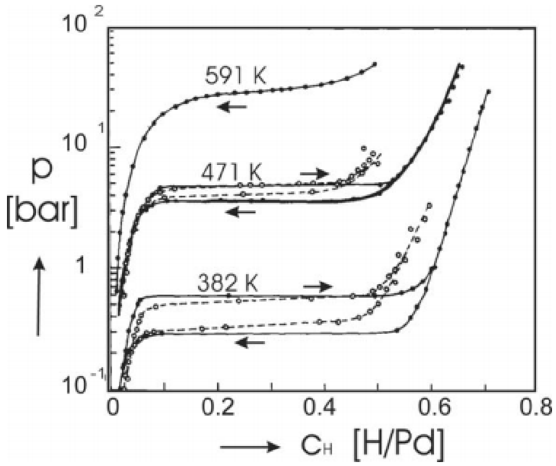

Figure 2.14 Pd-H isotherms for 300nm (black) and 50nm (dashed) films [46].

Pivak et al. [56] investigated the effect of clamping by hydrogenating Pd films with and without a Ti buffer layer; the buffer layer was used to increase mechanical interaction with the substrate. Hysteresis in the sapphire substrate films converges between cycles 11 and 17 (Figure 2.15) and is due to film delamination. With the Ti buffer layer, hysteresis is substantially increased, as strong biaxial stress prevents the film from buckling.

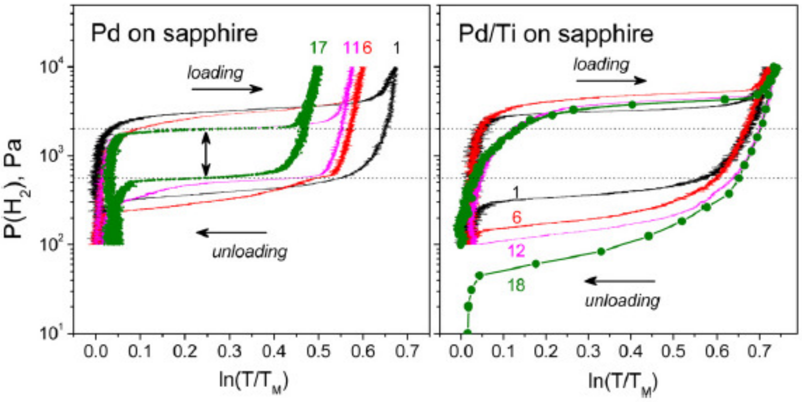

Figure 2.15 Pressure-composition isotherms for (left) Pd and (right) Pd-Ti film for several cycles. Vertical arrow represents hysteresis [56].

While hysteretic behavior has been considered in Pd films for decades, only more recently have researchers characterized possible phase coherency in-situ during hydrogen loading. Wagner et al. [62] studied α and β phase lattice expansion during gas phase hydrogenation. Their results in Figure 2.16 show monotonic increase of lattice parameters of both phases during loading and monotonic decrease during unloading but to their original value. From this, it is inferred that the phases remain coherent, as incoherent phase formation would be manifest through either: lack of lattice constant change after pressure increase/decrease or lack of lattice constant return after complete loading cycle. In other words, these manifestations would infer dislocation formation between the two phases.

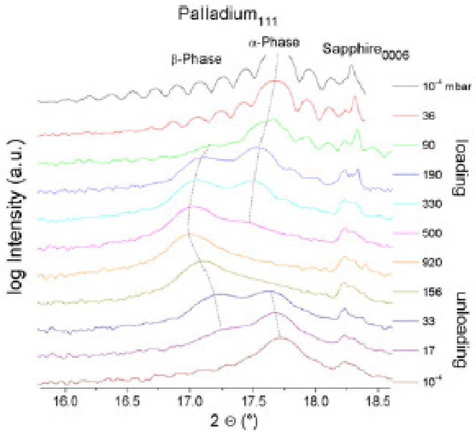

Figure 2.16 X-ray diffraction peak shift during gas-phase hydrogenation of 22.5nm polycrystalline film [62].

Wagner et al. furthermore quantified the lattice constants for both α and β phases during hydrogenation via in situ xray diffraction, displayed in Figure 2.16. They believe this data proves that films must be thinner than 34nm for full coherent transformation. The reason for this conclusion is that the 34nm α phase lattice parameter remains constant after stepping up hydrogen pressure (dashed circle in Figure 2.16), thus proving dislocation formation, as slipping around the phase boundary will cause the phase lattice parameter to remain unchanged.

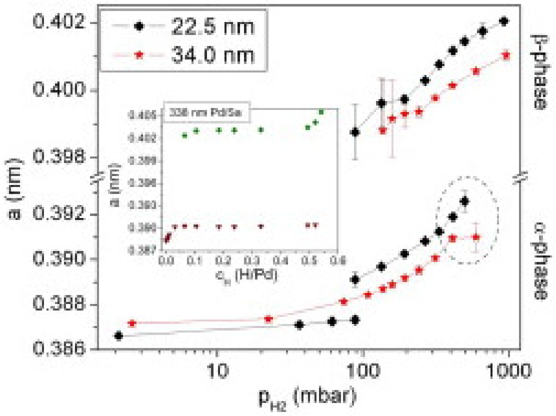

Figure 2.17 Lattice parameters of 22.5nm and 34nm Pd film during first hydrogenation cycle [62].

While significant work has been completed that attempts to characterize the nanostructure of Pd films during hydrogenation, it can be noted that virtually all studies have used multi-oriented, polycrystalline film. Recent work by Wagner et al. [57] describes how using a thin V buffer layer on top of sapphire substrate will induce epitaxial Pd film growth with (111) orientation. The goal of the proposed dissertation research is to fabricate high quality epitaxial films, as described in [57], and observe the effects of coherent phase formation.

Characterization of metallic hydride phases is difficult due to intrinic heating by electron sources (SEM, TEM). Surface morphology characterization in films may give insight into coherent phase formation if the phases are not close to being compatibile. This approach has also been used in closed-system ceramic films such as $BiFeO_3$ as well [2].

\

2.2.2 Structural Characterization of Metal Hydrides

Characterizing the structure and composition of metal-hydrides is ideally performed *in-situ*, as hydrogen content in these systems is not stable in the absence of partial pressure of hydrogen gas. Standard methods of structural characterization, including x-ray diffraction, have been engineering to enable high pressure gas phase hydrogenation inside of a x-ray diffraction setup [62]. While full dehydrogenation of a 50nm Pd thin film specimen generally takes up to 12 hours in ambient conditions (results shown in Chapter 4), removing gas pressure at elevated temperature will accelerate the dehydrogenation process as the hydrogen atoms will be much more mobile in the host metal matrix as diffusion will occur rapidly.

X-ray diffraction (XRD) is a non-destructive technique that is capable of characterizing crystal structure and can provide precise data on unit cell dimensions. An XRD setup generally consists of an x-ray tube, a sample holder, and an x-ray detector. The sample holder rotates in the path of the collimated x-ray beam at angle θ while the detector rotates at an angle 2θ. A schematic of XRD operation is shown in Figure 2.18.

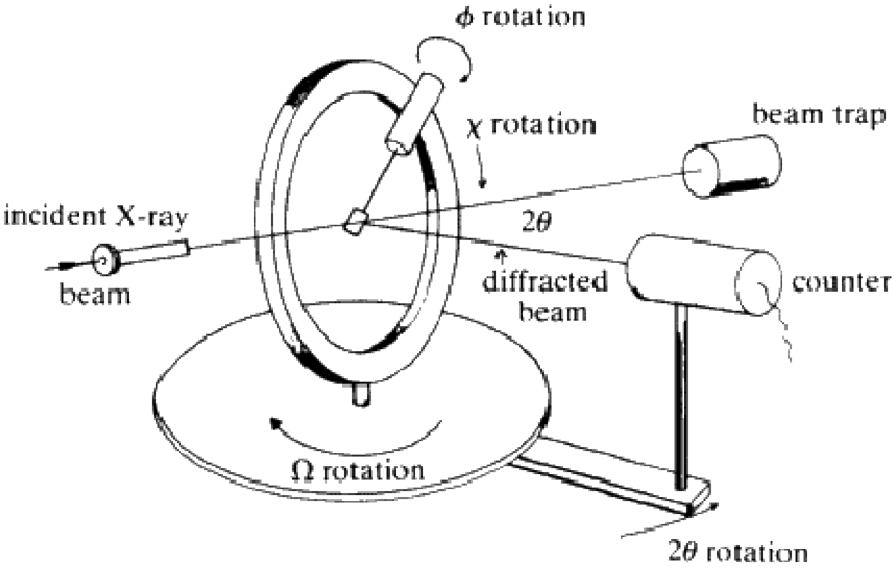

Figure 2.18 Schematic of x-ray diffractometer [58].

XRD correlates measured high intensity peaks of reflection to a given 2θ. More specifically, Bragg's law (Eq. 2.1), where *n* is an interger and λ is the wavelength of the incident wave, is used to correlate angle 2θ to *d*, the spacing between planes of atomic lattices within the material.

$$n\lambda = 2dsin\theta \tag{2.1}$$

Another pertinent property of thin films, texture, must be considered when fabricating and characterizing films for hydrogenation. A film is said to be highly textured if it is found preferentially oriented with respect to a certain reference frame. In other words, the crystals that constitute the film grow in alignment with the orientation of the substrate with minimal in plane rotation. This texture is investigated by rotating the χ angle 360° for a given φ angle that corresponds to one of the orientations of the crystal. As the χ angle is rotated, a highly textured film will produce distinct points in the 2θ-χ space, with the number depending on the symmetry of the crystal structure. This technique is used in this dissertation to confirm epitaxy in the Pd thin films.

Another powerful structural characterization technique, transmission electron microscopy (TEM), has been utilized to image and characterize hydride phases in Pd [50] as well as other metal-hydride systems. This microscopy technique streams a high energy electron beam through a very thin specimen (~100 nm thick). TEMs are capable of much higher resolution than optical microscopes due to the incredibly small wavelength of electrons compared to visible light. TEMs create images by bombarding the prepared specimen with a high energy beam of electrons. These electrons pass through the specimen and the image is collected on a detector, allowing up to atomic resolution. TEM also enables electron diffraction *in-situ*, enabling localized structural characterization.

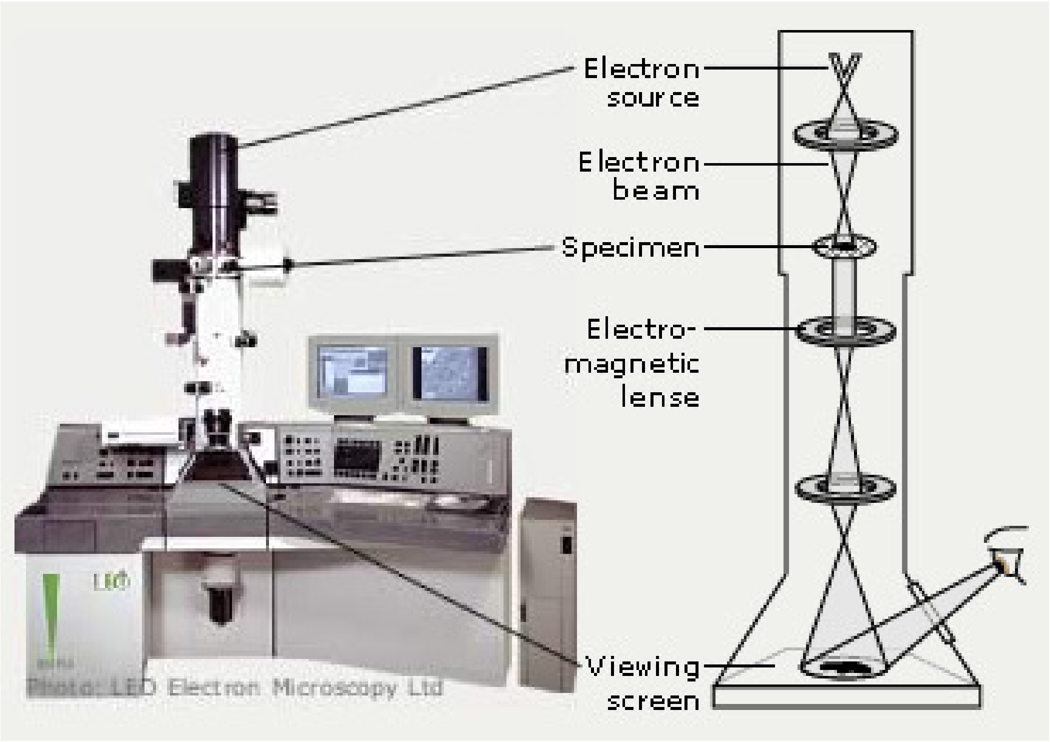

Figure 2.19 Schematic of general operating principle of transmission electron microscopy [59].

However, aside from the issue of hydride decomposition in ambient conditions or vacuum, the high energy electron beam de-stabilizes the interstitial hydrogen atoms and causes them to escape the metal matrix in a matter of seconds to minutes. This phenomenon has been observed in [50], where coherent PdH plates are imaged via TEM and a series of chronological images shows full decomposition within 2-3 minutes of electron beam exposure (Figure 2.20).

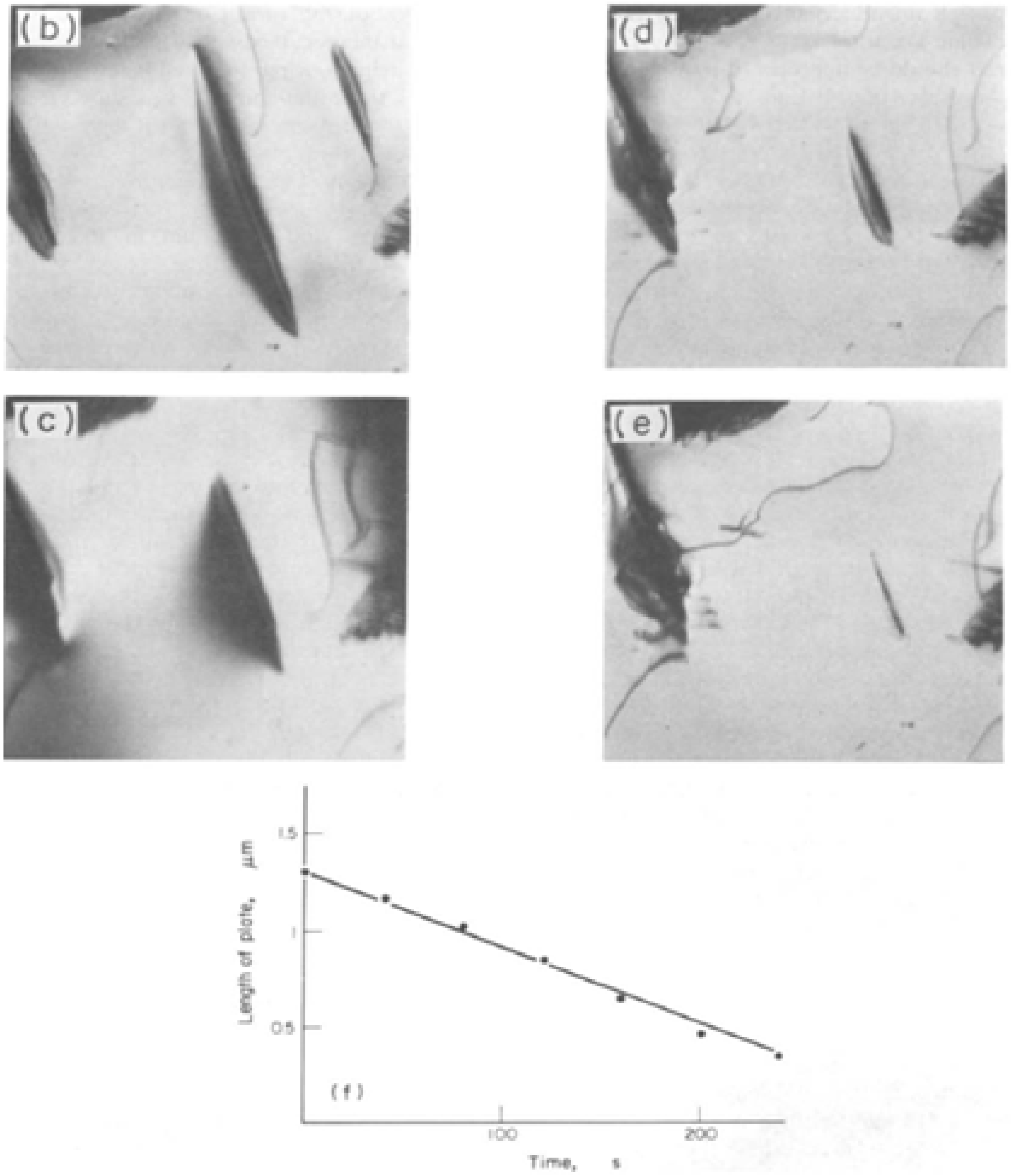

Figure 2.20 Decomposition of PdH plates under electron beam expsosure (b-e) and linear relation between beam exposure time and length of plate (bottom) [50].

Atomic force microscopy (AFM) is another non-destructive characterization technique. This method utilizes a small cantilever with a sharpened tip that has a radius on the order of tens of nm. The cantilever is excited harmonically at its resonance frequency at a close distance to the sample surface. As the surface becomes closer or farther from the tip, the frequency of the beam changes and the control system moves the beam up or down to lock in the resonant frequency. The cantilever deflection is measured by laser reflection that is collected in a quadrant diode (Figure 2.21). This method can be used to gain insight into phase morphology as there will be height discrepancy between phases due to elastic incompatibility and is utilized in this dissertation to characterize PdH phase morphology in epitaxial Pd films. However, this technique can only be applied in ambient conditions and exact hydrogen concentration will not be known since it begins to dissociate immediately after being removed from the hydrogenation chamber.

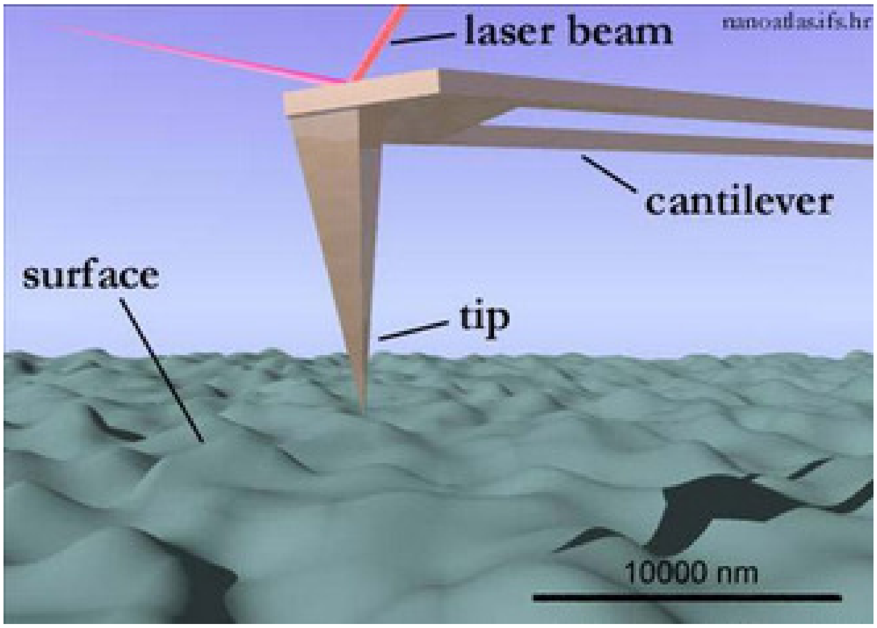

Figure 2.21 Schematic of vibrating cantilever used in atomic force microscopy [60].

The effect of surface change due to hydrogenation of Pd thin films has been studied *in-situ* via AFM [24]. This study considered 165nm multi-oriented Pd thin films loaded with 1

MPa of hydrogen pressure at room temperature. This work showed grain roughening and enlarging upon one complete loading cycle. The work shown in [24] is in accordance to what is observed and described in Chapter 4 of this dissertation (for room temperature hydrogenation). The results presented in this dissertation extend on those found in [24], as high temperature hydrogenation is performed and novel surface morphology is characterized.

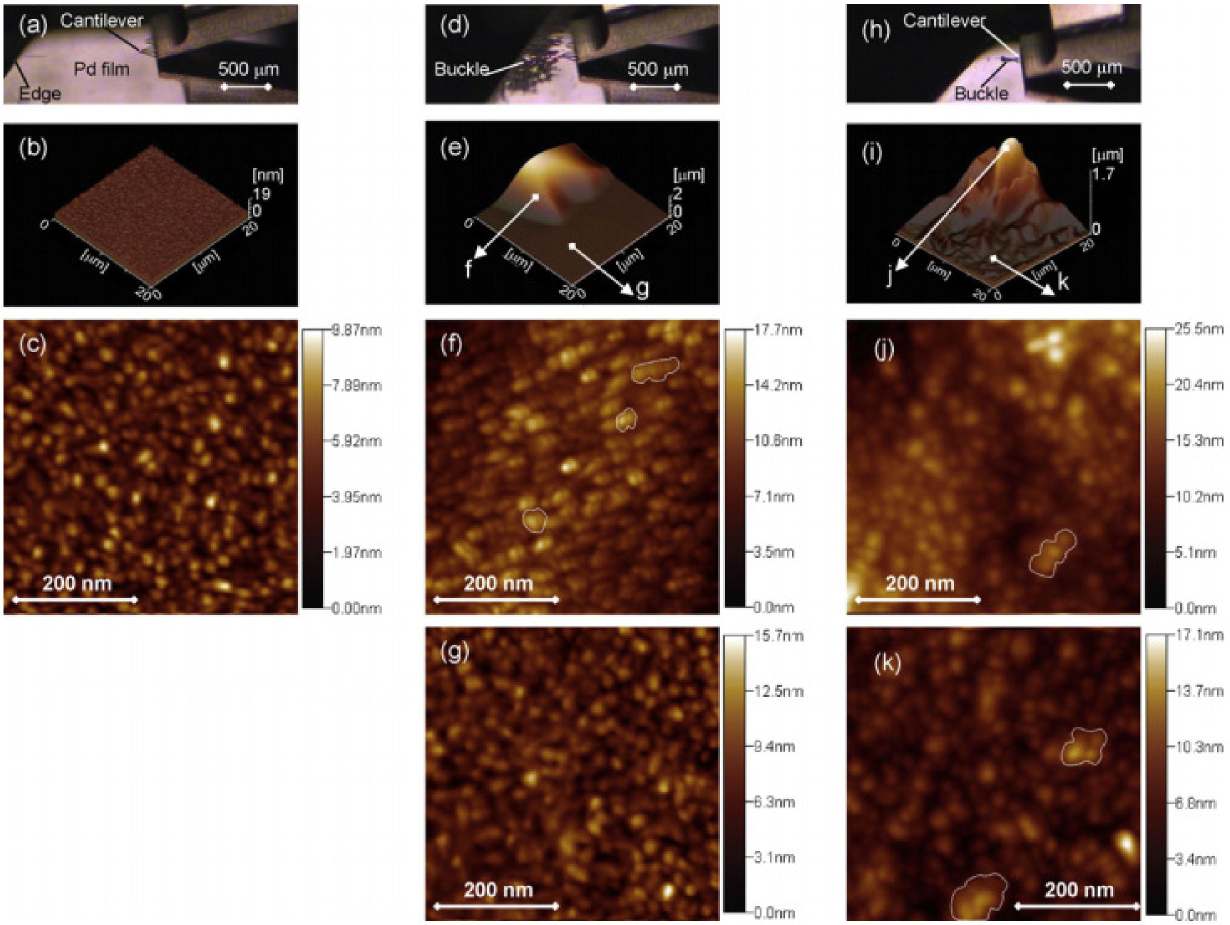

Figure 2.22 AFM micrographs of Pd thin film (a-c) as deposited, (d-g) during hydrogenation at 1MPa, (h-k) after complete desorption of hydrogen [24].

The methods of operation for the techniques listed above make direct characterization of hydride content and crystalline structure at high temperature a difficult proposition. *In-situ* analysis is necessary for complete certainty at a given concentration, as small volumes of H will begin to escape even at room temperature under zero partial pressure. On the other hand, retrofitting existing equipment (XRD, AFM) to operate under high H pressure and high temperature is not trivial, as these conditions can cause severe damage to the instruments due to hydrogen embrittlement.

Taking these considerations into account, AFM and XRD analysis under ambient conditions will be utilized to characterize the effect of hydride phase decomposition in the epitaxial Pd films. While these methods won't provide data with complete certainty for a given concentration under particular loading conditions (some H will escape the film upon removal of pressure), they will allow realization of major trends of hydrogenation of epitaxial Pd films under varying conditions, such as presence of hydride phase and also existence of modulated ordered surface structure

2.2.3 Structural Changes in Epitaxial Rare Earth Films after Hydrogenation

Northmann et al. [63] characterized the effects of hydrogenation on Nb thin films and captured changes in surface morphology via in-situ STM. After finite element modeling, they conclude that the small islands in Figure 2.23 (b) are coherent while the elongated ones are partially coherent. It is also inferred from the FEA results that the critical size of hydride precipitate to transform from coherent to semi-coherent is controlled by the balance of elastic energy stored around the precipitate-matrix boundary and the necessary energy for dislocation formation.

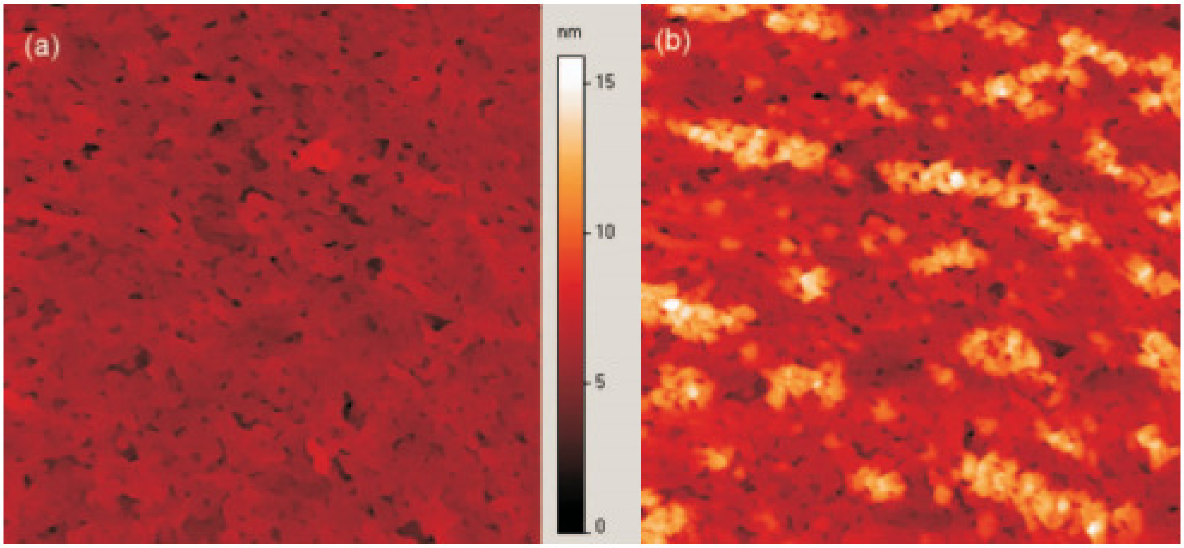

Figure 2.23 Initial 80nm Nb film surface morphology (a) and hydrogenated Nb film surface at 9e-5 Pa H pressure (b) [63].

Epitaxial HoH_x and YH_x films exhibit interesting changes in structural and optical properties upon hydrogenation [64]-[70]. More specifically, self organized ridge networks have been observed on the surface of these epitaxial films (Figure 2.24). These structures form due to phase decomposition of hydride phases, transforming from metallic to semiconducting-like phases and exhibit switchable-mirror effects; the differing hydride phases present substantially different light transmission properties [67]. Epitaxial film growth is necessary induce structured domains that can be utilized as switchable pixels or switchable mirrors [65].

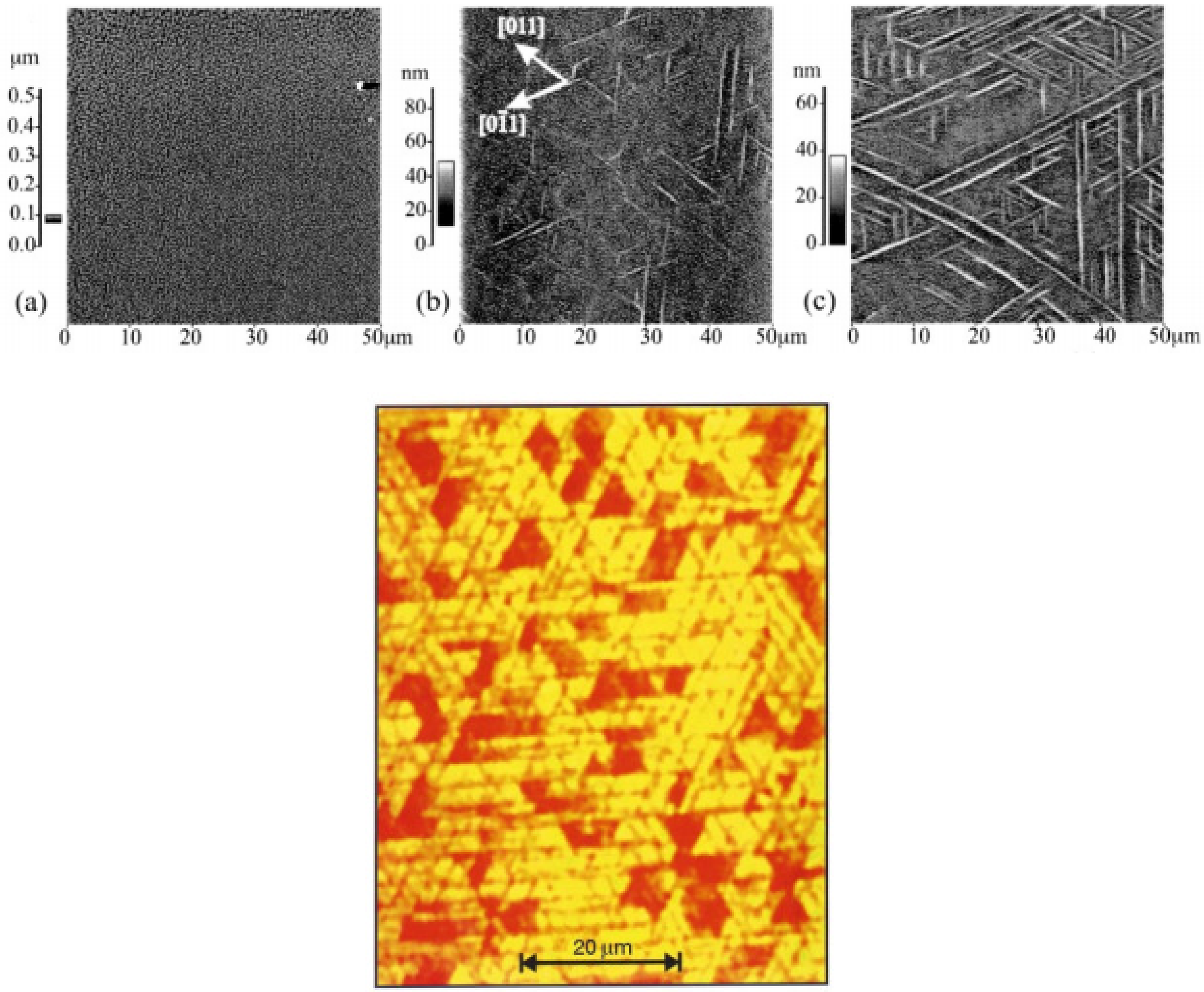

Figure 2.24 AFM topography of (a) as grown Ho film (b) dihydride Ho film (c) trihydride Ho film displaying ridge networks with varying hydride structure [64] and optical domain switching via hydride phase decomposition in YtH thin epitaxial film (bottom) [65].

It is possible to tune the height and domain spacing of the ridges by varying film thickness (Figure 2.25) [68]. The constraint by the substrate is said to lead to large compressive stresses during hydrogenation which will diminish as the thickness of the film increases. This phenomenon is displayed in the Pd-PdH system (Chapter 4), where increased film thickness leads to larger and denser ordered surface structures.

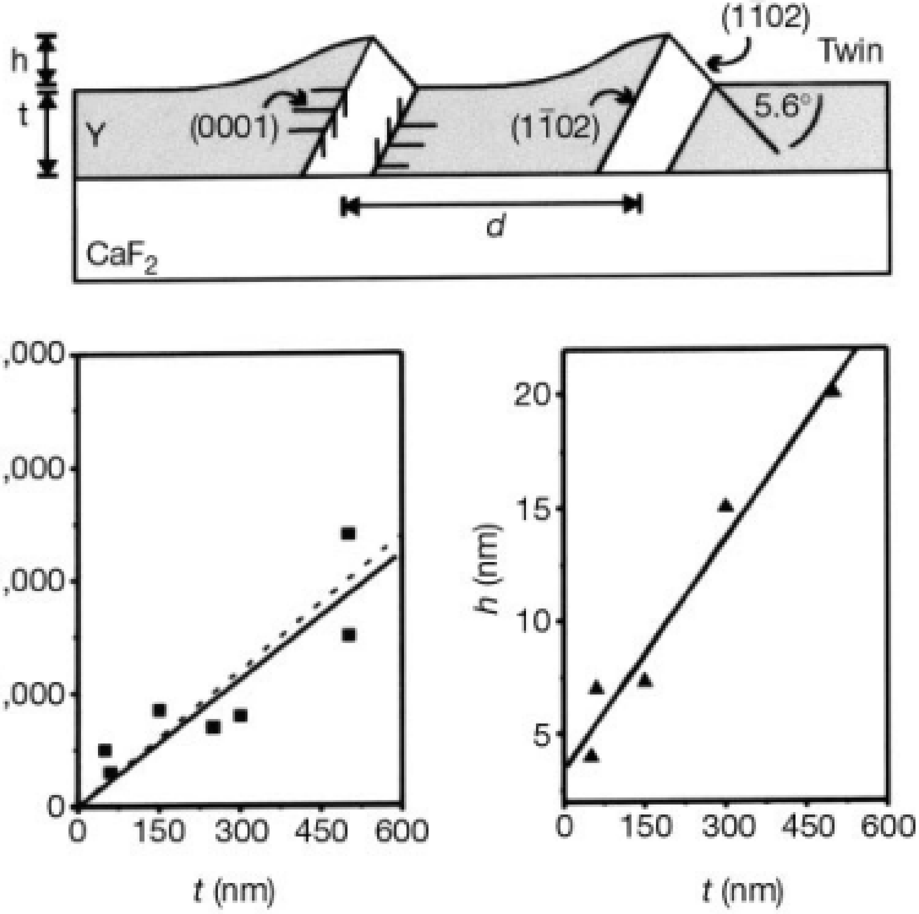

Figure 2.25 Schematic representation of ridge pattern created by twinning caused by in plane expansion (top) and film thickness vs ridge period *d* and ridge elevation [68].

2.2.4 Thermodynamics of Metal-Hydride Transformation with Coherent Interfaces

Schwarz et al. [52], [53] developed a thermodynamic theory describing the effect of phase coherency on phase evolution of metal-hydride systems. This theory is based on the absorption and desorption of interstitial atoms in a crystalline host which proceed to form two phases with different compositions. Their analysis shows that chemical potential within the two phase coherent region is a linear function and not a constant, which is a source of intrinsic hysteresis.

2.3 Ag-Si Interface

The Ag-Si system is an example of a simple eutectic with a temperature of ~835K and corresponding compositions 97 wt.% Ag and 3 wt.% Si (Figure 2.26). One way to achieve such a eutectic mixture is to create a diffusion couple and heat under appropriate temperature so that neither species melts homogeneously, but rather diffuses to form the eutectic composition and thus melt below the bulk melting temperature of both constituents. The motivation to use such a diffusion couple it to create a thin eutectic liquid layer on top of a single crystal Si wafer and observe effects of two phase solidification on single crystal substrate. As shown in Chapter 3, the presence of native oxide on the Si surface affects the diffusion rate between Ag and Si, acting as a semi-permeable diffusion barrier. Furthermore, annealing the diffusion couple in high vacuum as well as air established that only native oxide (not a thickened layer via annealing in air) is not sufficient to retard substantial diffusion between Si and Ag. Experimental work by McBrayer et al. [71] has shown that Ag diffusion through native Si oxide is suppressed in vacuum, but observed when heated in N_2 atmosphere as low as 50 Torr. Completed work shown later in this proposal will extend this concept, showing classical eutectic melting and solidification when native oxide is stripped and the couple is processed under high vacuum.

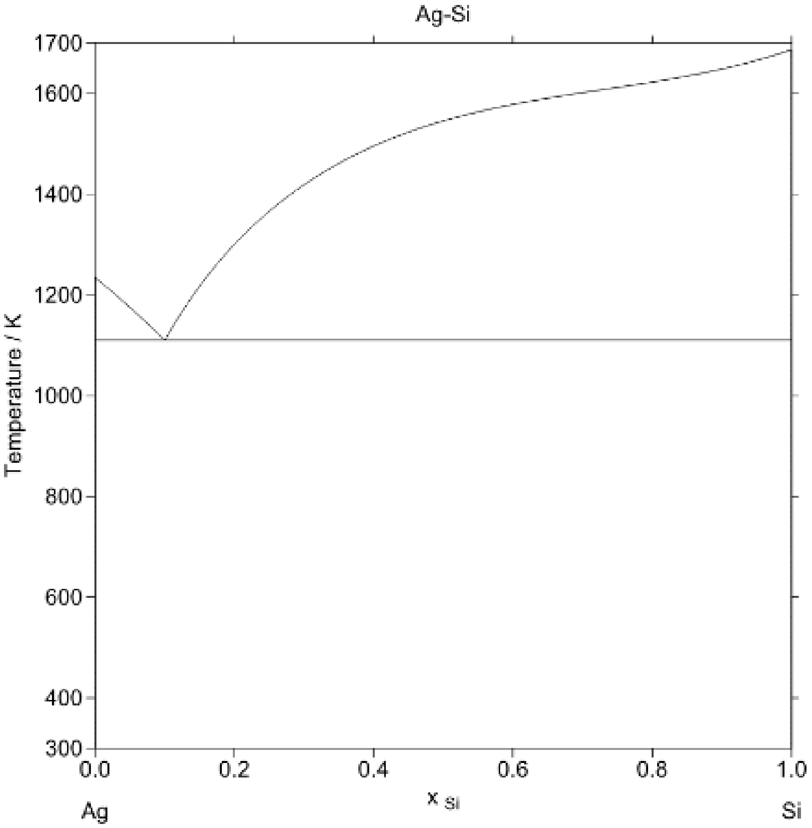

Figure 2.26 Phase diagram for Ag-Si system [66].

The nature of the Si-Ag interface, more specifically the (111) Si interface, has been a subject of discussion for many years [72]-[78]. These studies investigated the structure of Ag recrystallized on various Si surfaces. Further studies showed that annealing buried Ag-Si interfaces at temperatures over 200°C resulted in interfacial configurations not generally associated with the (111) Si surface [79], [80].

For the purpose of this dissertation, the effect of interface diffusion of the Ag-Si system will be seen as an opportunity to observe eutectic liquid recrystallization on single crystal Si, and also to observe the effect of native oxide as well as processing environment on interface morphology.

2.3.1 Ag-Si Solar Cell Contacts

The integrity of the interface between a Ag-Si couple has been the subject of extensive study in the solar cell community for many years [81]. This is due to the fact that an efficient technique to create an ohmic contact between emitter and electrode of the cell is to screen print a doped Ag paste layer and fire to metallize the contact. This paste generally is comprised of Ag powder, glass frit (generally containing an oxide), organic binder, and solvent. The glass frit layer is seen as crucial since it etches through the reflective SiN_x layer, thus enabling electrical contact between emitter and electrode [81]. Currently, almost all industrially produced solar cells utilize screen printed Ag paste for metallization of the front contact [82].

Ballif et al. characterized the interface structure of a Si-Ag paste couple after annealing [33], [83]. The paste was commercially available and contained lead borosilicate glass. The diffraction patterns in Figure 2.27 reveal an epitaxial relation between the Ag crystallite (P2) and the bulk Si wafer.

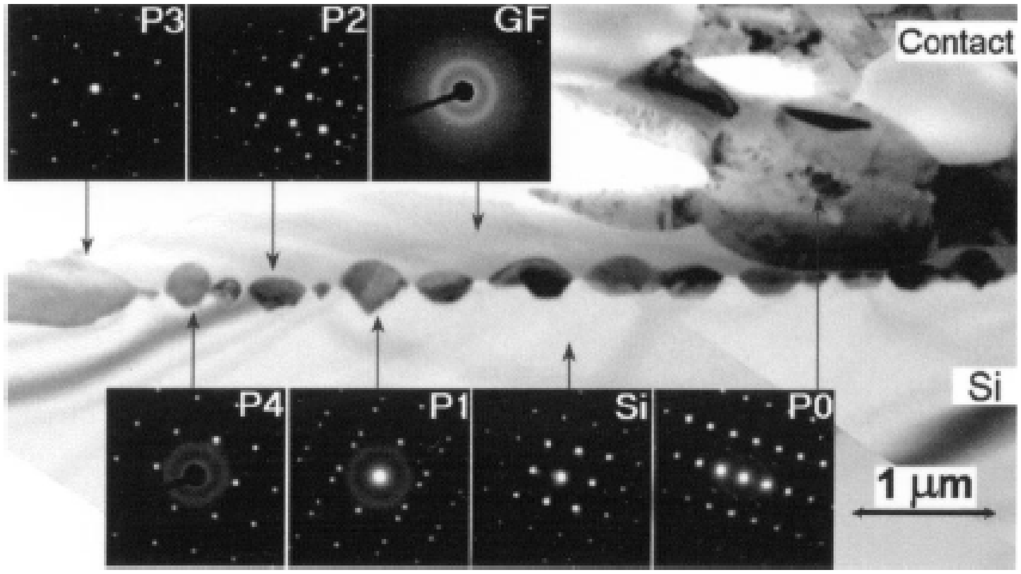

Figure 2.27 Cross sectional TEM image of Ag-Si contact. Different phases are indetified by their diffraction pattern [33].

Ballif et al. suggest a reaction of $Si + 2PbO \rightarrow SiO_2 + 2Pb$ that contributes to the etching of Si. They claim that the glass frit layer etches away the Si, and upon cooling the Si recrystallizes epitaxially on the wafer, with Ag crystalling epitaxially between the regrown Si.

The motivation of controlling Ag-Si interface morphology in the solar cell community is to specifically tailor contact resistance between Ag contact and Si emitter. As previously mentioned, doped paste is commonly used to metallize the emitter, and glass frit in the paste enables etching through the antireflective coating. However, this glassy layer impedes cell performance after firing in that it acts as an insulating barrier between the embedded Ag and bulk Ag from the paste [84].

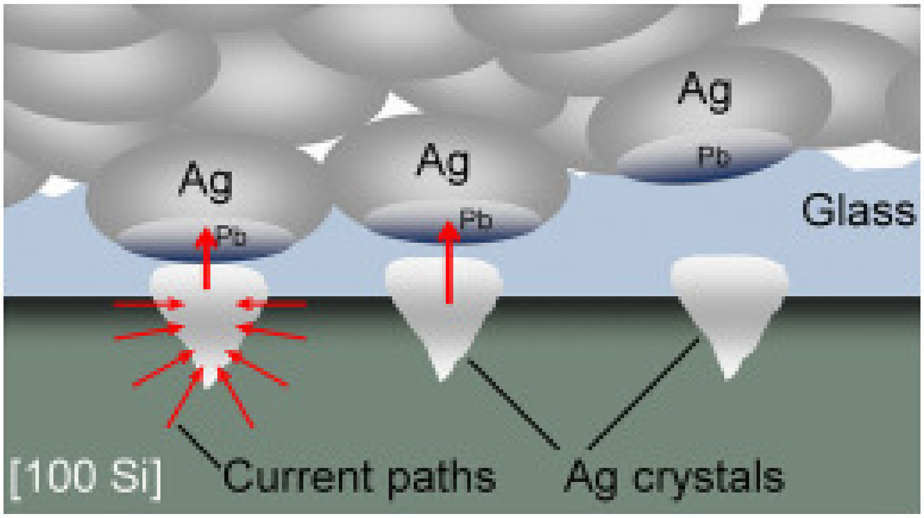

Figure 2.28 Schematic of interface of Ag paste and Si emitter after firing. Red arrows indicate charge transport; thick glass layer impedes conductivity [84].

The effect of Ag crystallite formation geometry and crystal structure on electronic structure has been considered via *ab initio* calculations and compared to experimental TEM observations [85]. These calculations were used to determine the correlation between Schottky barrier height and equilibrium atomic arrangement in epitaxial Ag-Si interfaces.

Experimental results shown in [85] display morphology and structure of epitaxial Ag crystallites embedded in Si wafer. The Si wafers were prepared by HF etching to clean the surface and SiN_x was deposited by direct plasma PECVD. Ag paste was used as a metallization contact and contained Ag particles, glass frit, solvents, and also binding agents. The diffraction patterns shown in Figure 2.29 show a 3 to 4 ratio between the Ag and Si unit cells, proving almost perfect lattice matching.

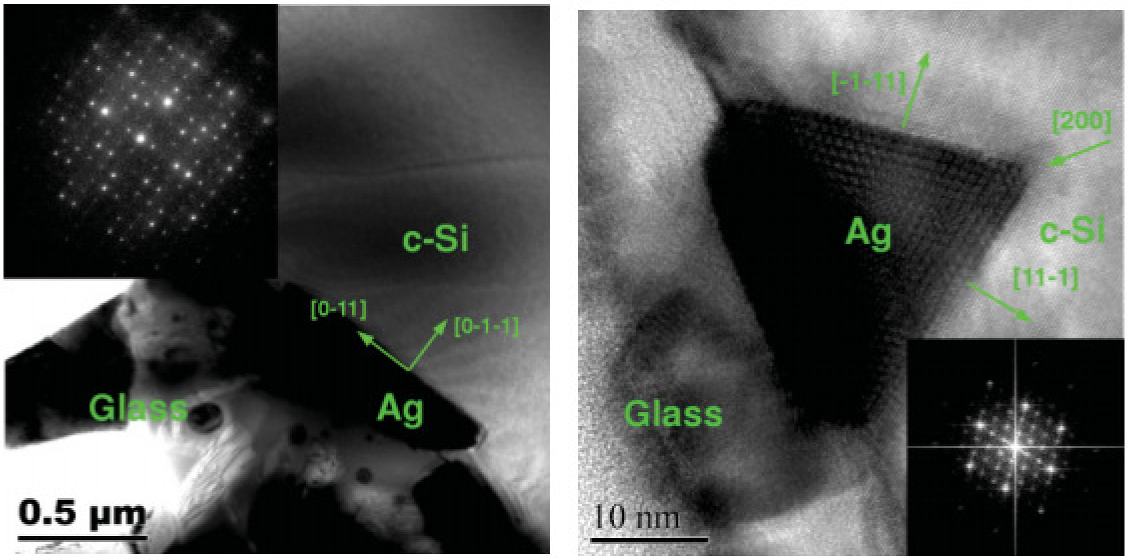

Figure 2.29 Bright field TEM micrographs of Ag crystallites in (111) (left) and (100) (right) Si [85].

The work in the following chapter expands on the references shown in this section. More specifically, it is shown that interfacial epitaxial Ag nanostructures can be formed without the use of doped Ag paste. It was determined that annealing a heterostructure composed of Ag foil and Si wafer in an oxygen rich environment (air) is necessary to achieve similar results, which can be applied to applications including solar cell metallization.

3 Effect of Native Oxide on Ag Nanostructure growth along the Interface of a Ag – Oxidized Si Heterostructure

To investigate the effect of eutectic liquid solidifying on a crystal substrate, a Ag-Si diffusion couple was heated above the eutectic melting point but below the bulk melting temperature of Ag. This was done with the intent of a thin eutectic liquid layer forming via diffusion and then solidifying on the Si crystal. Specimens were processed in high vacuum as well as air to determine the effect of oxide formation on interfacial melting and crystallization. Furthermore, specimens with and without native SiO_2 were annealed in vacuum to determine the role of the oxide layer on interfacial melting and solidification. In the case with intact native oxide annealed in vacuum, as well as annealing in air, a possible ternary system reaction along the interface ensues. Epitaxial Ag nanostructures were observed embedded in the Si wafer after annealing in air and the effect of Si crystal orientation of structure morphology was determined [5].

3.1.1 Experimental Overview

For this study, the effect of Si native oxide layer and annealing environment (in air or vacuum) on the Ag-Si interface is examined. More specifically, annealing the diffusion couple in air results in epitaxial Ag nanostructure formation, suggesting annealing environment, not only oxides found in commercially available Ag paste, influences nanostructure formation seen in [33], [83], [86], [87]. Also, it is discovered that initial (100) planar interface is a necessary condition for epitaxial pyramid crystal growth; (111) orientation results in flat Ag structures that etch into the Si surface.

Silicon wafers of (100) and (111) orientation were obtained from Mitsubishi Silicon America and Ag foil 0.1 mm thick was obtained from Alfa-Aesar (Ward Hill, MA) and used in all experiments. The specimens were created by placing a small piece of silver foil between the polished sides of two pieces of silicon wafers with the same crystal structure. The contact area of the layers was ~25mm^2. Two sets of heterostructures were studied: one containing Si with native oxide and the other containing Si stripped of the oxide layer. To create the oxide-free specimens, (100) and (111) Si wafer was cleaned in hydrofluoric acid and then stacked with Ag foil. These specimens were then clamped in a specimen holder, placed in a quartz tube, and pumped down to a vacuum pressure of approximately 10^{-9} torr. For native oxide specimens processed in air, a weight of 620 grams was placed on top of each specimen during the thermal process to ensure acceptable contact area between the layers. Experiments were performed by the following thermal process: ramping the oven temperature from ambient up to the desired temperature in a period of 3 hours, holding constant for a prescribed amount of time, and then allowing passive cooling. For characterization, all specimens were mounted in epoxy. To obtain cross sections of the interface, the mounted specimens were mechanically polished.

Furthermore, (100) oxidized specimens were mechanically ground and then etched in aqueous KOH to dissolve part of the Si substrate and reveal a plane view of Ag nanostructures embedded in Si along the interface (processing schematic shown in Figure 3.1. Afterwards, the exposed interface was analyzed to observe structural growth. Specimens were analyzed using a Hitachi S-3400 scanning electron microscope with all images obtained at room temperature.

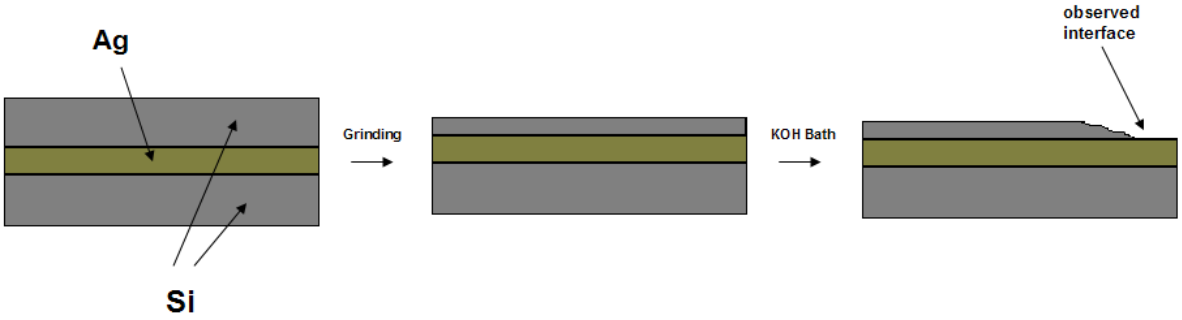

Figure 3.1 Processing schematic of etching sequence for interfacial observation of annealed Ag-Si heterostructure.

Specimens were also processed at a temperature of 1000° Celsius in air to observe solidification characteristics after melting the Ag foil. Additionally, specimens were prepared at 800° Celsius to observe interfacial properties when heated below the eutectic temperature of the system. An 800° Celsius foil sample was quenched to examine the possibility of contact melting.

The specimens stripped of native oxide were processed in an ampule under vacuum pressure at 5 degrees above the eutectic temperature (845° C) for 1 hour. The ampule, shown in Figure 3.2, is composed of quartz tubing closed on one end. The specimen was loaded by placing the Ag-Si heterostructure between two pieces of steel rod to maintain interfacial contact between the Ag and Si. A small piece of quartz tubing was melted onto the open end of the tube and attached to a vacuum pump. The ampule was allowed to vacuum down overnight and a pressure of 1e-9 Torr was achieved. After processing, the ampule was fractured in a clamp and the specimen was collected. After annealing at 5 degrees above the eutectic temperature (845° C) for 1 hour in vacuum, solidified eutectic liquid with a plane interface with the Si substrate contained a distribution of Si platelets with a total concentration close to the equilibrium eutectic composition (Figure 3.6).

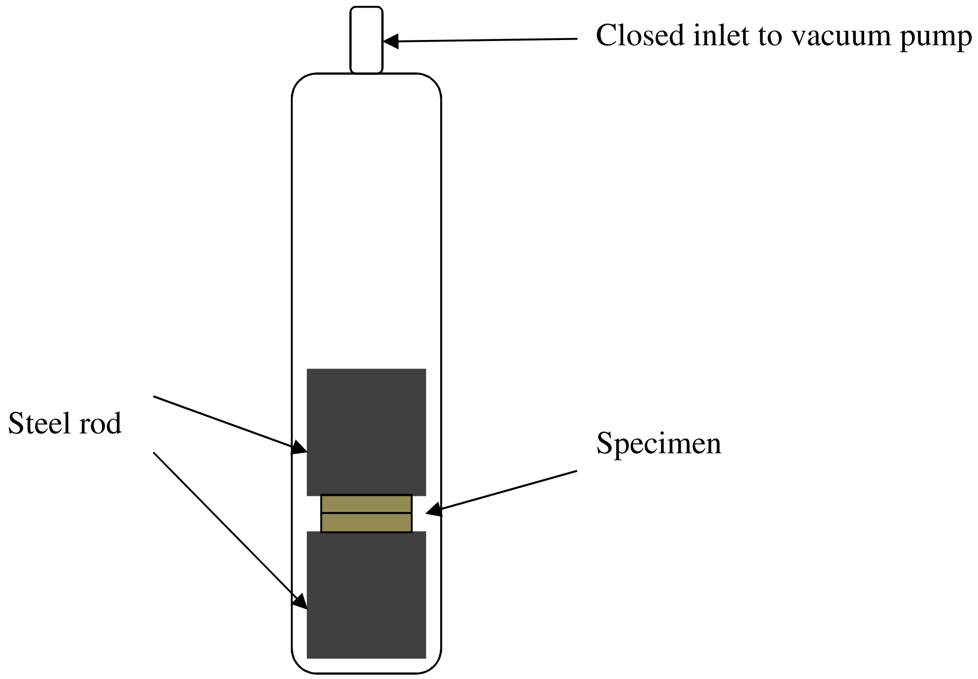

Figure 3.2 Schematic of vacuum ampule used for high vacuum experiments.

The Ag layer in the oxidized heterostructures did not melt for all thermal processing below the bulk melting temperature of Ag. Thickness of the Ag foil after treatment below the bulk melting temperature was the same as before thermal treatment, contrary to heating above the bulk melting temperature of Ag which results in a 20% decrease in thickness. Also, there was no visible sign of Si inclusions in the Ag. However, the thermal treatment at 900° C resulted in formation of periodic Ag nanostructures embedded in the interface along the Si layer.

3.1.2 Ag Nanostructure Structural Characterization

After thermal processing, all specimens were mounted and cross sectioned and then imaged via SEM, as shown in Figure 3.3. Ag triangular growth features were observed at the (100) Si interface for one hour heat treatment at 900° C (Figure 3.3b). The size of the structures was approximately 300 nm wide and tall on average. The short heat treatment (ramp only up to

900° C) produced structures 250 nm wide at the base and tall (Figure 3.3a). The longest heat treatment (ramp plus 10 hour at 900° C) created structures 1 μm wide and tall on average for (100) Si (Figure 3.3c). Figure 3.3d displays a closer view of the foil specimen heated for 10 hours. One can recognize three layers with characteristic features: layer A containing the pyramid structures, layer B consisting of an evenly distributed glassy layer of Ag and Si particles in the vicinity of the oxide nanolayer, and layer C comprised of an uneven interface of Si and the Ag foil.

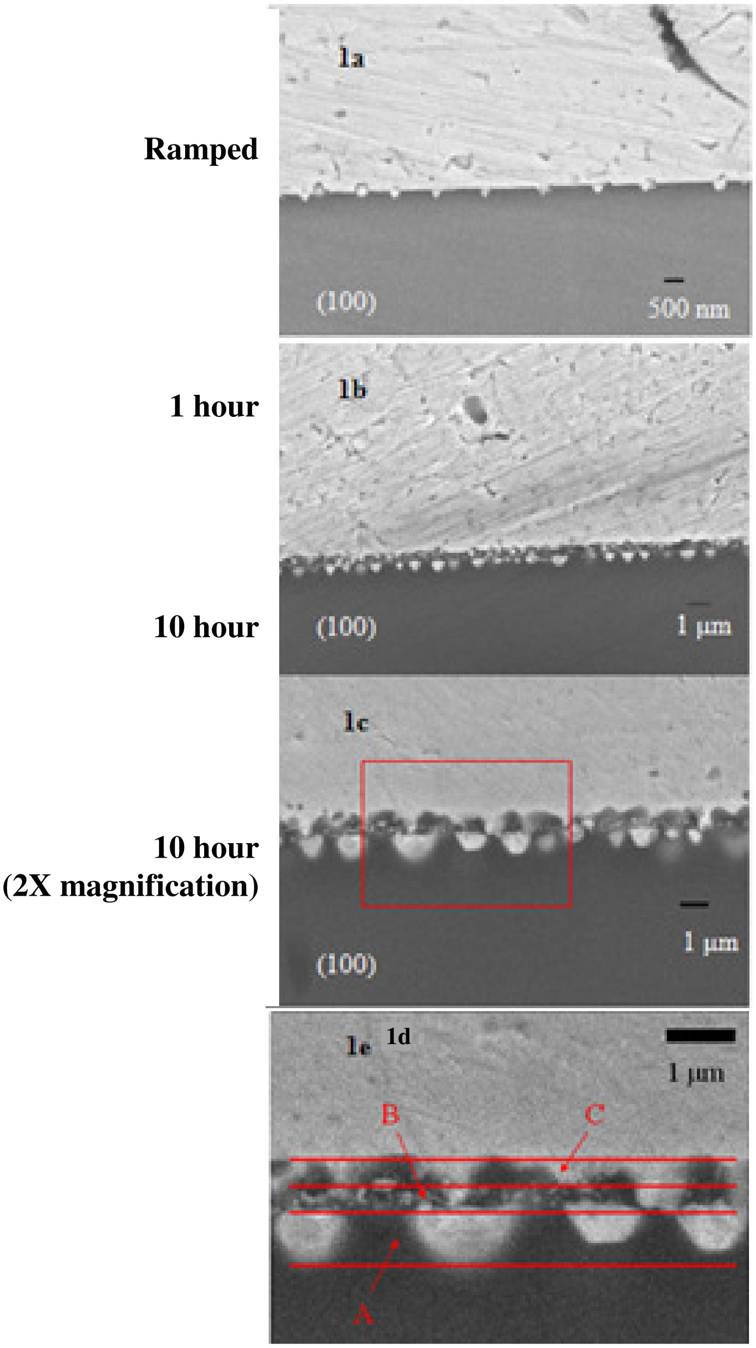

Figure 3.3 Cross section SEM micrographs of Ag foil sample prepared using (100) Si substrates after: ramped only heat treatment with (100) Si, 1 hour heat treatment with (100) Si, 10 hour heat treatment with (100) Si, and magnified cross section SEM image from 1c of foil specimen heated for 10 hrs. displaying three distinct interface regions.

Structures approaching 2 μm wide and 400 nm thick for the largest observed structure in the (111) substrate (Figure 3.4), establishing the dependence of nanostructure morphology on Si crystal orientation.

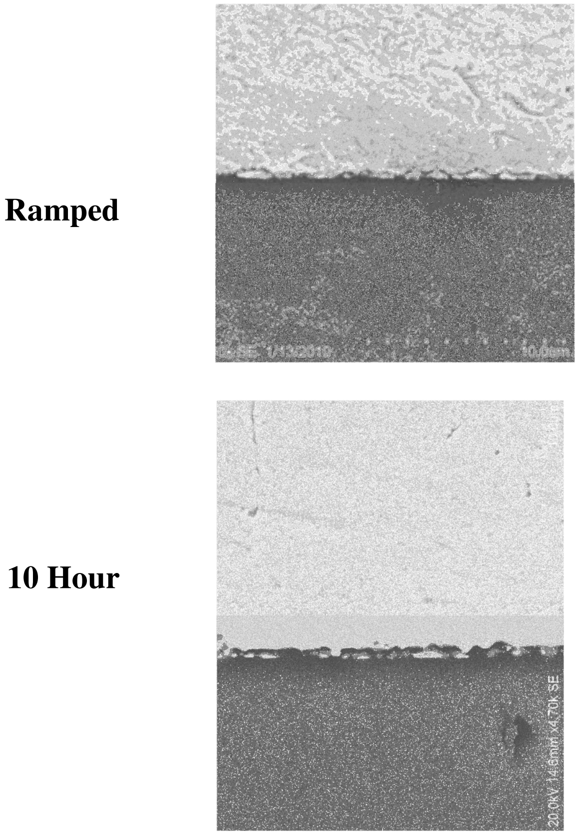

Figure 3.4 Cross section SEM micrographs of Ag foil sample prepared using (111) Si substrates after: ramped heat treatment, 10 hour heat treatment, with the same magnification.

Specimens of (100) and (111) orientation were processed at 1000° Celsius in air and Ag melting was observed. Applied pressure forced a substantial volume of Ag to flow out of the sample, reducing the effective thickness to 20% of the initial foil thickness. After solidifying, traces of Si were found within the Ag region that resembled a eutectic pattern and nanostructures were observed along the bulk Si and melt interface, as displayed in Figure 3.5. Similar to growth structures occurring during the 900° Celsius specimen treatment, a clear sawtooth pattern of Ag features is present with an intermediate layer underneath the features.

After solidifying, traces of Si were found within the Ag region that resembled a eutectic pattern (Figure 3.5) and nanostructures were observed along the bulk Si and melt interface. These structures possibly formed during the ramp stage before melting of the Ag foil. In both the (100) and (111) cases, the liquid front grows into the Si wafer, creating bulges. However, the initial interface between Si and Ag remains visible as a chain of small Si particles. This residual interface was generated from the intermediate layer in the heterostructures (layer B in Fig. 1d) and is formed by oxide nanoparticles which serve as seeds for precipitation of Si.

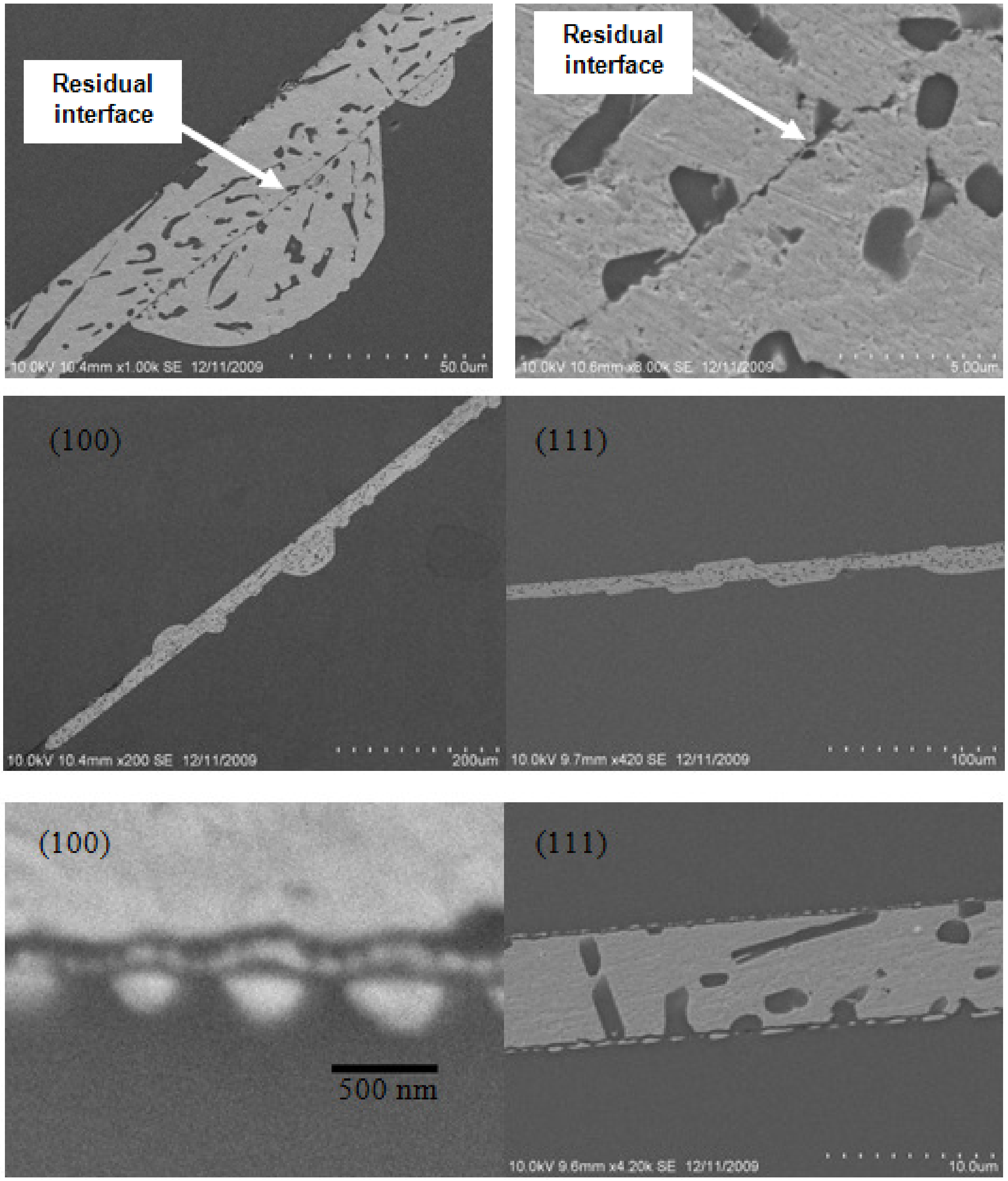

Figure 3.5 Far (top left) and near (top right) field SEM images of melted Ag (100) specimen displaying residual interface between initial Ag foil interface and melt front. Far field SEM images of 1000°C melted (100) and (111) specimens (middle). Near field SEM images of interfaces of 1000°C melted (100) and (111) specimens (bottom).

The specimens stripped of native oxide were processed in an ampule under vacuum pressure at 900° Celsius and yielded a melted region with approximately 12% Si (Figure 3.6), complying with eutectic composition of pure Ag-Si. No ordered structures were observed along the melt and Si interface. It is also notable that no residual interface is present between the initial foil and melt front, as referred to in Figure 3.5.

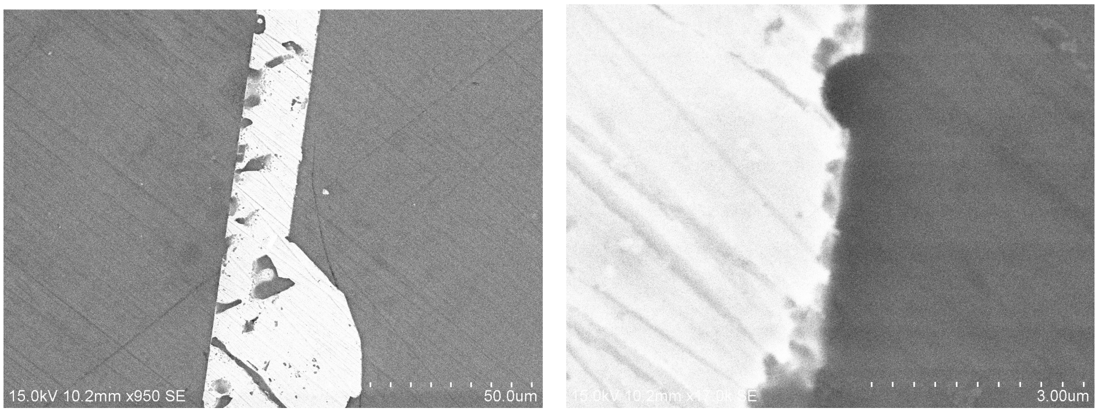

Figure 3.6 Far field (left) and close field (right) SEM micrograph of Ag-Si diffusion couple processed in vacuum ampule.

Electron backscatter diffraction (EBSD) was used to characterize the crystal structure of Ag nanopyramids and surrounding Si crystal. EBSD is a SEM based characterization technique used to quantify crystal structure on a millimeter to nanometer scale. This is accomplished by capturing backscattered electrons from the specimen surface and imaging Kikuchi bands that form via interaction of electrons from each of the lattice diffracting planes. The captured pattern can then be indexed to known patterns in a crystallographic database in order to verify the crystal structure of the grain in the imaged specimen. This technique is capable of characterizing grains as small as 50nm in size. The specimen must be rotated 70° relative to normal incidence of the electron beam which significantly distorts the microscope image and makes accurately imaging and identify nano-scale phases dubious due to change in imaging aspect ratio. This analysis, shown in Figure 3.7, confirms the epitaxial relation between the single crystal Ag nanostructure and the immediate surrounding Si.

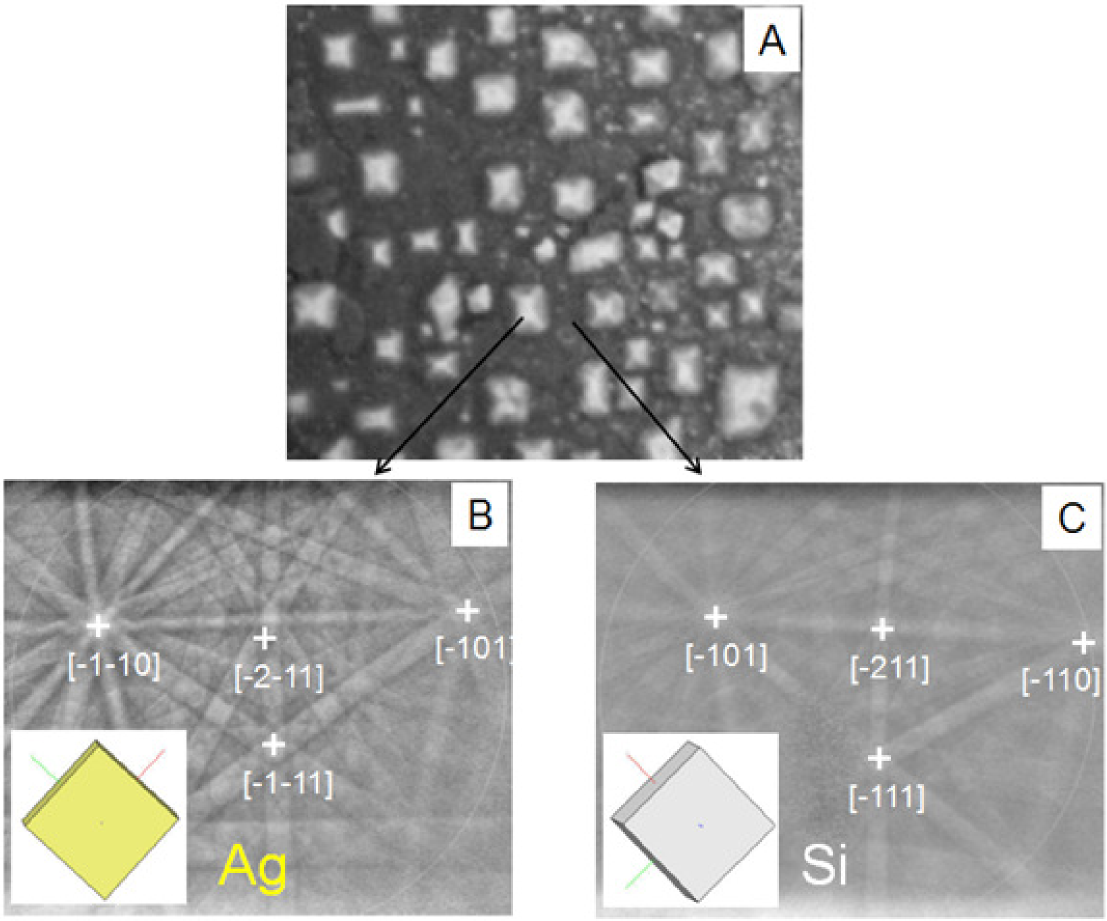

Figure 3.7 EBSD patterns of the Ag islands (B) and the underlying Si substrate (C). Insets with simulated orientations of unit cells indicate epitaxial relationship between Ag islands and Si substrate.

The geometries of Ag nanostructures in both (100) and (111) specimens is consistent with regard to Si crystal structure. In other words, the planar view of the interface of the (111) specimen (Figure 3.8, planar view prepared by peeling apart specimen) show Ag crystals formed in the shape of equilateral triangles and this morphology and orientation corresponds to the (111) faces of the pyramid structures in Figure 3.7. This proves that epitaxial formation is the same in both cases, and the change in morphology is dependent on which plane the structures are viewed (ie. transverse to the (100) or (111) plane).

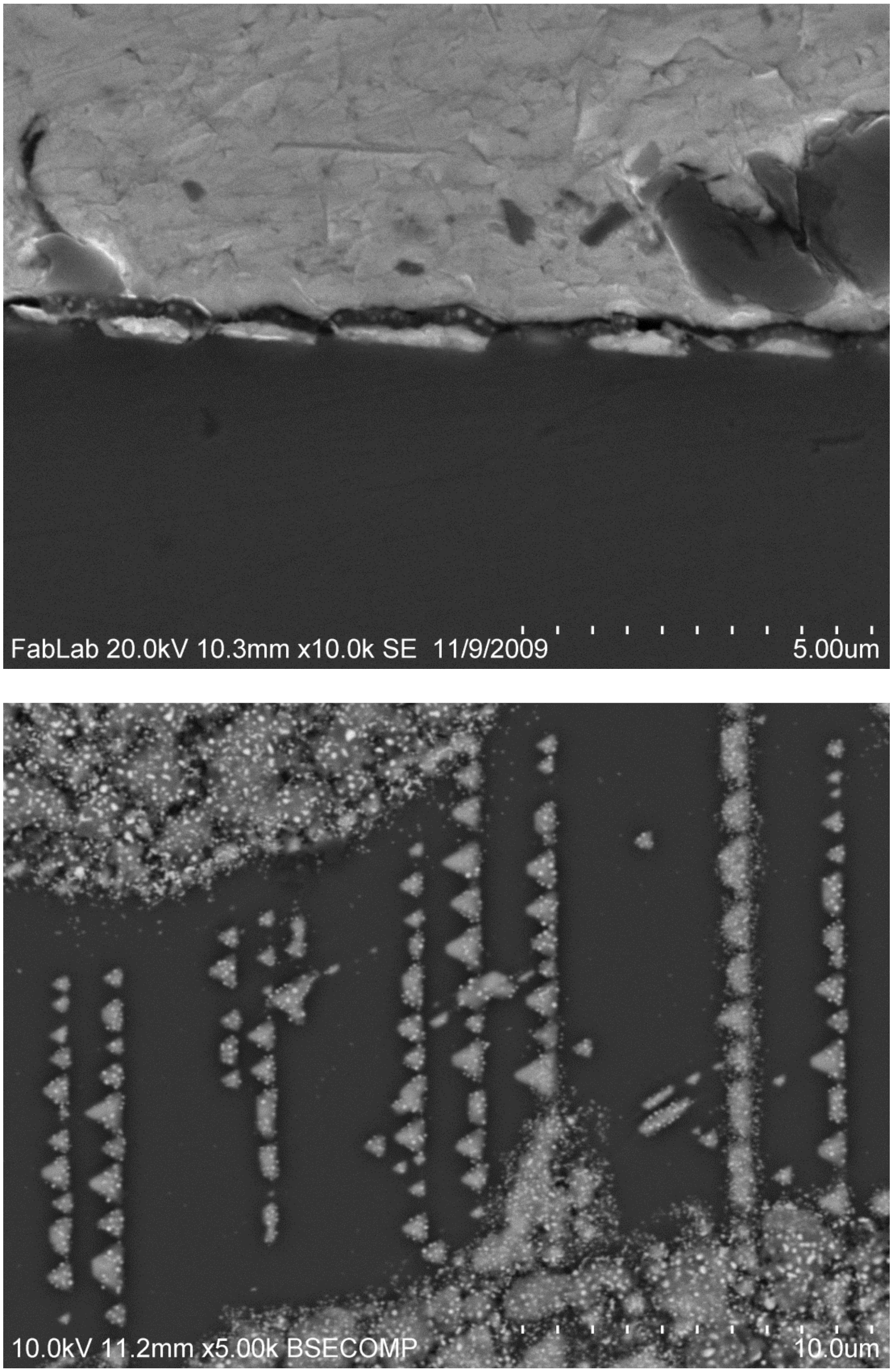

Figure 3.8 High mag cross section of annealed (111) Si specimen (top) and top surface of peeled-apart specimen revealing planar surface geometry of nanostructures.

The height and size of Ag nanostructures in Figure 3.8 was characterized via scanning probe microscopy. The micrograph of the scan is displayed in Figure 3.9. The features are on the order of 300 nm high. Note that the triangular artifact effect observed in the micrograph is due to the tip shape and bluntness of the scanning probe (berkovich tip in Hysitron Nanoindenter).

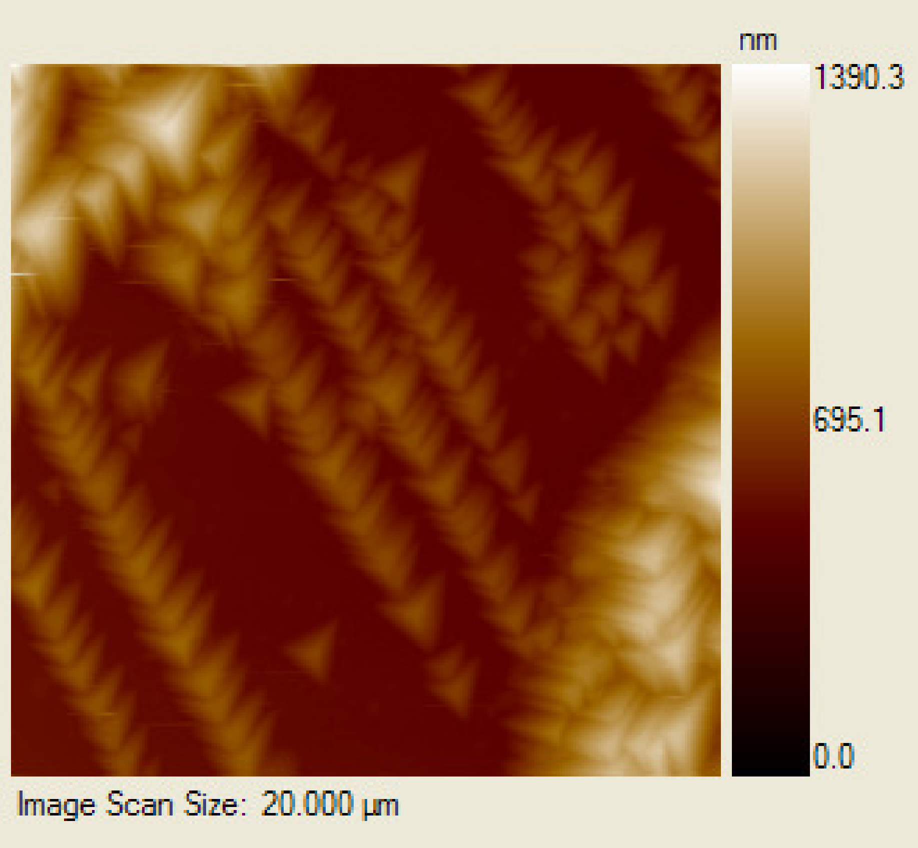

Figure 3.9 SPM micrograph of Ag nanostructres on surface of peeled (111) Si specimen.

A (100) native oxide specimen was processed at 800° C to observe possible nanostructure formation while heated below the eutectic temperature of the system. A heating method similar to the process described earlier (ramp up to desired temperature in 3 hours, hold steady for 1 hour, and allow the oven to cool passively in ambient temperature) was used. SEM micrographs reveal small features along the interface that resemble those observed when heated above the eutectic temperature. These structures are smaller than ones observed in previous cases with dimensions on the order of 100-200 nm. A (100) specimen was also heated for 10 hours with the same ramp method (ramp in 3 hours and hold steady for 10 hours) and was quenched in water immediately after the 10 hour period (Figure 3.10). Ag pyramids similar to the other (100) specimens are present with a size of up to 300 nm in terms of height and width. When comparing the intermediate layers of quenched and unquenched specimens, the quenched specimen does not exhibit a third layer comparable to layer C of the unquenched specimen in Figure 3.3e. This observation suggests a liquid layer above the pyramid nanostructures is present and slow crystallization in the unquenched case may be responsible for formation of layer C. Furthermore, observations of like Ag pyramid structures in quenched and unquenched cases may imply that the formation of this layer is driven by an etching process during heating rather than melt solidification [88].

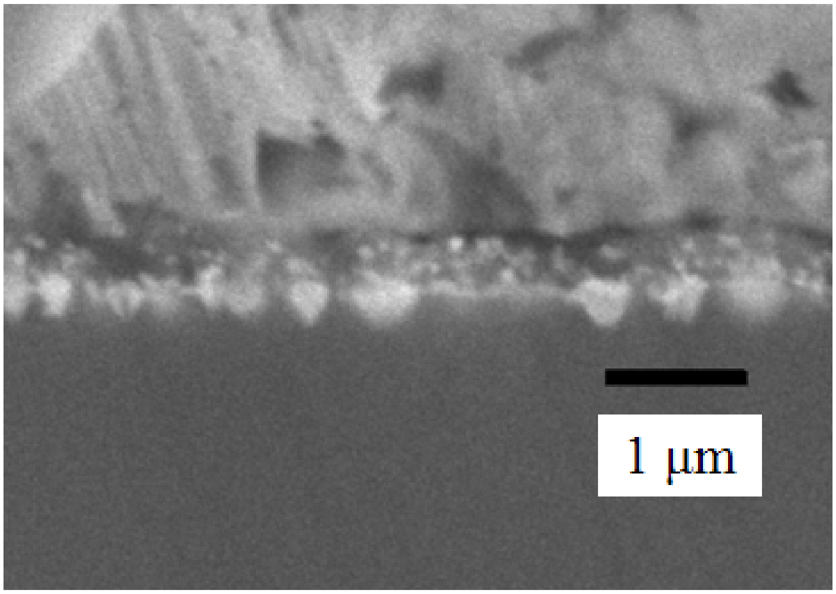

Figure 3.10 SEM micrograph of Ag-Si interface displaying triangular Ag nanostructures (light regions) with thick intermediate layer after 10 hour 800° Celsius heat treatment with quenching.
\

3.1.3 Discussion

The presented results clearly demonstrate that annealing in an oxygen-rich environment (air) above the eutectic temperature but below bulk melting retards diffusion between Ag and Si. Evidently, the native oxide layer increases thickness in combination with possible formation of Ag oxide as the furnace is heating, creates an effective diffusion barrier. This layer behaves as a semi-permeable membrane, permitting Ag to diffuse into Si, but not Si into Ag. During annealing at the eutectic temperature or higher, Ag penetrates the oxide layer and forms a layer of liquid composed of Ag and Si, close to the eutectic composition. Then, during cooling this liquid crystallizes to form a solid mixture of Si and Ag. Si proceeds to solidify epitaxially on the single crystalline Si surface. Due to preferential orientation of interfaces between Ag and Si, the inclusions of Ag in Si take on the shape of pyramids with (111) faces. The thickness of the liquid layer, and the size of the Ag pyramids, is determined by the rate in which Ag penetrates the oxide barrier. As shown in experiments, this oxide layer becomes less effective as a semi-permeable membrane at the melting temperature of Ag.

The size and morphology of the structures was found to depend on the duration of thermal treatment, as well as the crystallographic orientation of the Si wafer. Longer thermal treatment was found to increase the feature density as well as size. Heat treatment below the eutectic temperature created a sparse array of features that were much smaller than when treated at higher temperatures.

This study produced several observations that provide insight into nanostructure formation along a heterostructure composed of Ag and oxidized Si:

1. A nanostructured interface consisting of Ag crystals embedded in Si wafer can be produced without the use of doped Ag paste, but instead with a Ag-Si couple annealed in air.
2. Specific morphology of interfacial nanostructures observed in prior studies [1]-[4] was found to be dependent on Si orientation.
3. Annealing specimens in air prevents eutectic melting of the Ag-Si couple at temperatures up to the melting point of Ag.
4. The periodicity and scale of nanostructures are controlled through processing temperature and time.
5. Native oxide does not act as an effective diffusion barrier when annealed in the absence of air above the eutectic temperature.
6. Nanostructure formation can be inhibited by annealing in vacuum.

4 Epitaxial Palladium Film Fabrication and Hydrogenation

Epitaxial Pd thin films of 50 and 100 nm thickness were deposited and characterized via AFM and XRD before and after hydrogenation. Hydrogenation produced noticeable surface effect, but as noted in the literature in similar studies of Pd foil [50], the presence of coherent structure after H loading was variable. High temperature hydrogenation produced visible ordered, plate-like structures, but the presence of H could not be confirmed via XRD characterization.

4.1 Film fabrication and characterization

Pd films were deposited on c-plane sapphire substrate with a V buffer layer by electron-beam deposition (schematics of setup shown in Figure 4.1 and Figure 4.2). E-beam deposition is a type of physical vapor deposition where a source target is bombarded by a steady beam of electrons produced by a heated Tungsten filament. This beam melts the target and allows evaporation and condensation over the inner surface of the chamber. The substrate is mounted directly over the target on the top side of the chamber to allow clear line-of-sight and uniform deposition thickness. The deposition performed in a vacuum chamber which can preferably maintain a vacuum of up to ~10^{-9} torr. Deposition speed can be well controlled by 0.01 nm/s up to over 10 nm/s. E-beam deposition is convenient when depositing multi-layer structures since the vacuum does not need to be broken in order to alternate the target.

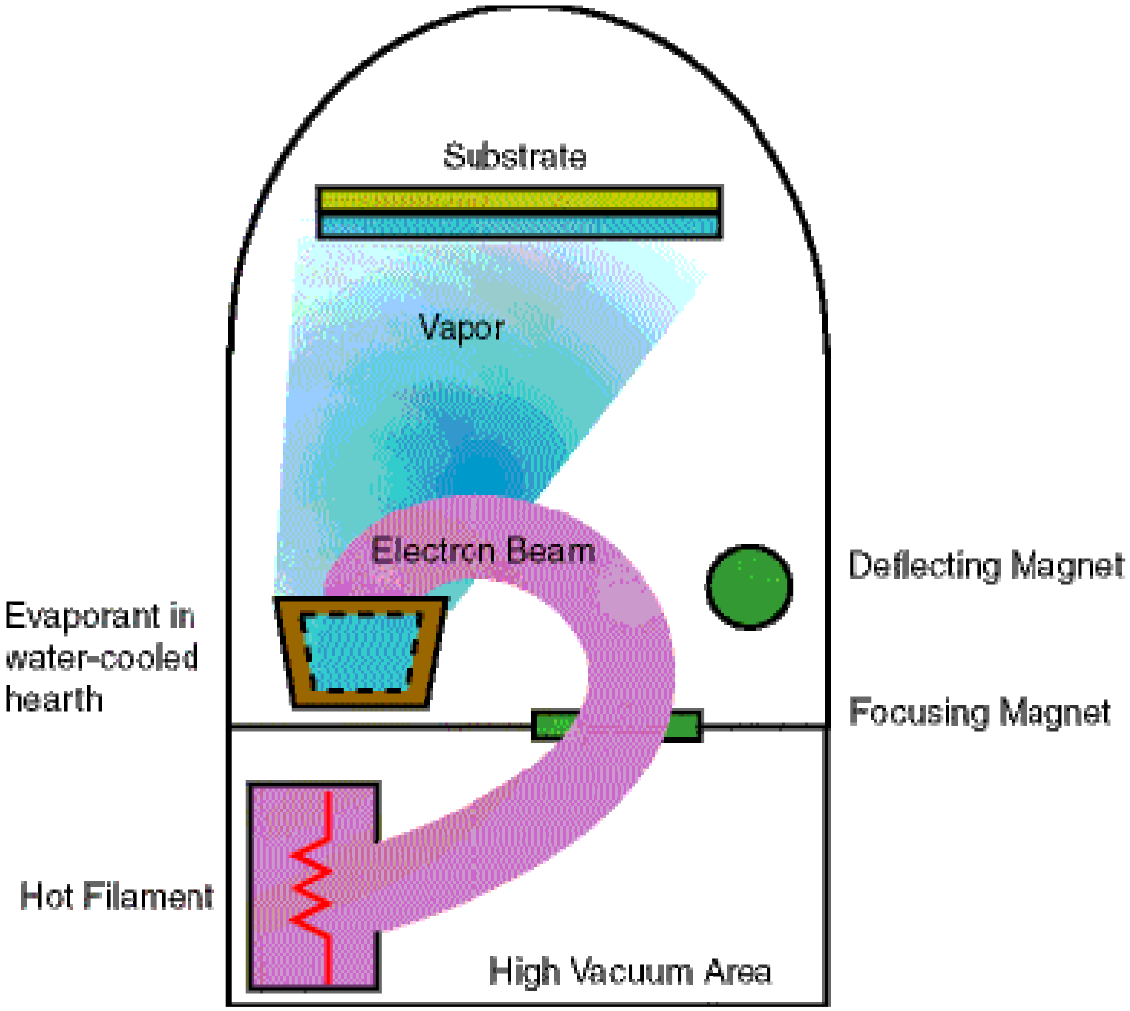

Figure 4.1 Schematic of e-beam deposition process [89].

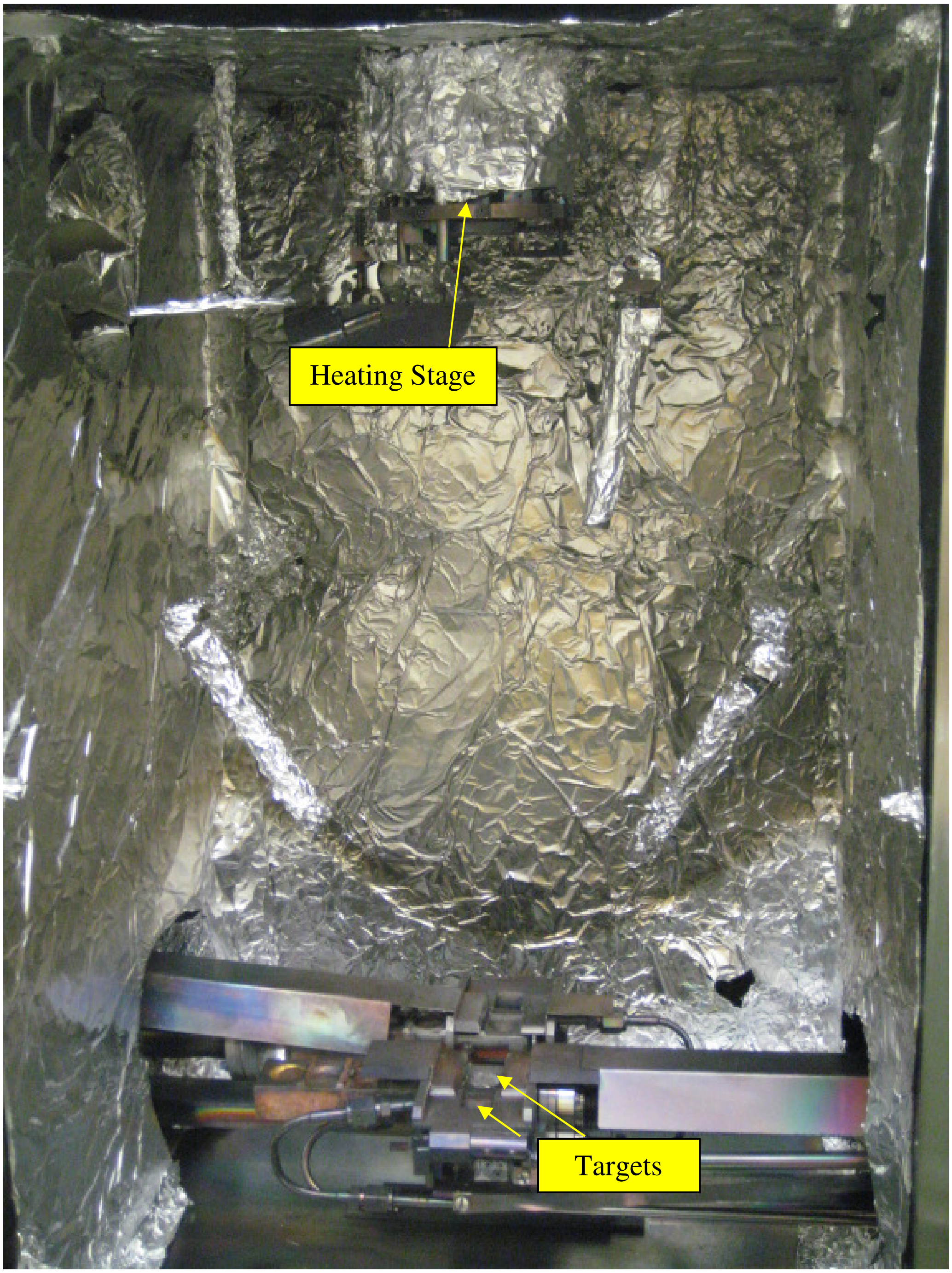

Figure 4.2 Electron beam deposition chamber used for Pd thin film deposition.

Pd granules 99.994% pure were used. Vacuum pressure in the e-beam chamber reached ~$2*10^{-8}$ Torr before deposition and rose upwards of ~$5*10^{-7}$ Torr during deposition. The deposition stage was heating during fabrication, as this was shown to improve smoothness and overall quality of the film [57]. Heating of 100°C produced roughness of ~3nm while heating at 120°C produced roughness around 1-2nm on average. The films were allowed to cool to room temperature in the deposition chamber under vacuum to prevent oxidation of the Pd surface. All Pd films were stored in a vacuum desiccator before hydrogenation to minimize organic contamination on the film surface.

AFM analysis of the as-deposited films displayed grains approximately 50nm wide with 1-3nm average roughness. Additionally, a pole map was created by measuring peak intensity at 2θ for (220) at a χ angle of 54.79°, which represents the angle between the (220) and (111) orientations. The ψ axis was then rotated a full 360° in increments of 5°. The pattern shows 6 distinct points which correspond to the 2 possible epitaxial stacking patterns for Pd [57]. Additionally, x-ray diffraction confirmed single phase growth, as only (111) Pd and sapphire peaks are visible (Figure 4.3). Depositing pure Pd on sapphire results in a multi-oriented film [57]. To create a highly textured, epitaxial film, a 1 nm V buffer layer was deposited between the Pd and sapphire [57]. This effect is attributed to a Nishiyama-Wassermann type BCC to FCC metal growth transformation and results in epitaxial (111) in–plane film growth.

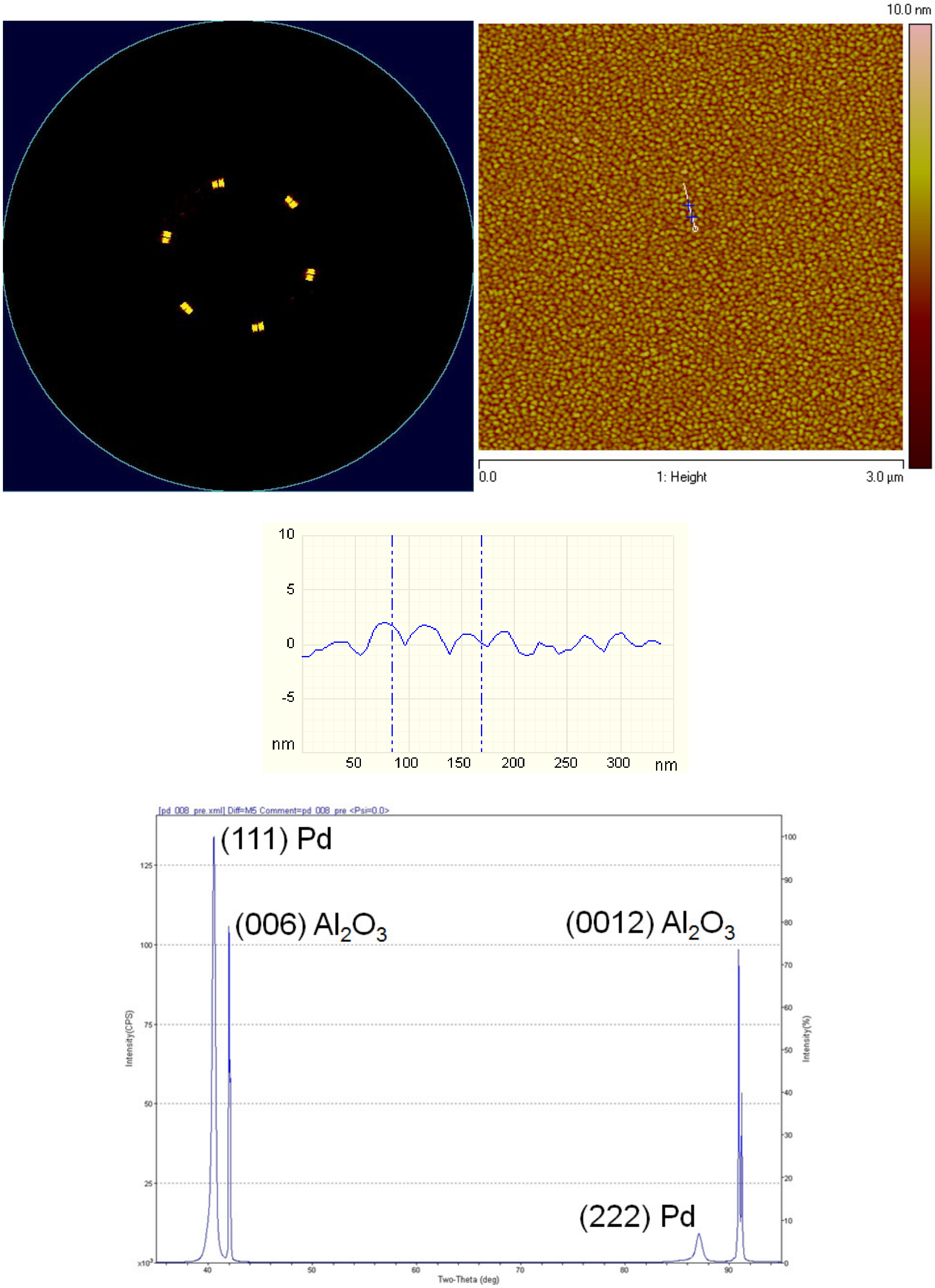

Figure 4.3 Pole map (top left) confirming epitaxial Pd film growth, AFM topography with scan line (top right) of Pd film, scan line detail of surface morphology (middle), and x-ray diffraction data from epitaxial Pd film (bottom).

The quality of epitaxy between the film and substrate interface may greatly affect the internal stress of the film, as well as the possibility of coherent polydomain formation [6]. When considering the constituent layers of the multi-layer film structure, it is necessary to calculate equivalent lattice parameters for the Pd and V layers, as the (111) plane of these layers will lay parallel to the basal plane of the Al_2O_3 substrate. In this case, the equivalent epitaxial lattice parameters will be $\frac{\sqrt{2}}{\sqrt{3}}a$. Further calculation, using parameters from Table 4.1, provides epitaxial strain of ~0.94 for the V layer and ~0.51 for the Pd layer with respect to the initial unstressed Al_2O_3 parameter. Clearly, these values are excessively high for relatively soft metals and it can be inferred that dislocations form along one or both interfaces in order to relieve stress.

Layer	Structure	Lattice Parameter (nm)
Al_2O_3	HCP	a=.4785 b=1.299
V	BCC	.3020
Pd	FCC	.3889
PdH_x, x<0.017	FCC	.3985
PdH_x, x>0.580	FCC	.4025

Table 4.1 Structure properties of substrate, V layer, Pd, and α and β PdH phases.

All hydrogenation experiments were performed in a Sieverts type apparatus (Figure 4.4) located at the National Institute of Standards and Technology (Gaithersburg, MD). The apparatus was connected to a loading chamber via thin steel tubing and the chamber was place-able into a small tube furnace for elevated temperature experiments. This setup enables testing at pressure up to 100 bar and temperatures up to 500°C. The minimum sensitive for pressure measurements is 0.001psi. An 18" long Cu tube with one closed end was used as the loading chamber. This was used to isolate the connecting hardware to the steel tubing, since it could not maintain a proper seal at furnace temperature without leaking.

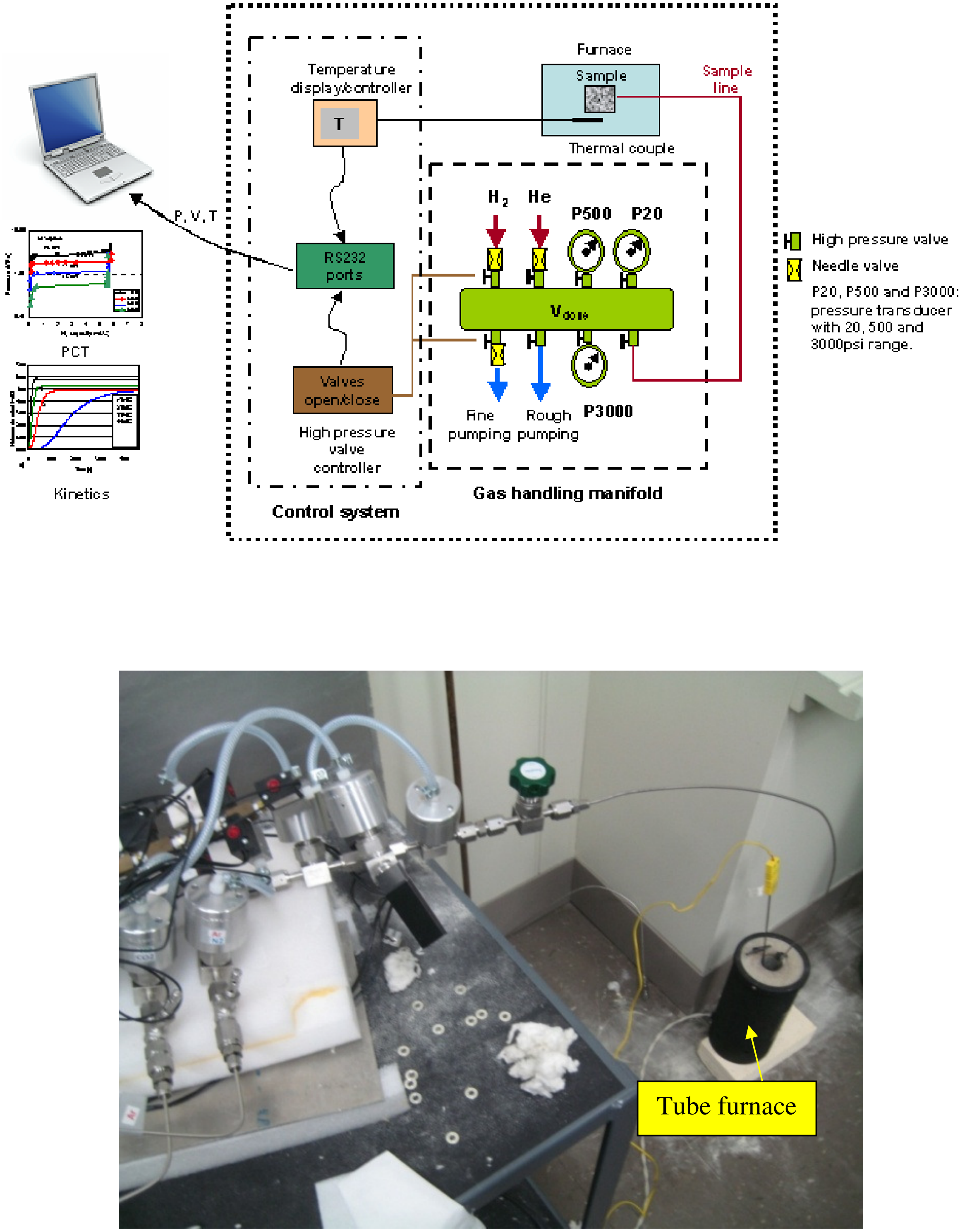

Figure 4.4 Schematic of Sieverts apparatus used to hydrogenate Pd films [90] (top) and apparatus connected to small chamber in tube furnace (bottom).

Specimen #	Film thickness (nm)	Process T(K)	H2 Pressure (bar)	Quench	XRD
Pd002	50	650	0.50	none	β peak
Pd004	50	650	0.85	none	β peak
Pd005	50	650	1.00	none	none
Pd006	50	195	31.00	none	none
Pd007	50	650	26.00	none	none
Pd008	50	650	18.00	water	none
Pd008_03	50	650	25.00	none	none
Pd010_01	100	650	0.01	none	none
Pd010_02	100	300	0.55	none	none
Pd010_03	100	300	28.00	none	β peak
Pd010_05	100	650	28.00	liquid N2	none
Pd010_06	100	650	27.00	liquid N2	none
Pd010_07	100	650	27.00	ice	none
Pd010_08	100	650	0.01	ice	none
Pd011_01	100	300	8.00	liquid N2	none

Table 4.2 Summary of epitaxial Pd film hydrogenation experiments.

4.2 Hydrogenation of 50nm Thick Epitaxial Pd Films

Two sequences were used when hydrogenating the epitaxial Pd films: load low pressure at room temperature and allow to cross the two-phase boundary, and load pressure at high temperature and impose single phase composition according to the conventional phase diagram until cooling (Figure 4.5). The high temperature case (650K) was hydrogenated at a pressure of 18 bar to keep phase distribution in the single phase α region (in accordance with bulk isotherm data in Figure 2.9). For both specimens after loading, all gas was vacuumed away (and allowed to cool in the chamber under vacuum in room temperature for the heated specimen). After removal, specimens were characterized via AFM and XRD approximately 10 minutes after, with full characterization taking approximately another 30 minutes.

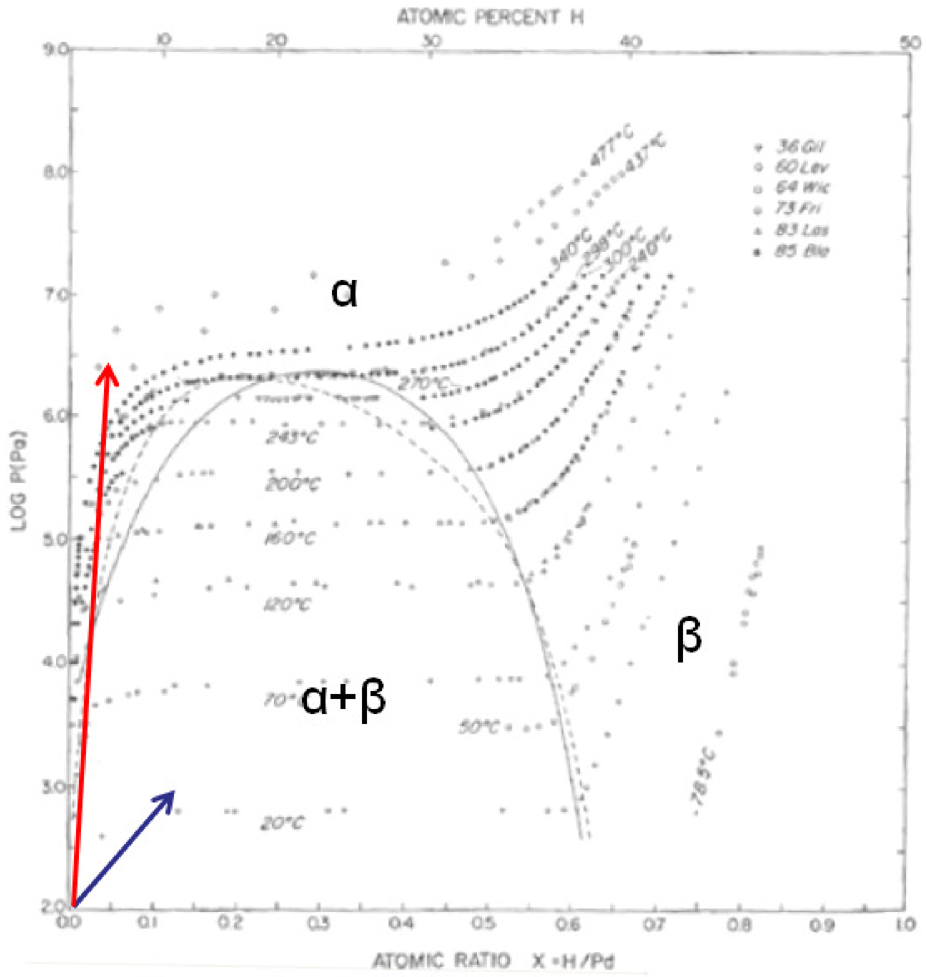

Figure 4.5 Loading schemes used for high temperature (red) and low temperature (blue) hydrogenation experiment.

4.2.1 Room Temperature Hydrogenation

Films were hydrogenated at room temperature and high hydrogen pressure (18 bar) to fully transform the film to β phase in order to (a) confirm the presence of hydride phase via ambient environment XRD analysis and (b) to ascertain approximately how long under ambient conditions this phase exists before full decomposition. After removing from the hydrogenation chamber, x-ray analysis was performed completed at ~30 minutes after removal. These results (shown in Figure 4.6) show almost full conversion to β phase hydride. This specimen was then kept in ambient conditions for ~12 hours and rescanned to analyze evolution of hydride phases. This result (Figure 4.6) shows full conversion back to (111) Pd. This data shows that (1) analyzing specimens for hydrogen content in ambient conditions is plausible in the case of room temperature hydrogenation as long as analysis is performed relatively quickly after removal and (2) the hydride phases fully decompose when stored in ambient conditions for as little as 12 hours.

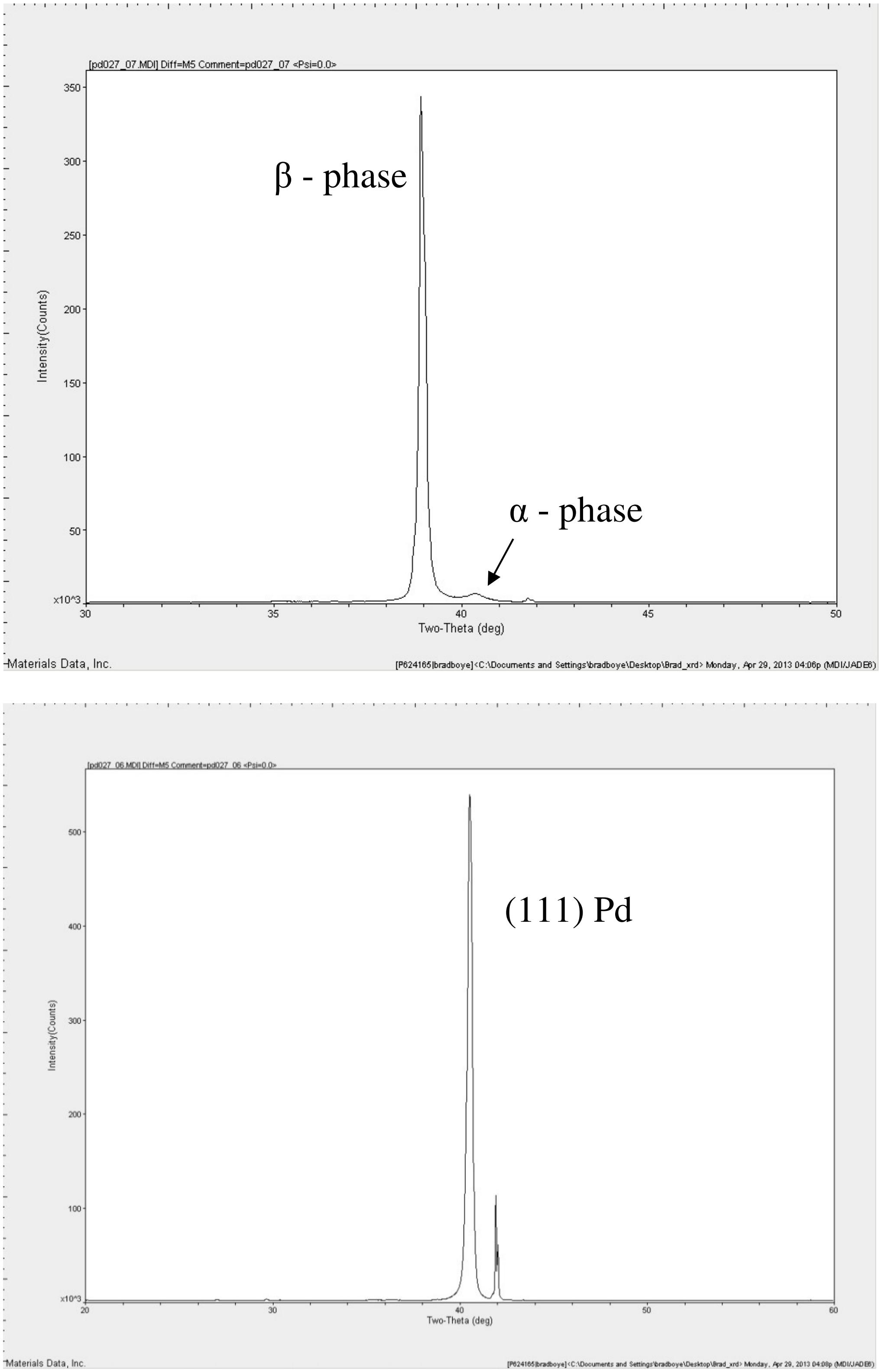

Figure 4.6 XRD spectrum of 50 nm Pd film (top) directly after room temperature and high pressure hydrogenation and (bottom) conversion back to (111) Pd after 12 hours in ambient conditions.

50 nm Pd films were also processed at room temperature and 300 mbar of hydrogen pressure. This processing produced unordered coarsening of the film surface and also contained measureable values of beta phase hydride via x-ray diffraction, as shown in Figure 4.7.

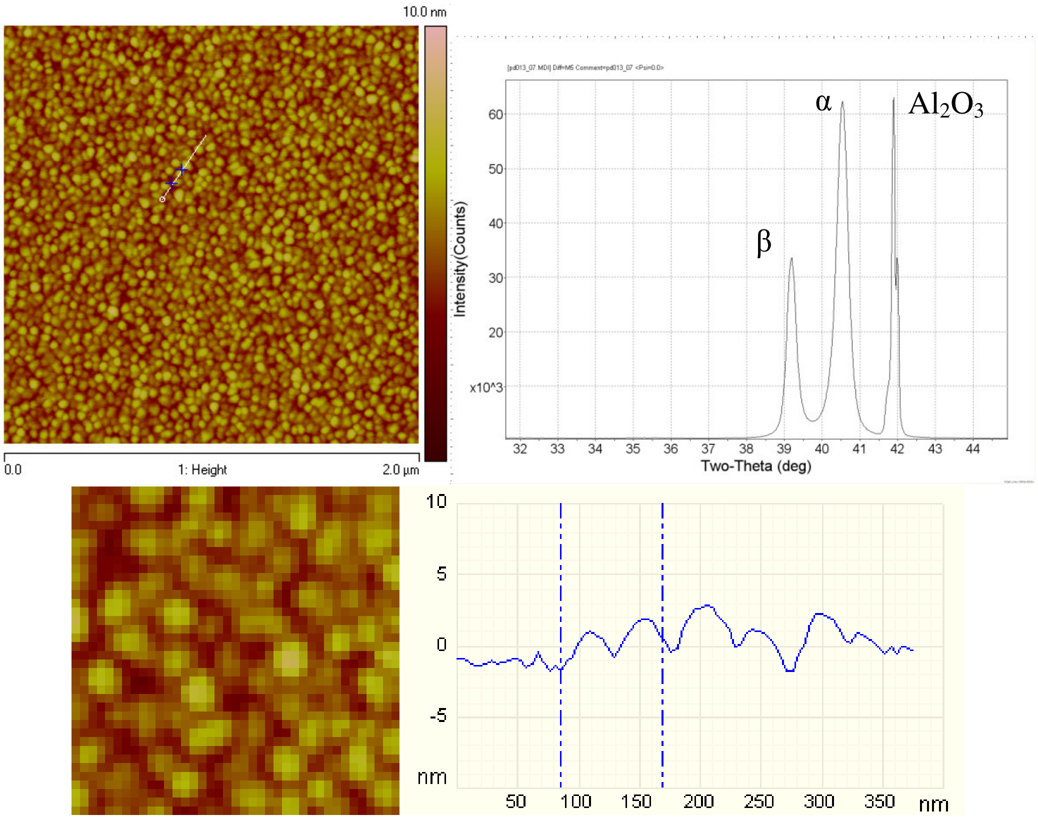

Figure 4.7 AFM micrograph of post hydrogenated film surface (top left) with magnified section (bottom left), x-ray diffraction scan shown α, β, and sapphire peaks (top right), scan profile of surface morphology.

4.2.2 High Temperature Hydrogenation

The high temperature hydrogenation process created ordered surface nanostructure, as shown in Figure 4.8, but failed to leave evidence of hydride presence when analyzed via x-ray diffraction (no peak was present). It is possible that no β phase peak was present due to a low overall concentration of nanostructures on the film surface (Figure 4.12). Furthermore, all hydrogen may have escaped upon removing pressure at high temperature due to high mobility of

H atoms out of the film at 650K and the observed ordered structures were remnants of defect formation due to partial coherency or twinning.

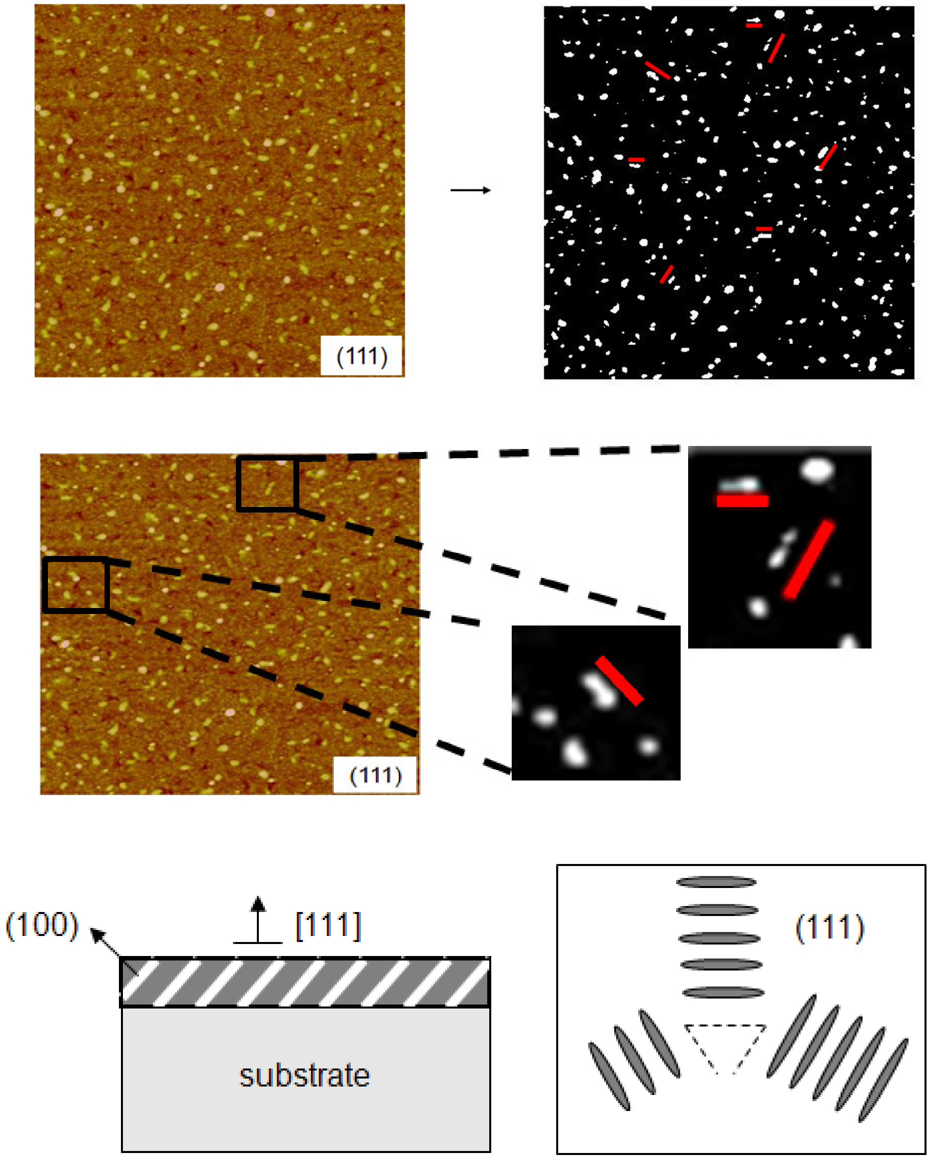

Figure 4.8 Surface topography of hydrogenated 50nm Pd film (top left), threshold image emphasizing nanostructure formation (top right), magnified threshold image (middle), and predicted orientation of coherent phase formation in (111) epitaxial film.

It can be concluded that high quality epitaxial films do not produce classical ordered plates, such as in [50], when hydrogenated to relatively low concentration levels at room temperature.

4.3 Hydrogenation of 100nm Thick Epitaxial Pd Films

100nm epitaxial Pd films were hydrogenated using the same experimental setup shown in Figure 4.4. The films were loaded and allowed to vacuum down to below 1e-4 Torr before the chamber was placed into the tube furnace preheated to 650K. After approximately 30 minutes to allow sufficient preheating, 18 bar of hydrogen pressure was pumped into the chamber. The specimens were held under these conditions for approximately 2 hours to ensure equilibration of hydrogen content within the films. To unload, the sample chamber was kept in the furnace and all gas was vacuumed to below 1e-4 Torr. The chamber was then removed from the tube furnace and allowed to cool to room temperature. Specimens were cooled in vacuum to prevent oxidation of the film surface and also to prevent full hydrogenation of the film, as 18 bar at room temperature will convert all Pd to β phase hydride.

SEM and AFM were utilized to image the film surface morphology in ambient environment after hydrogenation. Both methods revealed ordered, nanoscale plate-like structures with surface orientation virtually the same as that shown in Figure 2.11. Three variants of these structures are visible and are separated by almost exactly 60º of rotation. In other words, one of each three variants could be lined up in such a way as to construct a perfect equilateral triangle. Far and close field SEM micrographs are shown in Figure 4.9. The length scale of the plates appears to be hierarchical, with smallest appearing to be on the order of 10 nm wide and larger ones approaching 200 nm wide.

In an attempt to reproduce the coherent hydride phase formation show in [50], specimens hydrogenated at high temperature were quenched in both ice water and liquid nitrogen. However, quench to these temperatures from 650K severely damaged the film, causing buckling and delamination. The damage to the film was so severe that the surfaces could not be imaged and characterized with AFM. This is most likely due to difference in coefficients of thermal expansion between the substrate and film.

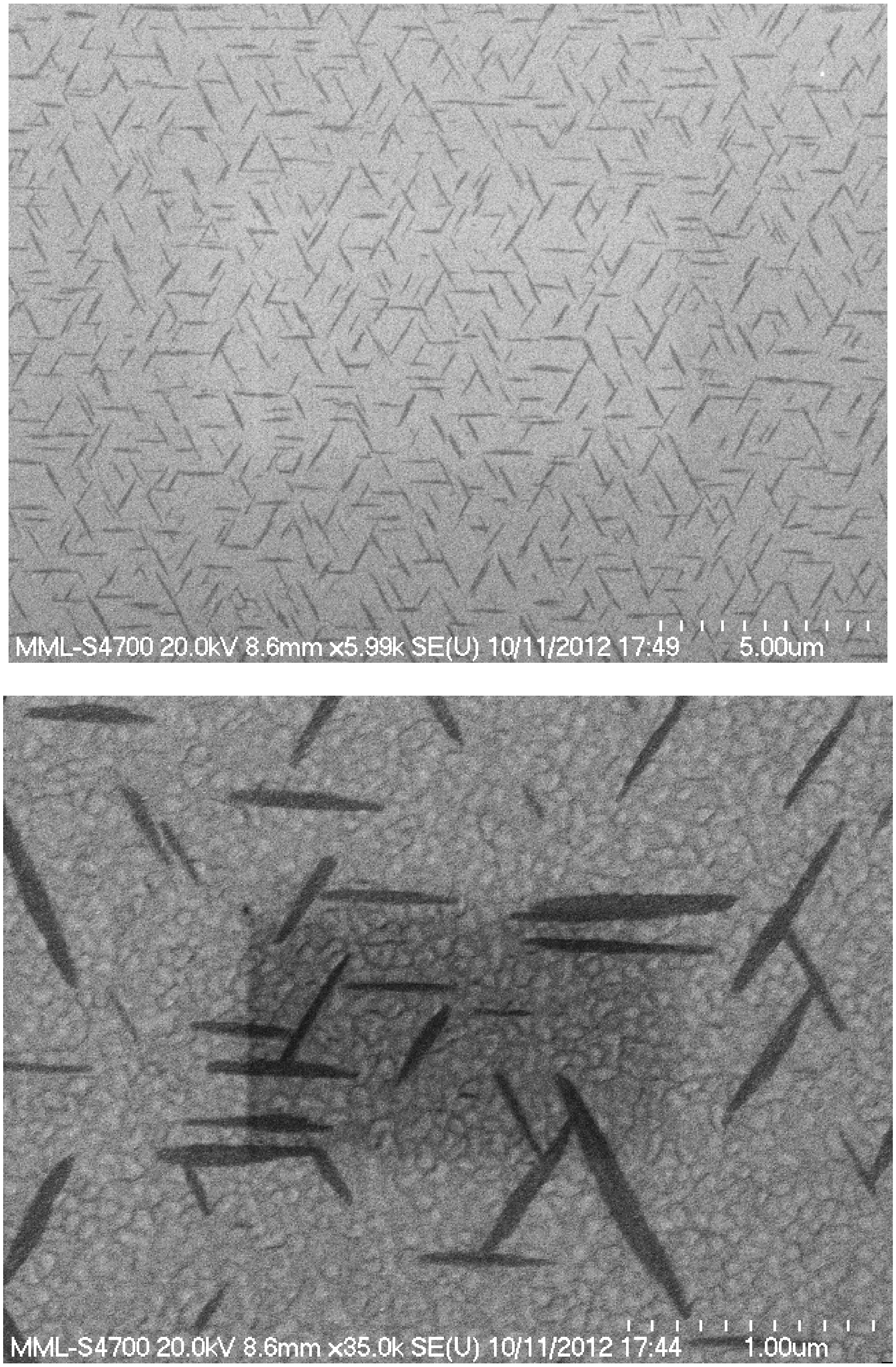

Figure 4.9 Far field (top) and near field (bottom) SEM micrographs of 100nm thick Pd film after hydrogenation at 18 bar and 650K. Dark regions are ordered {100} plates.

XRD analysis (Figure 4.10) shows no evidence of hydride phase existence in the specimen. Only (111) Pd and sapphire peaks are visible on the spectrum. This result could mean (a) all hydrogen was removed from the Pd lattice upon depressurization in the chamber at high temperature (b) the plate morphology seen is in fact β-phase hydride but only in a very small volume relative to the total volume of the film and not measurable with XRD. As previously mentioned, it is also possible that the unique morphology imaged on the film surface is a result of plastic deformation (partial coherency) or twinning [48] and is only an artifact of the regions once existing as β-phase hydride.

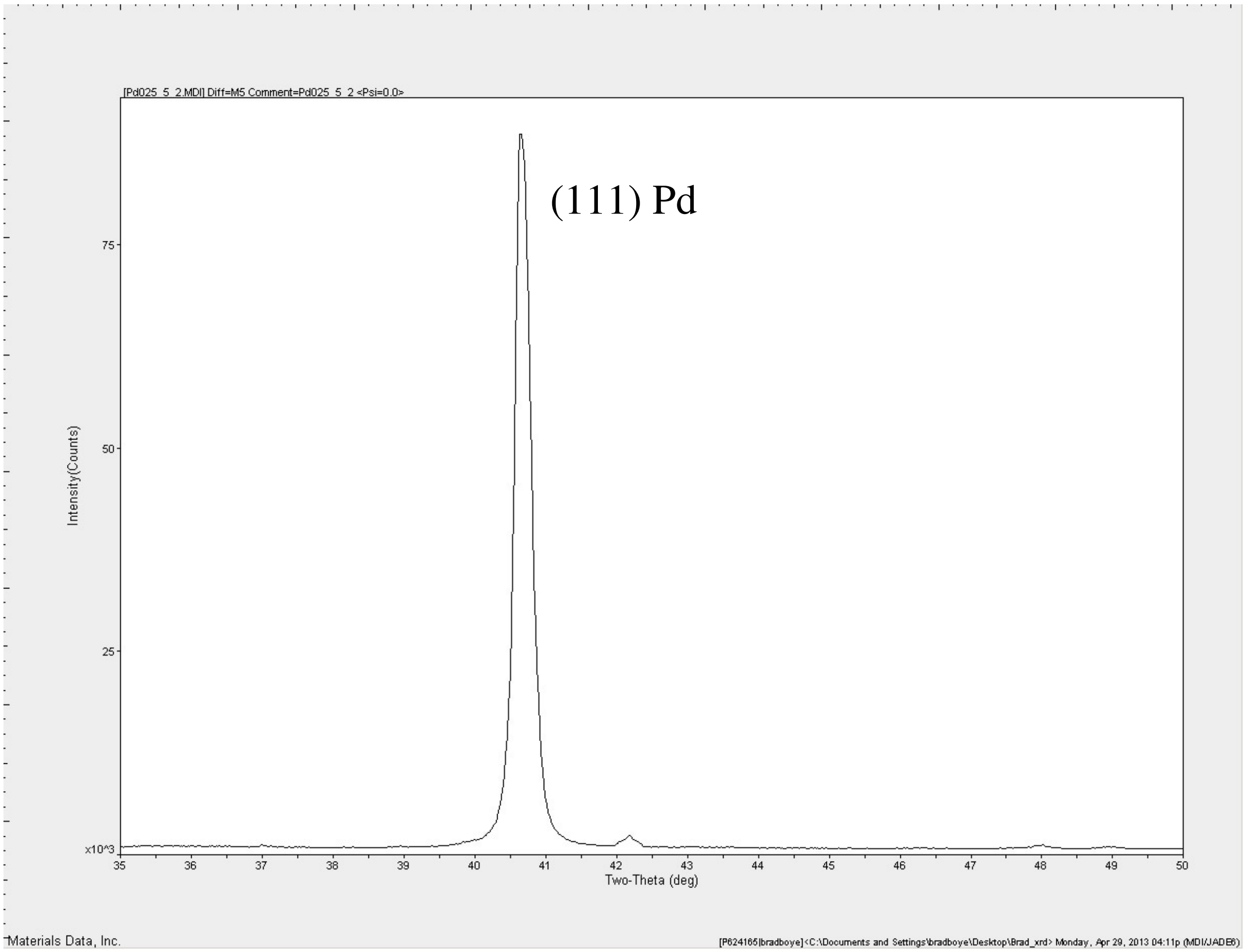

Figure 4.10 XRD spectrum of 100 nm Pd film after high temperature and high pressure hydrogenation.

AFM characterization of the film surface (Figure 4.11) displays the relative height difference between the Pd matrix and the plate structures. The plates are approximately 2-5 nm higher than the matrix. Also, the size, morphology, and orientation of the plates adheres to what is seen in SEM micrographs (Figure 4.9). From this analysis, it is clear that the nanoscale plates form from an expansion in specific crystallographic planes.

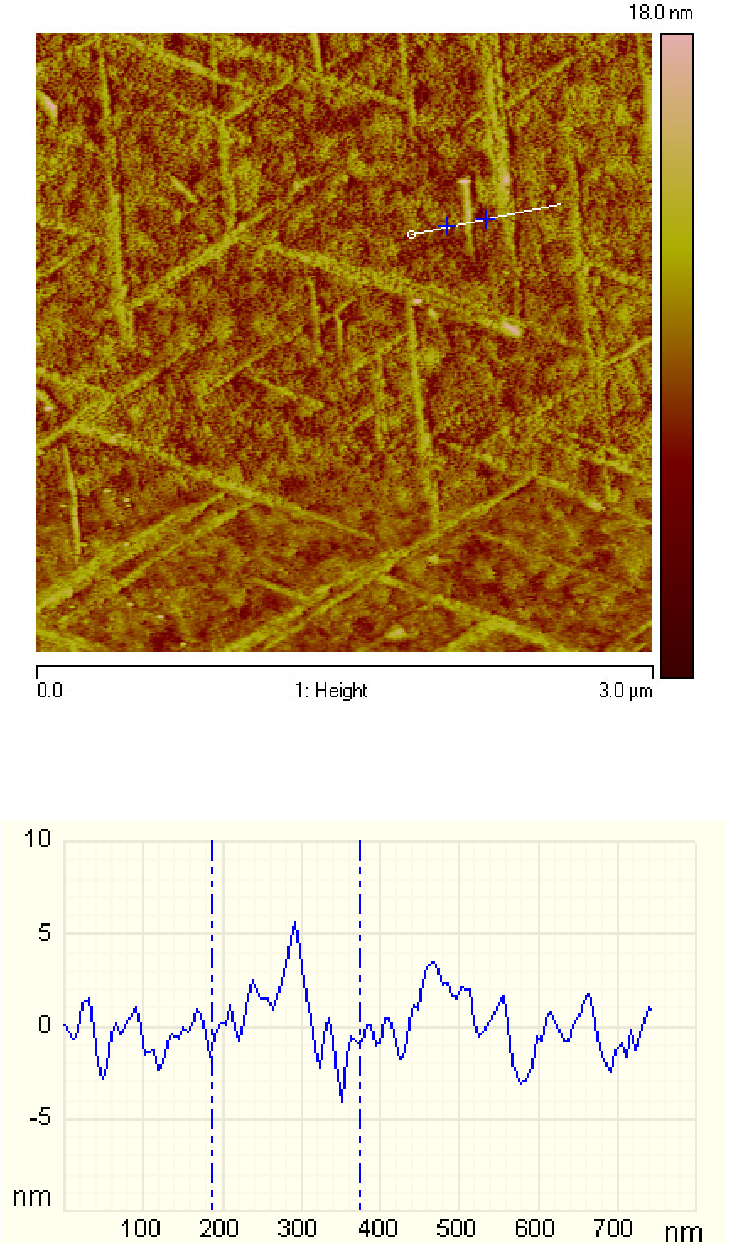

Figure 4.11 AFM micrograph (left) and topographical profile (right) of 100nm thick Pd film after hydrogenation at 18 bar and 650K.

The height difference between the nanostructures and Pd matrix in Figure 4.11 is indicative of coherency strain due to elastic incompatibility between the structures. The calculated incompatibility strain between Pd and β phase hydride is ~3.5%. In the case of a 100 nm thick film, the height of the plate nanostructures corresponds to 2-5% strain, assuming the interface is coherent.

The size and distribution of the ordered surface plates (shown in Figure 4.9) was not uniform over the entire surface of the film. In multiple specimens processed with the high temperature and pressure method mentioned in this chapter, a very dense arrangement of ordered surface plates are found near the edge of the film specimen. This density decreases going away from the edge, with plate density becoming very sparse up to 60-80 microns from the edge (Figure 4.12).

The edge gradient effect may be indicative of a stress-related formation mechanism of the nanoscale ordered plates. Due to differences in coefficients of thermal expansion, it is possible that the film relaxes around the edges in some specimens during heating and expansion and formation of β phase hydride can form more readily.

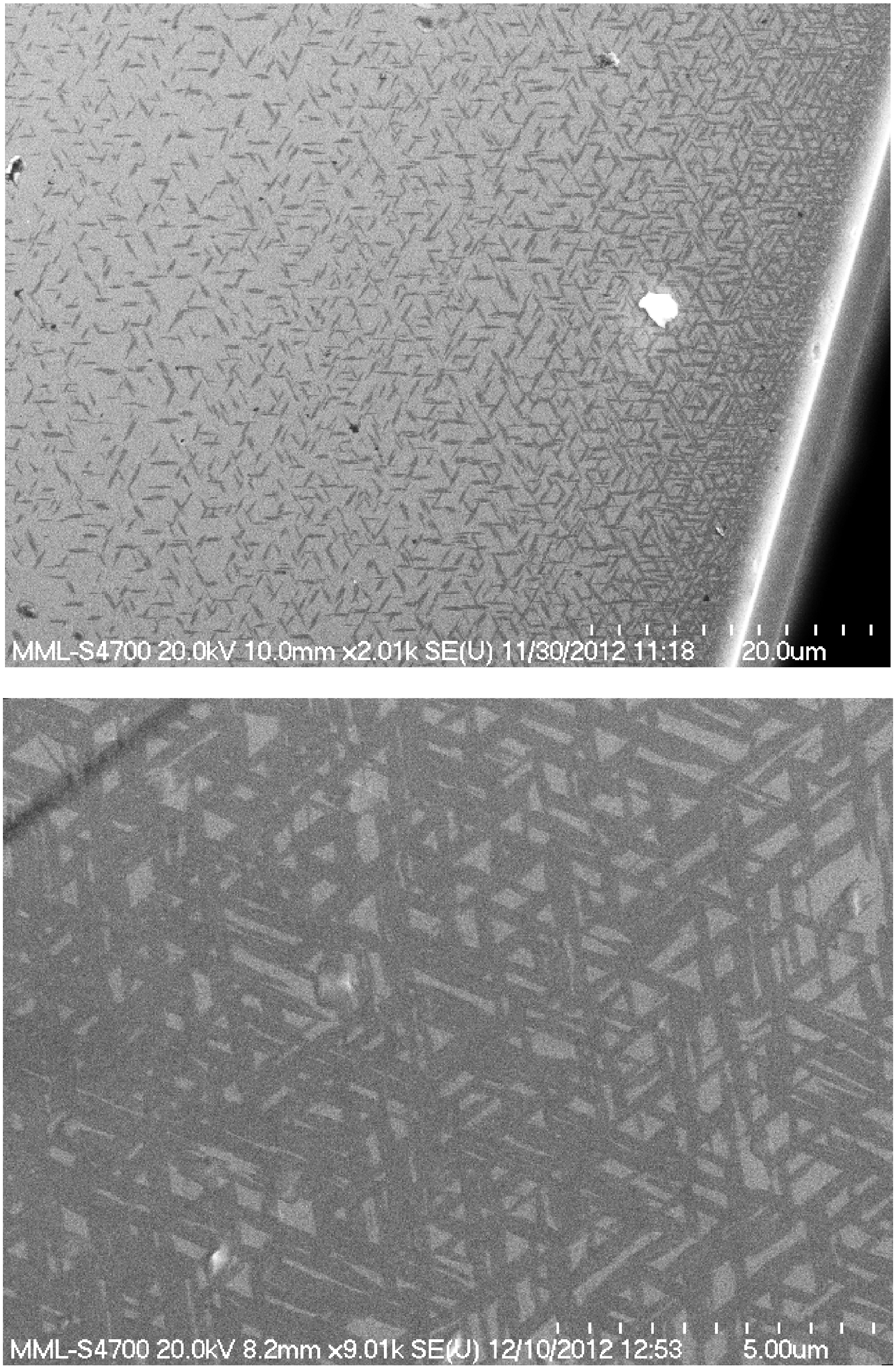

Figure 4.12 Gradient of ordered plates away from hydrogenated Pd specimen edge after hydrogenation (top) and magnified view of high concentration plate region (bottom).

A 100nm specimen was processed under the same conditions as the one with ordered structures (Figure 4.9) except Ar gas was loaded instead of hydrogen. This done to determine if the structure formation was due to only high temperature and pressure or if hydrogen plays a definite active role. After this processing, the film roughened slightly, but remained largely similar to the initially deposited state, as shown in Figure 4.13. These results illustrate that the ordered nanostructure surface formations observed after high temperature and high pressure hydrogen are most likely due to the presence of coherent β phase hydride precipitates or are remnants of these phases caused by twinning or partial coherency.

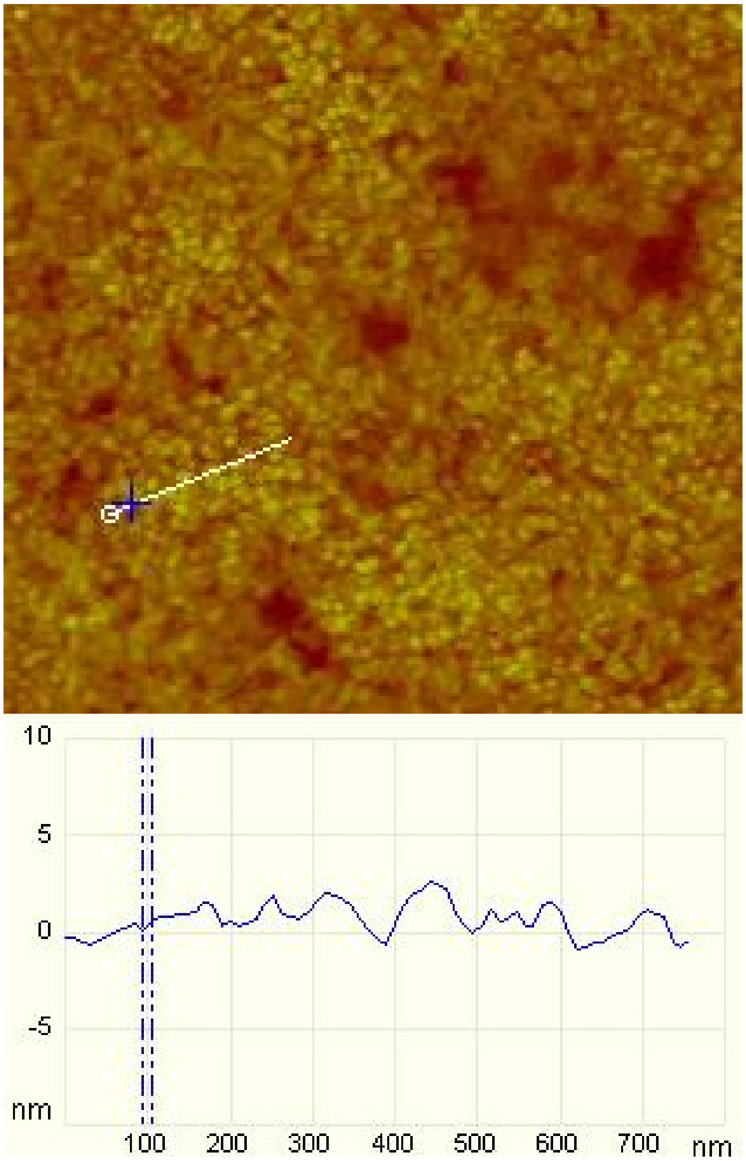

Figure 4.13 AFM micrograph of Pd film surface after annealing at 650K under 18 bar Ar pressure (2.5μ scan window) (top) and height profile (bottom).

4.4 Measuring Hysteresis with Sieverts Apparatus

In an attempt to capture isothermal hydrogen loading and unloading behavior of the epitaxial Pd films, the Sieverts apparatus was utilized to measure the volume of hydrogen gas absorbed via changes in gas pressure. Pressure was increased in incremental steps and measured after allowing the absorption to equilibrate. From this change in pressure, the volume of gas absorbed can be assimilated and the overall hydrogen concentration in the film can be calculated based on the overall volume of the Pd film.

This procedure was proven capable of measuring hydrogen absorption isotherms, as shown in [61], for particulate Mg. Similar experiments were attempted at room temperature and high pressure in 100nm epitaxial Pd film (to ensure full hydrogenation of the film). However, due to the small Pd volume in the film, as well as the limiting capacity of H atoms within the Pd lattice, insufficient changes in pressure occurred during stepwise pressure hydrogen loading. Due to this, the Sieverts apparatus was unable to capture suitable data for isothermal analysis of hydrogenation of 100nm Pd films. This behavior was verified by running the same isothermal analysis with Ar instead of H and capturing the same data (Figure 4.14). The y-axes of the plots should be considered arbitrary, as it is known that no gas was absorbed in the Ar test and the active volume can be adjusted in the hydrogen test to match the absorbed mass of the Ar test. In other words, the effect observed in both Ar and H tests are artifacts and do not correspond to true absorption data. The observation of negative absorbed mass in the case of H absorption further proves that the data is not representative of any real phenomenon, as pressure cannot increase in the chamber if gas is being absorbed into the solid state. The effect of negative absorption can be assumed to be due to ambient temperature fluctuations during the test.

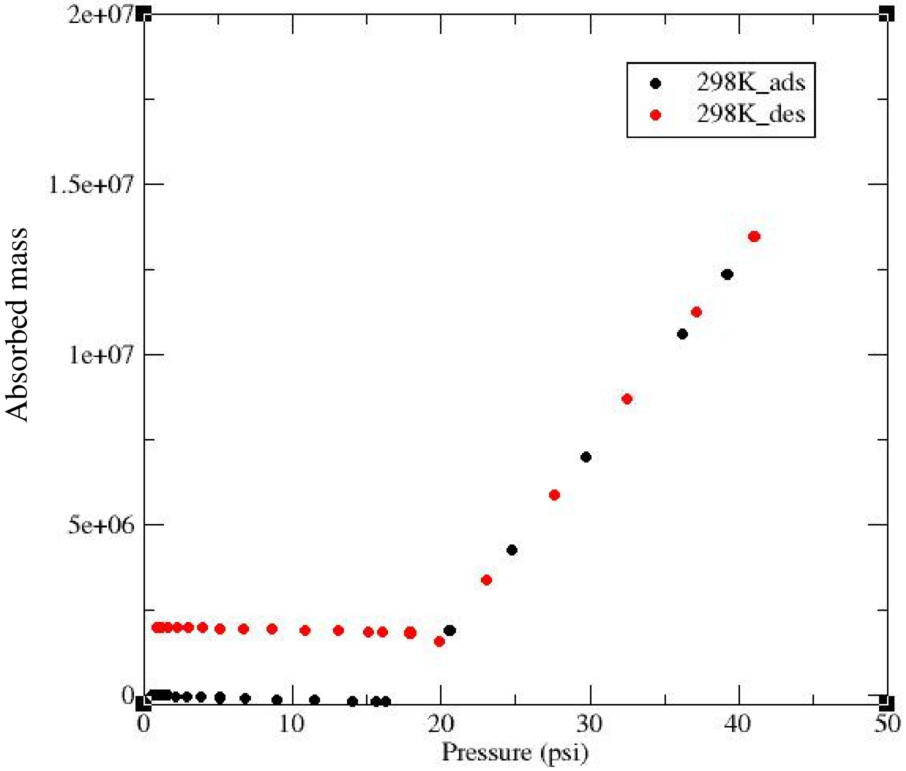

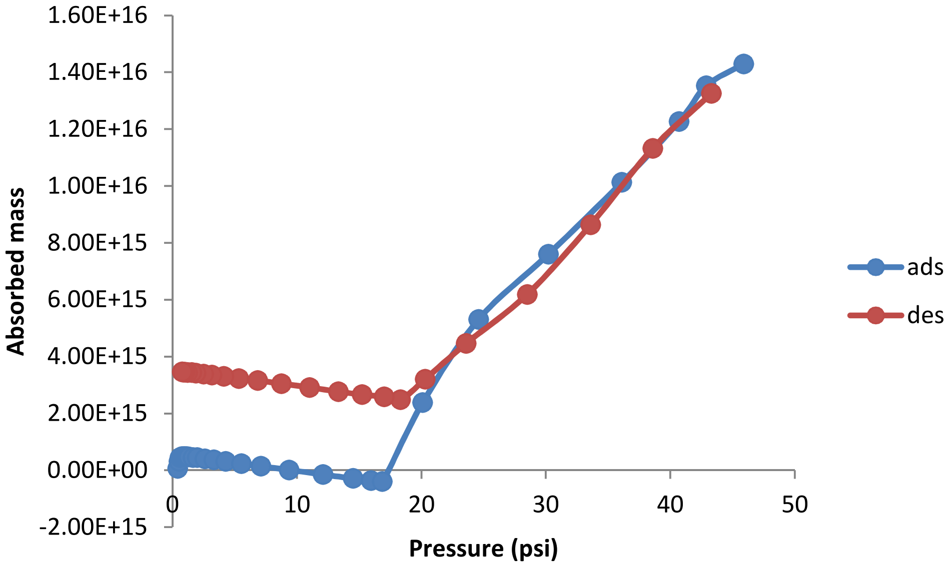

Figure 4.14 Isothermal response of Ar gas absorption at room temperature (top) and isothermal response of H absorption at room temperature (bottom) of 100nm Pd film.

4.5 Conclusions

The study presented in this chapter produced several conclusions regarding hydrogenation of epitaxial Pd thin films:

1. Room temperature hydrogenation produces films with roughened surfaces and measureable hydride content via XRD
2. High temperature and high pressure hydrogenation produces nanoscale ordered structures corresponding to coherent hydride phase formation in [50]
3. The size and density of ordered plates appears to be film thickness related; 100nm films produced ordered surface structures many times larger than those formed on 50nm film surface under similar processing conditions
4. In several specimens, a gradient of size and density of ordered plates is realized from the edge of the film specimen; the plates were very dense on the edge making up almost total concentration and proceeded to decrease in density up to 80 microns from the edge
5. The height profile difference between plates and Pd matrix, between 2-5nm in the 100nm film, correlates to the predicted strain incompatibility due to misfit strain between between Pd and β phase hydride (3.5%)

5 Controlling Hysteresis of Metal-hydride Transformations in Epitaxial Thin Films

The role of structure and phase transformation in reversible phase transformation in the Pd-PdH system has been the subject of study for several decades [26]. More recently, a thermodynamic model has been developed that accounts for intrinsic hysteresis due to coherency strain manifest by lattice misfit between α and β PdH phases [53]. This section presents a theory that extends this concept by adding a direct elastic interaction term (between film and substrate) to the Gibbs free energy, making the two-phase state a non-convex function with decreasing chemical potential, effectively eliminating intrinsic hysteresis.

This theoretical framework assumes two-phase decomposition in epitaxial film with perfect coherency between the phases as well as the film-substrate interface. In other words, this theoretical model does not predict the existence of two-phase state, but rather describes the evolution of free energy in the two-phase regime when concentrations, volume fractions, and strain of each phase are known. The relative concentration of interstitial atoms (in this case, hydrogen atoms) controls epitaxial strain of the phases. Isomorphic phase transformation is considered (to accurately model the Pd-PdH system), and Vegard's law is used to assume linear concentration dependence on epitaxial strain.

5.1.1 Elimination of Hysteresis in Epitaxially Constrained PdH Film during Hydrogen Loading

The thermodynamics of formation and evolution of coherent metal-hydride mixture is considered and applied more specifically to the Pd-PdH system [91], [92]. The trend to minimize elastic energy of internal stresses results in an equilibrium micro and nanostructure of the two-phase mixture a shown in Figure 4.8. Typical equilibrium two-phase configuration is an alternation of plane-parallel plates separated by an interface along the best fitting crystallographic plane of the phases.

It is possible to generalize the condition of phase transformation in an epitaxial film as a uniaxially constrained member, as shown in Figure 5.1. Self-strain between the phases (ε_0) as well as axial misfit of the initial phase (ε_M) contribute an elastic strain energy term to the overall free energy of the system.

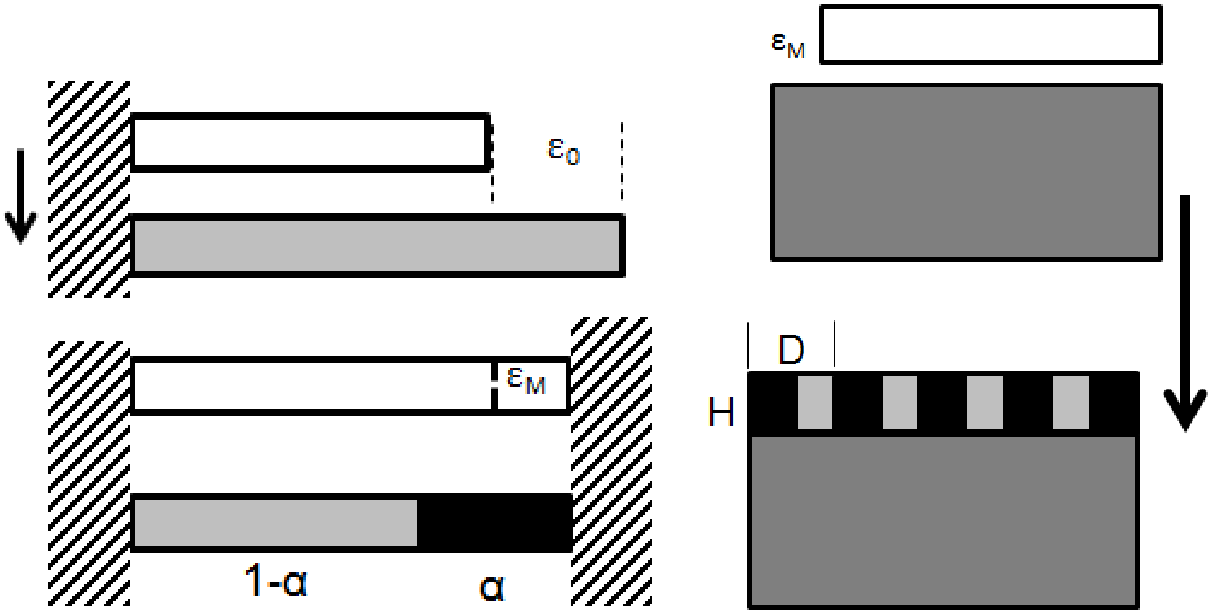

Figure 5.1 Schematic of unconstrained film that undergoes phase transformation with self-strain ε_0 (top-left) and under uniaxial constraint with initial misfit strain ε_M (bottom left) and epitaxial film with initial substrate misfit ε_M (top right) under phase decomposition with phase fractions α and 1-α (bottom right).

The free energy of an equilibrium two-phase metal-hydride system with coherent phases and no external constraint is defined as:

$$F = (1-\alpha) f_1(c_1) + \alpha f_2(c_2) + \alpha(1-\alpha)\frac{1}{2}\hat{G}_m\big(\hat{\varepsilon}_1(c) - \hat{\varepsilon}_2(c)\big)^2 \qquad (5.1)$$

where $f_1(c_1)$ and $f_2(c_2)$ are the free energy densities of undistorted phases (1-metal, 2-hydride) with concentration of hydrogen $c_1$and c_2, respectively. $\varepsilon_1(c)$ and $\varepsilon_2(c)$ are the self-strain of Phase 1 with concentration c_1 and Phase 2 with concentration c_2 which characterize the change in lattice parameters with Phase 1 at c=0 as a reference state [93].

$e_m(c_1, c_2) = \frac{1}{2}\hat{G}(\vec{m})\Delta\hat{\varepsilon}(c_1, c_2)$ is the energy of elastic interaction between the phases due to their strain incompatibility $\Delta\hat{\varepsilon}(c_1, c_2)$ along the plane interface with normal $\vec{m}$. $\hat{G}(\vec{m})$ is the plane modulus for $\vec{m}$. $\hat{G}(\vec{m}) = C - m\left(\vec{m}\hat{C}\vec{m}\right)^{-1}m$ [94]. C is the elastic modulus of the phases (assumed to be the same). Strain incompatibility $\Delta\hat{\varepsilon}$ for structural transformation with changing concentration of component can be presented as a sum of two parts: $\Delta\hat{\varepsilon} = \hat{\varepsilon}_0 + \hat{\varepsilon}(c_1, c_2)$, where ε_0 is self strain due to change of lattice structure (polymorphic transformation) without change of concentration which is taken into account by the second term.

First, consider isomorphic transformations, which have equilibrium two-phase state in a miscibility gap with a critical point. For isomorphic transformation, $\varepsilon_0 = 0$ and $\Delta\hat{\varepsilon} = \hat{\varepsilon}(c_1, c_2)$. Assume that linear dependence of lattice parameter of both phases on concentration (Vegard's law, ie. $\hat{\varepsilon}_2(c_2) - \hat{\varepsilon}_1(c_1) = \hat{\varepsilon}(c_2 - c_1)$). Free energy of two phases together with condition of conservation of average concentration is

$$\phi(c_1, c_2, \alpha; \mu, \bar{c}, \vec{m}) = (1-\alpha)f_1(c_1) + (\alpha)f_2(c_2) + \alpha(1-\alpha)e_m(c_2 - c_1)^2 + \mu[\bar{c} - \{(1-\alpha)c_1 + \alpha c_2\}] \tag{5.2}$$

Solving equations $\frac{\partial\phi}{\partial c_1}=\frac{\partial\phi}{\partial c_2}=\frac{\partial\phi}{\partial\alpha}=\frac{\partial\phi}{\partial\vec{m}}=0$ leads to an equilibrium orientation $\vec{m}$ of the interface between the phases and the two equations

$$\frac{\tilde{f}_2(c_2)-\tilde{f}_1(c_1)}{c_2-c_1}=\frac{\partial\tilde{f}_2}{\partial c_2}=\frac{\partial\tilde{f}_1}{\partial c_1}, \quad \tilde{f}_{1,2}=f_{1,2}(c)+e_m {c_{1,2}}^2 \tag{5.3}$$

for equilibrium concentrations c_1^* and c_2^*. This concentration does not depend on α. Then, the free energy of equilibrium two-phase mixture

$$f_{mix}(\bar{c})=\big(1-\alpha(\bar{c})\big)\tilde{f}_1(c_1^*)+\alpha(\bar{c})\tilde{f}_2(c_2^*)-e_m\bar{c}^2 \quad \text{with} \quad \alpha(\bar{c})=\frac{\bar{c}-c_1^*}{c_2^*-\bar{c}} \tag{5.4}$$

corresponding to the lever rule. The free energy is a nonconvex quadratic function of $\bar{c}$ (Fig. 1). Two-phase equilibrium is stable if $\bar{c}$ is fixed [93], [95]. However, it becomes unstable in open systems if chemical potentials are control parameters [52], [53].

The relations above are valid for any binary solution, substitutional or interstitial if Vegard's law is valid. For interstitial solutions with interstitial atoms with much larger diffusional mobility than the matrix, it is possible to consider stability at constant number of metal atoms (i.e. $\mu_1 \to 0$) . Then, the equilibrium is determined by chemical potential of interstitial atoms only which is a function of $\bar{c}$,

$$\mu(\bar{c})=\frac{df_{mix}}{d\bar{c}}=\frac{\hat{f}_2(c_2^*)-\hat{f}_1(c_1^*)}{c_2^*-c_1^*}-2e_m\bar{c} \quad \text{where} \quad c_1^*<\bar{c}<c_2^* \tag{5.5}$$

Thus, the chemical potential in closed systems measured for increasing fraction of hydride phase has negative slope. For an open system where equilibrium is determined by minimizing Gibbs free energy at given external chemical potential μ_H, $g=f_{mix}(\bar{c})-\mu_H\bar{c}$, $\mu(\bar{c})=\mu_H$, the two-phase state is unstable.

Transformation proceeds at $\mu^+(\bar{c}=c_1^*)$ and finishes at $\mu(c_1^*)=\mu\big(c_1^f\big)$. Reverse transformation proceeds at $\mu^-=\mu(c_2^*)$ starting at c_2^* and completed in single phase state at c_2^f. Then, thermodynamical hysteresis is

$$\Delta\mu = \mu^{+} - \mu^{-} = 2e_m(c_2^* - c_1^*) \quad (5.6)$$

This result is identical to the one obtained in [53], where the model of an elastically isotropic solution with non-interacting H atoms was used. Considering the problem in the frame of macroscopical thermodynamics in the present analysis allows us to show how hysteresis can be eliminated in a straightforward manner.

Eq. (3) describes the boundary of the two-phase area and at the same time also describes phase equilibrium in the film clamped by a rigid substrate. If the clamped film with normal $\vec{m}$ has no misfit with a substrate in the pure metallic state, its free energy as a function of concentration c is $f(c) + e_m c^2$, i.e. equal to $\hat{f}$. Clamping by the substrate decouples the layers with different compositions c_1^* and c_2^* after decomposition of the film. The equilibrium two-phase state is formed by elastic non-interacting phases and $f_{mix} = (1-\alpha)\hat{f}_1(c_1^*) + \alpha\hat{f}_2(c_2^*)$. Then, chemical potential

$$\mu(\bar{c}) = \frac{df_{mix}}{d\alpha}\frac{d\alpha}{d\bar{c}} = \frac{\hat{f}_2(c_2^*) - \hat{f}_1(c_1^*)}{c_2^* - c_1^*} = \frac{\partial \hat{f}}{\partial c_2} = \frac{\partial \hat{f}}{\partial c_1} \quad (5.7)$$

is constant and characterizes a stable two-phase equilibrium of elastically non-interacting phases. Correspondingly, there is no thermodynamic hysteresis at the transformation of such a clamped film. This is true for any initial misfit of a single phase film.

More generally, the coherent two-phase state can be stabilized with an arbitrarily oriented film-substrate interface that does not coincide with the orientation of phase interface, $\vec{m}$. In this case, an equilibrium structure of two-phase film is a heterophase polydomain: a periodic array of plane parallel domains of metal and hydride phases (elastic domains) [6]. Since average lattice parameter of heterophase epitaxial film should be equal to the parameter of substrate, the elastic energy of film-substrate interaction is determined by their average misfits:

$e_n = \frac{1}{2}\hat{G}(\vec{n})(\hat{\varepsilon}_M - [(1-\alpha)\hat{\varepsilon}_1 + \alpha\hat{\varepsilon}_2])^2 = (1-\alpha)\frac{1}{2}\hat{G}(\vec{n})(\hat{\varepsilon}_M - \hat{\varepsilon}_1)^2 + \alpha\frac{1}{2}\hat{G}(\vec{n})(\hat{\varepsilon}_M - \hat{\varepsilon}_2)^2 -$

$\alpha(1-\alpha)\frac{1}{2}\hat{G}(\vec{n})(\hat{\varepsilon}_2 - \hat{\varepsilon}_1)^2$ (5.8)

where $\hat{G}(\vec{n})$ is plane modulus for orientation $\vec{n}$, $\hat{\varepsilon}_M$ is a reference misfit determined by difference of lattices of Phase 1 (Figure 5.1) at $c_1 = 0$ and a substrate. The first two terms in Eq. (8) are the epitaxial energies of the phases and the last term is the energy of indirect interaction between the phases through the substrate. Including this energy in the free energy of constrained film leads to transformation of nonconvex function $f(\alpha)$ to convex and consequently to stabilization of the two-phase state. Since the orientation of $\vec{m}$ corresponds to minimum of the film energy, the last term in Eq. (8) $\hat{G}(\vec{n})(\hat{\varepsilon}_2 - \hat{\varepsilon}_1)^2$ is larger than $\hat{G}(\vec{m})(\hat{\varepsilon}_2 - \hat{\varepsilon}_1)^2$ in Eq. (1). For isomorphous solutions obeying Vegard's law, the free energy of constrained film is

$f(c_1, c_2, m; n) = (1-\alpha)f_1(c_1) + \alpha f_2(c_2) + \alpha(1-\alpha)(c_2 - c_1)^2 e_m + e_n(\delta - \bar{c})^2$ (5.9)

where $e_n = \hat{G}(\vec{n})\varepsilon^2$ and $\delta = \varepsilon_M/\varepsilon$. The minimization of the energy (Eq. (9)) at constant $\bar{c}$ leads to the following free energy of equilibrium two-phase mixture:

$f_{mix} = (1-\alpha)\hat{f}_1(c_1^*) + \alpha\hat{f}_2(c_2^*) - e_m\bar{c}^2 + e_n(\delta - \bar{c})^2$ (5.10)

with $0 < \alpha = \frac{\bar{c} - c_1^*}{c_2^* - \bar{c}} < 1$ at $c_1^* < \bar{c} < c_2^*$ and the equilibrium chemical potential

$\mu = \frac{\hat{f}_2(c_2^*) - \hat{f}_1(c_1^*)}{c_2^* - c_1^*} + 2e_n\delta + 2(e_n - e_m)\bar{c}$ (5.11)

Figure 5.2 displays the free energy and chemical potential vs. concentration plots (Eqs. 5.10 and 5.11).

Thus, for $e_n > e_m$, the film-substrate interaction, which does not affect equilibrium concentrations in the phases, transforms a nonconvex free energy of coherent phase mixture (Eq. (4)) to a convex function of an average concentration $\bar{c}$. It results in increasing chemical potential with $\bar{c}$. For thin films on a relatively thick substrate, $e_n > e_m$. However, the energy e_n

can be decreased if the thickness of the substrate decreases to relatively the same thickness of the film. Particularly in layered composites, it is possible to control the value of hysteresis and to decouple the phase interaction, making $e_n = e_m$.

To illustrate the relation between e_n and e_m, we estimate these values for epitaxial thin film Pd-H on c-plane sapphire substrate. For isomorphic Pd-PdH$_x$ transformation, both phases have FCC structure and the self-stress is pure dilatation. Therefore, the orientation of phase interface corresponding to minimal elastic energy e_m is determined by elastic anisotropy only. Since for both phases the coefficient of elastic anisotropy is positive (2C$_{44}$/(C$_{11}$-C$_{12}$)>0, $m_0 \parallel < 100 >$ [95], [96] and $G_m = \frac{(C_{11}+2C_{12})(C_{11}-C_{12})}{C_{11}} = 1.29*10^{11}\ J/m^3$. For $n \parallel < 111 >$ [95], [96] $G_n = \frac{6(C_{11}+2C_{12})C_{44}}{4C_{44}+C_{11}+2C_{12}} = 2.85*10^{11}\ J/m^3$. Taking into account that $\varepsilon_0 = \varepsilon c$, $e_m = 6.82*10^{-21}\ J/atom$ and $e_n = 15.10*10^{-21}\ J/atom$.

The analysis above can be generalized to include polymorphic transformations. The presence of the structural part $\hat{\varepsilon}_0$ in the self-strain at polymorphic transformation makes the equilibrium concentrations in the phases depend on the phase fraction α, thus rendering the lever rule invalid. This complication prevents investigation of elastic interaction between coherent phases without knowledge of concentration dependence of the free energies of undistorted phases $f_1(c)$ and $f_2(c)$. Different effective approximations have been used for calculating phase equilibria [97], [98].

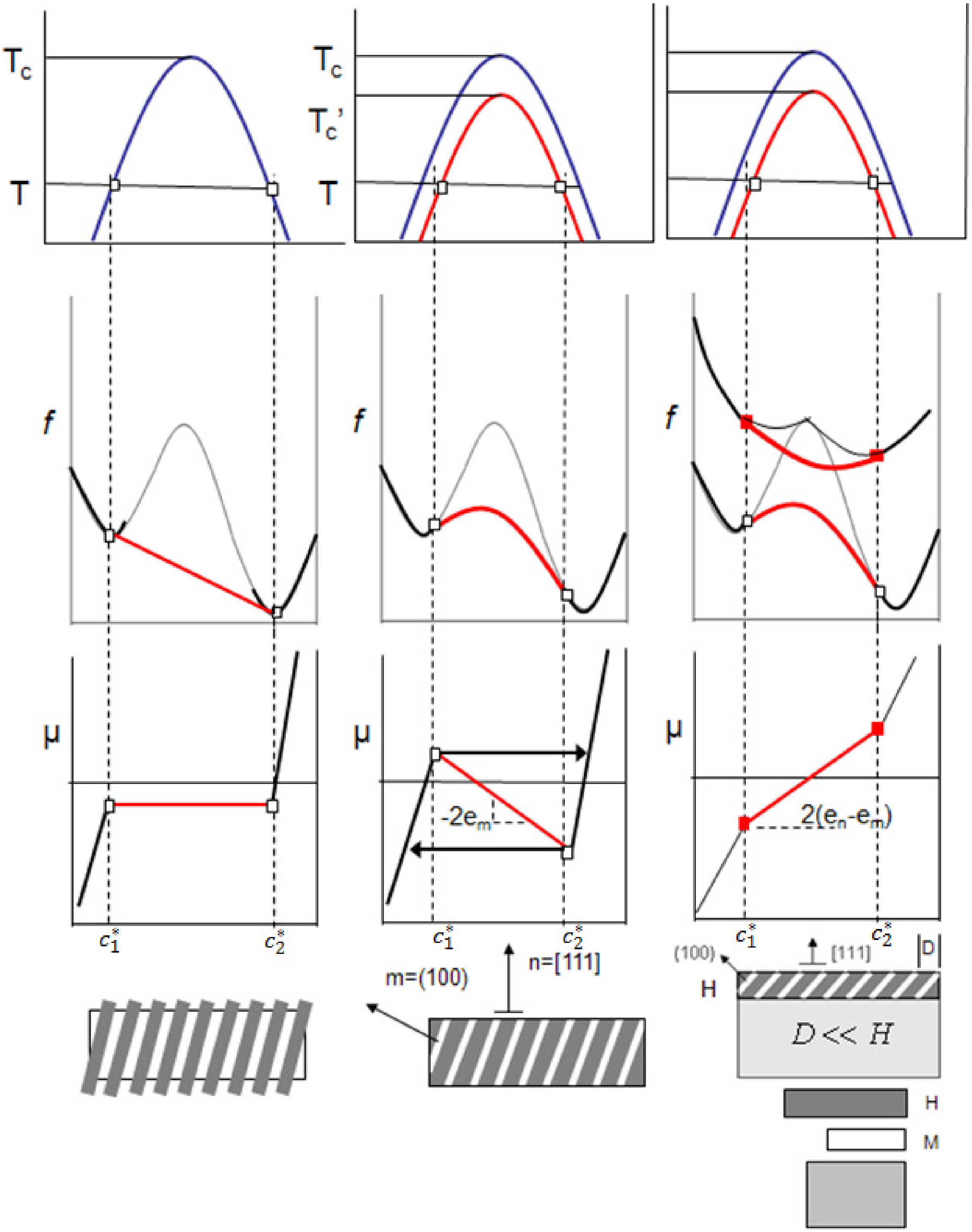

Figure 5.2 T-c phase digram, f-c free energy, and chemical potential μ-c for (left) freestanding incoherent and (middle) coherent metal-hydride structure, and (right) coherent clamped by substrate.

The model proposed in this chapter considers simple cases which can be considered analytically without an exact expression for bulk free energies of the phases. Using computational methods, including first principle calculations, it will be possible to obtain a quantitative description of phase transformation in epitaxial film of various metal-hydride transformations.

Comparing the presented theoretical model with experimental observation of metal-hydride transformation, it is necessary to clarify assumptions and approximation used in the theoretical analysis. The presented estimates neglect the difference of elastic properties between phases and their concentration dependence. However, initial stages of transformation ($\alpha \approx 0$ and $\alpha \approx 1$) can be determined more accurately since they correspond to first formation of an equilibrium crystal of a new phase in the matrix of initial phase [99]. Typical equilibrium crystal has the shape of a thin plate with field stress confines inside the plate (the energy of stress in a matrix concentrated near the plate edge is negligible as well as the surface energy of the plate in comparison with bulk elastic stress). Then, e_m is the energy of the plate crystal characterized by elastic modulus G_m of a new phase, while e_n is determined by G_n of a matrix phase since its fraction in a film is close to 1. For the Pd-PdH system, concentration dependence of moduli is not essential and can be neglected, but it is possible that difference $e_m - e_n$ changes its sign especially if film and substrate have comparable thickness.

Considering thermodynamics of heterophase polydomain film constrained by a substrate, it is assumed that the domain period, $\mathfrak{D}$, is much less than the thickness of the film, H. Then, the elastic energy of film-substrate interaction is determined by average misfit with a substrate that is less than energy of elastic interaction of an epitaxial single phase film. Taking into account that equilibrium domain period $\simeq (lH)^{1/2}$ [36], where characteristic length $l \simeq \Gamma/e_n < 10\ nm$ where

Γ is energy of domain interface of domain interface, $\frac{\mathfrak{D}}{H} = \left(\frac{l}{H}\right)^{1/2} \ll 1$ if $H > 50 \sim 100\, nm$. So, increase of film thickness and, correspondingly, thickness of domains, makes possible the relaxation of internal stress through formation of interface dislocations. Transition from coherent to partially coherent two-phase structure cannot qualitatively change the pattern of transformation, but essentially changes its thermodynamical characteristics. The relaxation of film substrate interface may result in the appearance (or increase) of thermodynamic hysteresis, while relaxation of interphase interfaces leads to decreasing hysteresis. However, this relaxation increases extrinsic hysteresis due to energy dissipation of domain interface movement. Therefore, the coherent transformation should be expected in a relatively narrow interval of film thickness [62].

It should also be mentioned that critical temperature of the miscibility gap is considerably lower for coherent phase transformation than for incoherent transformation (for Pd-H, it should be ~300K [50]). Thus, most experimental work corresponds to incoherent or partially coherent transformation and therefore cannot be quantitatively compared with Eq. (6). However, there are several studies demonstrating plate-like microstructure of two-phase Pd-PdH transformation with observed coherency between the two phases ([50], [51]) that correspond to the theoretically predicted {100} plate orientation. As shown in the previous chapter, progress in epitaxial thin film fabrication will enable nanoscale coherent metal-hydride phase decomposition in thin films, thus making thermodynamically reversible metal-hydride transformation feasible from both a theoretical and experimental perspective.

6 Conclusions

6.1 *Scientific and Technical Contributions*

6.1.1 Determination of Processing Parameters for Epitaxial Control of TMNS at a Ag-Si Interface

This work established a processing technique to fabricate TMNS at the interface between Ag foil and Si wafer [5]. Crystal orientation of the Si was found to determine Ag nanostructure morphology while annealing duration determined structure size and periodicity. Annealing in an oxygen rich environment (air) was discovered to be a critical parameter to prevent bulk diffusion between the layers and enable modulated nanostructure growth. Annealing specimens in vacuum resulted in bulk diffusion and eutectic solidification, establishing the need for oxide layer growth to retard diffusion and enable structure growth. EBSD analysis revealed the epitaxial relation between the single crystal Ag nanostructures and the surrounding Si.

6.1.2 Formation of Transversely Modulated Nanostructures in Epitaxial Pd Thin Films via Hydrogenation

Transversely modulated nanoscale surface structures were fabricated in epitaxial Pd film via high temperature and high pressure gas phase hydrogenation. These structures are oriented similarly to coherent hydride formations seen in [50], suggesting their presence is due to coherent β phase hydride formation. A thickness effect was observed, where 50 nm films displayed ordered plates with a much smaller aspect ratio than those formed in a 100 nm film. An edge-gradient effect was observed in some specimens, suggesting that phase fraction of the ordered nanostructures may be dependent on internal stress of the film. In other words, the stress along the edges of the film may be relaxed during heating due to differences in thermal coefficients and interfacial defect formation, resulting in varying equilibrium nanostructure concentration.

6.1.3 Development of a Thermodynamic Model for Predicting the Control or Elimination of Hysteresis due to Metal-hydride Transformations in Epitaxial Thin Films

A thermodynamic approach has been formulated that predicts elimination of intrinsic hysteresis during isomorphic phase transformation in metal-hydride epitaxial thin films via substrate constraint [91], [92]. This is due to the addition of an elastic energy term in the total free energy which represents elastic interaction between the film and substrate due to film-substrate misfit and epitaxial misfit of the phases. This term makes the free energy of the two-phase state a nonconvex function, making the chemical potential an increasing linear function in this range.

6.2 Future Work

Upon consideration of the scientific developments made in this dissertation, several concepts can be proposed for further development.

6.2.1 Measure Electronic Properties of Ag-Si Heterostructure with Nanostructured Interface

The effect of Ag nanostructure morphology, size, and density on interfacial contact resistance can be determined via electrical measurements. Specimens created with various processing parameters can be tested and compared to Si wafers metallized with commercially available Ag paste to compare contact resistance.

6.2.2 Determine Effect of SiO_2 Thickness and Growth on Interfacial Ag Nanostructure Growth

Oxide layers of varying thickness can be grown on Si wafer via thermal annealing. Specimens can be constructed by sandwiching Ag foil with the annealed Si wafers and processed in vacuum. The necessary volume of oxide necessary to prevent bulk diffusion and enable nanostructure formation can be realized, which may yield insight into a more rigorous formation mechanism as oxide concentration along the interface can be known.

6.2.3 Structural Characterization of Transversely Modulated Nanostructures in Epitaxial Pd Film after Hydrogenation

Transmission electron microscopy (TEM) can be utilized to characterize the crystal structure and composition of the ordered nanostructures observed in the 100 nm Pd films. This will enable local characterization of each individual structure via electron diffraction. Furthermore, the orientation of the nanostructures through the thickness of the film can be determined by fabricating a cross sectional TEM specimen for imaging. If the phases completely disappear during imaging due to electron beam heating, the presence of hydrogen in the ordered structures can be indirectly confirmed.

6.2.4 Capture Hysteresis Behavior of Epitaxial Pd Thin Films during Hydrogenation via Gravimetric Analysis

Gravimetric analysis can be considered to characterize the hysteresis behavior of 100 nm epitaxial Pd thin films during gas phase hydrogenation. This technique is generally more sensitive than the Sieverts apparatus used in experiments described in this dissertation which has a pressure measurement sensitivity of 0.001 psi. A gravimetric test setup located at NIST is capable of high temperatures (500°C) and has sensitivity of fractions of a microgram.

References

[1]. A.L. Roytburd, *Physica Status Solidi A-Applied Research*, **37**, 1, 1976, 329-336

[2]. R. J. Zeches, M. D. Rossell, J. X. Zhang, A. J. Hatt, Q. He, C.-H. Yang, A. Kumar, C. H. Wang, A. Melville, C. Adamo, G. Sheng, Y.-H. Chu, J. F. Ihlefeld, R. Erni, C. Ederer, V. Gopalan, L. Q. Chen, D. G. Schlom, N. A. Spaldin, L. W. Martin, R. Ramesh, Science, 326, 977 (2009).

[3]. H. Brune, M. Giovannini, K. Bromann, K Kern, *Nature* **394**, 451-453.

[4]. Y. Le Bouara, A. Loiseaub, A.G. Khachaturyan, *Acta Materialia,* **46**, 8, 1998, 2777-2788

[5]. B.M. Boyerinas, J. Balsam, A.L. Roytburd, H.A. Bruck, *Journal of Applied Physics*, 2013, **113**, 18, 184302

[6]. A.L. Roytburd, *Journal of Applied Physics,* **83**, 1, 1998, 228-238

[7]. S. Kontermann, R. Preu, G. Willeke, *Applied Physics Letters*, **99**, 2011, 111905

[8]. H.H. Berger, *Journal of the Electrochemical Society*, **119**, 507, 1992

[9]. D.K. Schroder, D.L. Meier, *IEEE Transactions: Electron Devices,* **31**, 637, 1984

[10]. M. Hilali, M. Al-Jassim, B. To, H. Moutinho, A. Rohatgi, S. Asher, *Journal of the Electrochemical Society*, **152**, G742, 2005

[11]. X.Q. Zeng, Y. Wang, H. Deng, M.L. Latimer, Z. Xiao, J. Pearson, T. Xu, H. Wang, U. Welp, G.W. Crabtree, W. Kwok, *ACS Nano*, **5**, 9, 2011, 7443-7452

[12]. X.Q. Zeng. Y.L. Wang, Z.L. Xiao, M.L. Latimer, T. Xu, W.K. Kwok, *Journal of Materials Science*, **47**, 2012, 6647-6651

[13]. J. Carpena-Nunez, D. Yang, J. Kim, C. Park, L.F. Fonseca, *Nanotechnology*, **24**, 2013, 1-10

[14]. C.M. Chang, M.H. Hon, I.C. Leu, *ACS Applied Materials & Interfaces*, **5**, 2013, 135-143

[15]. X.Q. Zheng, Y.L. Wang, Z.L. Xiao, M.L. Latimer, T. Zu, W.K. Kwok, *Journal of Materials Science*, **47**, 18, 2012, 6647-6651

[16]. F. Greco, L. Ventrilli, P. Dario, B. Mazzolai, V. Mattoli, *International Journal of Hydrogen Energy*, **37**, 22, 2012, 17529-17539

[17]. L. K. Randeniya, P.J. Martin, A. Bendavid, *Carbon*, **50**, 5, 2012, 1786-1792

[18]. R.M. Penner, *MRS Bulletin*, **35**, 10, 2010, 771-777

[19]. F. Yang, S.C. Kung, M. Cheng, J.C. Hemminger, RM Penner, *ACS Nano*, **4**, 9, 2010, 5233-5244

[20]. C.W. Ong, Y.M. Tang, *Journal of Materials Research*, **24**, 6, 2009, 1919-1927

[21]. X.M.H. Huang, M. Manolidis, S.C. Jun, J. Hone, **86**, 14, 2005, 143104

[22]. M. Ramanathan, G. Skudlarek, H.H. Wang, S.B. Darling, *Nanotechnology*, **21**, 125501, 2010, 1-6

[23]. J.M. Wheeler, T.W. Clyne, *International Journal of Hydrogen Energy*, **37**, 2012, 14315-14322

[24]. I. Matsumoto, K. Sakaki, Y. Nakamura, E. Akiba, *Applied Surface Science*, **258**, 2011, 1456-1459

[25]. T.B. Flanagan, C.N. Park, D.H. Everett, *Journal of Chemical Education*, **64**, 11, 1987

[26]. M.V. Goltsova, *International Journal of Hydrogen Energy*, **31**, 2006, 223-229

[27]. T.B. Flanagan, J.D. Clewley, *Journal of the Less Common Metals,* **83**, 1982, 127-141

[28]. T.B. Flanagan, W.A. Oates, *Journal of the Less Common Metals*, **92**, 1983, 131-142

[29]. T.B. Flanagan, T. Kuji, *Journal of the Less Common Metals*, **152**, 1989, 2130226

[30]. D. Wang, T.B. Flanagan, T. Kuji, *Physical Chemistry Chemical Physics*, **4**, 2002, 4244-4254

[31]. R. Kelekar, H. Giffard, S.T. Kelly, B.M. Clemens, *Journal of Applied Physics*, **101**, 2007, 114311

[32]. J. X. Zhang, B. Xiang, Q. He, J. Seidel, R. J. Zeches, P. Yu, S. Y. Yang, C. H. Wang, Y-H. Chu, L. W. Martin, A. M. Minor, R. Ramesh, *Nature Nanotechnology*, **6**, 2011, 98-102

[33]. C. Ballif, D. M. Huljić, G. Willeke, A. Hessler-Wyser, *Applied Physics Letters*, **82**, 12, 2002, 1878-1880

[34]. A. L. Roytburd, T. S. Kim, Q. Su, J. Slutsker, M. Wuttig, *Acta. Mat.*, **46**, 14, 1998, 5095-5107

[35]. S.P Alpay, A.L. Roytburd, *Journal of Applied Physics,* **83**, 9, 1998, 4714-4726

[36]. A. L. Roytburd, *Journal of Applied Physics*, **83**, 1, 1998, 239-245

[37]. S.P. Alpay, A. L. Roytburd, *Journal of Applied Physics*, **83**, 9, 1998, 4714-4723

[38]. V. Nagarajan, I.G. Jenkins, S.P. Alpay, H. Li, S. Aggarwal, L. Salamanca-Riba, A.L. Roytburd, R. Ramesh, *Journal of Applied Physics*, **86**, 1, 1999, 595-602

[39]. A.L. Roytburd, J. Slutsker, *Journal of Mechanics and Physics of Solids*, **49**, 2001, 1795-1822

[40]. A.L. Roytburd, J. Ouyang, B.M. Boyerinas, H.A. Bruck, *Applied Physics Letters*, **99**, 172902, 2011

[41]. B. D. Adams, A. Chen, *Materials Today*, **14**, 6, 2011, 282-287

[42]. T. Skoskiewicz, *Physica Status Solidi A*, **11**, 2, 1972, K123

[43]. P. Tripodi, D. DiGioacchino, R. Borelli, J.D. Vinko, *Physica C*, **338**, 2003, 571-572

[44]. P. Tripodi, D. DiGioacchino, J.D. Vinko, *Physica C*, **408**, 2003, 350-352

[45]. P. Tripodi, D. DiGioacchino, J.D. Vinko, *International Journal of Modern Physics B*, **21**, 18, 2007

[46]. A. Pundt, R. Kirchheim, *Annual Review of Materials Research*, **36**, 1, 2006, 555-608

[47]. H. Idrissi, B. Wang, M. S. Colla, J. P, Raskin, D. Schryvers, T. Pardoen, *Advanced Materials*, **23**, 2011, 2119-2122

[48]. B. Amin-Ahmadi, H. Idrissi, R. Delmelle, T. Rardoen, J. Proost, D. Schryvers, *Applied Physics Letters*, **102**, 2013, 071911

[49]. F.D. Manchester, *Phase Diagrams of Binary Hydrogen Alloys,* ASM International, 2000, 158

[50]. E. Ho, H. A. Goldberg, G. C. Weatherly, F. D. Manchester, *Acta Metallurgica*, **27**, 1979, 841-853

[51]. H.C. Jamieson, G.C. Weatherly, F.D. Manchester, *Journal of Less Common Metals*, **50**, 85-102, 1976

[52]. R.B. Schwarz, A.G. Khachaturyan, *Physical Review Letters*, **74**, 13, 1995, 2523-2526

[53]. R.B. Schwarz' A.G. Khachaturyan, *Acta Materialia*, **54**, 2006, 313-323

[54]. C. Lexcellent, G. Gondor, *Intermetallics*, **15**, 2007, 934-944

[55]. R. Feenstra, G. J. de Bruin-Hordijk, H. L. M. Bakker, R. Griessen, D. G. de Groot, *Journal of Physics F: Metal Physics*, **13**, 1983, L31-L18

[56]. Y. Pivak, H. Schreuders, M. Slaman, R. Griessen, B. Dam, *International Journal of Hydrogen Energy*, **36**, 3, 2011, 4056-4067

[57]. S. Wagner, A. Pundt, *Acta Materialia*, **59**, 2011, 1862-1870

[58]. http://serc.carleton.edu/images/research_education/geochemsheets/techniques/IUCrimg69.v2.gif

[59]. http://www.nobelprize.org/educational/physics/microscopes/tem/images/tem1-1.jpg

[60]. http://artsci.ucla.edu/BlueMorph/research/AFM1.jpg

[61]. S. Zheng, K. Wang, V. Oleshko, L. Bendersky, *Journal of Physical Chemistry C,* **116**, 40, 2012, 21277–21284

[62]. S. Wagner, H. Uchida, V. Burlaka, M. Vlach, M. Vlcek, F. Lukac, J. Cizek, C. Baehtz, A. Bell, A. Pundt, *Scripta Materialia*, **64**, 10, 2011, 978-981

[63]. K. Northemann, A. Pundt, *Physical Review B*, **78**, 2008, 014105

[64]. E.J. Grier, O. Kolosov, A.K. Petford-Long, R.C.C. Ward, M.R. Wells, B. Hjorvarsson, *Journal of Physics D: Applied Physics*, **33**, 2000, 894-900

[65]. J.W.J. Kerssemakers, S.J. van der Molen, N.J. Koeman, R. Gunther, R. Griessen, *Nature*, **406,** 2000, 489-491

[66]. R. W. Olesinski, G. J. Abbaschian, *Binary Alloy Phase Diagrams*, II Ed., 1, 92 (1990)

[67]. J.J. Huiberts, R. Griessen, J.H.Rector, R.J. Wijngaarden, J.P. Dekker, D.G. de Groot, N.J. Koeman, *Nature*, **380**, 1996, 231-234

[68]. J.W.J. Kerssemakers, S.J. van der Molen, R. Gunther, B. Dam, R. Griessen, *Physical Review B*, **65**, 2002, 075417

[69]. B.J. Kooi, E. Zoestbergen, J.T.M. De Hosson, J.W.J. Kerssemakers, B. Dam, R.C.C. Ward, *Journal of Applied Physics*, **91**, 2002, 1901-1909

[70]. A. Remhof, J.W.J. Kerssemakers, S.J. van der Molen, R. Grissen, *Physical Review B*, **65**, 2002, 054110

[71]. J.D. McBrayer, R.M. Swanson, T.W. Sigmon, *Journal of the Electrochemical Society,* **133,** 6, 1986, 1242-1246

[72]. N. Sasaki, S. Watanabe, M. Tsukada, *Physical Review Letters*, **88**, 2002, 046106

[73]. Y.G. Ding, C.T. Chan, K.M. Ho, *Physical Review Letters*, **67**, 1991, 1454

[74]. H.M. Zhang, R.I.G. Uhrberg, *Physical Review B*, **74**, 2006, 195329

[75]. H. Hirayama, T. Komizo, T. Kawata, K. Takayanagi, *Physical Review B*, **63**, 2001, 155413

[76]. R.I.G. Uhrberg, H.M. Zhang, T. Balasubramanian, E. Landermark, H.W. Yeom, *Physical Review B*, **65**, 2002, 081305

[77]. H.M. Zhang, J.B. Gustafsson, L.S.O. Johansson, *Physical Review B*, **74**, 2006, 201304

[78]. S.J. Chey, L. Huang, J.H. Weaver, *Physical Review B*, **59**, 1999, 16033

[79]. H. Hong, R.D. Aburano, D.S. Lin, H. Chen, T.C.Chiang, P. Zschack, E.D. Specht, *Physical Review Letters*, **52**, 1995, 1839

[80]. R.D. Aburano, H. Hong, J.M. Roesler, K. Chung, D.S. Lin, P. Zschack, H. Chen, T.C. Chiang, *Physical Review B*, **52**, 1995, 1839

[81]. G. Schubert, F. Huster, P. Fath, *Solar Energy Materials & Solar Cells*, **90**, 2006, 3399-3406

[82]. C.H. Lin, S.P. Hsu, W.C. Hsu, *Silicon Solar Cells: Structural Properties of Ag-Contacts/Si-Substrate* (2011). In L.A. Kosyachenko, *Solar Cells – Silicon Wafer-Based Technologies*

[83]. C. Ballif, D.M. Huljic, A. Hessler-Wyser, G. Willeke, *Conference Record Of The Twenty-Ninth IEEE Photovoltaic Specialists Conference 2002*, 2002, 360-363

[84]. S. Kontermann, G. Willeke, J. Bauer, *Applied Physics Letters*, **97**, 191910, 2010

[85]. K. T. Butler, P. E. Vullum, A. M. Muggerud, E. Cabrera, J. H. Harding*, Physical Review B,* **83**, 2011, 235307-1

[86]. Hong KK, Cho SB, You JS, Jeong JW, Bea SM, Huh JY, *Solar Energy Materials & Solar Cells* 2009; 93: 898

[87]. Jeong MI, Park SE, Kim DH, Lee JS, Park YC, Ahn KS, Choi CJ, *Journal of the Electrochemical Society*. 2010; 157: H934

[88]. Sangwal, K, *Etching of Crystals*. Netherlands: North-Holland Physics Publishing, 1987. Print.

[89]. http://www.engr.uky.edu/~cense/images/ebeam2.gif

[90]. "Sieverts Apparatus User's Manual", National Institute of Standards and Technology, Nov. 2010

[91]. B.M. Boyerinas, H.A. Bruck, A.L. Roytburd (2013) *Proceedings of the 2013 Spring MRS Meeting*

[92]. B.M. Boyerinas, H.A. Bruck, A.L. Roytburd (2013), "Thermodynamically Reversible Metal-Hydride Transformation in Epitaxial Thin Films", submitted to *Physical Review Letters*

[93]. A.L. Roitburd, *Soviet Physics Solid State*, **26**, 1229, 1984, **27**, 298, 1985

[94]. S.S. Orlov, V.L. Indenbom, *Kristallografiya*, **14**, 780, 1969

[95]. J.W. Cahn, *Acta Metallurgica*, **10**, 1962

[96]. A.G. Khachaturyan, *The Theory of Structural Transformations in Solids*, (Wiley & Sons, New York, 1983)

[97]. J.W. Cahn, F. Larche, *Acta Materialia*, **32**, 1915, 1984

[98]. A.L. Roytburd, J. Slutsker, *Acta Materialia*, **50**, 1809, 2002

[99]. A.L. Roytburd, *Phys. Met. Metall*., **59**, 43, 1985